OPTIMIZATION OF FNIRS PROBE GEOMETRY TO ELIMINATE NON-BRAIN TISSUE CONTAMINATION

by

Ayşegül Tümer

BSc, Physics, Boğaziçi University, 2008

Submitted to the Institute of Biomedical Engineering
in partial fulfillment of the requirements
for the degree of
Master of Science
in
Biomedical Engineering

Boğaziçi University
2014

ACKNOWLEDGMENTS

I would like to thank Dr. Ata Akın for his constant enthusiasm, support, patience and open-mindedness during my master's studies. When I first walked through the wide open doors of NOILab, I was deprived of inspiration, hope and will to continue in academy then he took scattered pieces of me and meticulously shaped me into the scientista and a teacher I am today; a scientista I always dreamt of becoming. This work is his courage interpreted by me. I am forever in debt for everything you have thought me Sensei, and this thesis is merely a grain of sand from the shores of my gratitude for you. You are the milestone of my academic life, you are the game changer.

Dr. Mehmet Burçin Ünlü, my advisor in Physics master studies, has shared his knowledge on MCML and contributed with great ideas and tricks for this thesis benevolently. I would like to thank him for his time and kindness.

A great friend and a colleague whom I have been lucky to have worked with, I would like to show my gratitude to Agah Karakuzu for his time and contribution for the crown analysis of this thesis. You are a hardworking, intelligent and a perceptive scientist and I know fate will be kind enough to provide you with what you truly deserve.

I am grateful to Dr. Sinem Burcu Erdoğan for her contributions in my thesis for the translating fMRI to fNIRS analysis and being supportive throughout these two years.

For representing a great role model in my academic life, I am thankful to Dr. Yasemin Keskin Ergen, and I wish to become as graceful, hardworking, and knowledgeable scientista as she is if I ever can.

I also would like to thank Rüştü Umut Tok, a former graduate of Dr. Akın's, for introducing me to MCML and for his availability when I required help, and trust me, I needed a lot of help...

I would like to thank my NOILab friends, (no order is intended) Melih Can, Yunus Engin Gökdağ, Ufuk Dalmış, Fırat Şansal, Deniz Nevşehirli, Seda Dumlu, Duygu Şahin for their friendship and support.

My great friends, my sisters at heart; Öznur Demir and Bengü Aktaş. You are both gifts of this life, my chosen family.

Selin Akıncı, thank you for turning those hard times into fun times. You have magic in you.

Annem, hayata karşı dilediğim kadar cesur ve güçlü olabilmem için her türlü imkanı sağladığın, bana inandığın, adadığın hayatın için teşekkür ederim. Bu hayat da senindir, çünkü biz biriz.

Babam, senin gibi bir insanın kızı olmak sahip olunabilecek en büyük gurur, öğrettiğin tüm değerler için minnettarım.

Abilerim, kim olduğumu bulmamın ve bugünüme gelmemin yapıtaşları. Sizin için daima en iyisini ümit ediyorum. Bulunduğunuz yerlere gelmek için gösterdiğiniz çabaya şahit olmam, istediklerime kolay ulaşamadığım zamanlarda, vazgeçmeyi bir seçenek olarak kabul etmemeyi öğretti.

And finally, I would like to thank myself for GOING THE DISTANCE. Girl, you're one stubborn son of a gun.

This work was sponsored in part by Boğaziçi University Research Fund Project No's: 11DX4 and 13XM1 and in part by TUBITAK Projects No's: 112E034 and 113E003.

ABSTRACT

OPTIMIZATION OF FNIRS PROBE GEOMETRY TO ELIMINATE NON-BRAIN TISSUE CONTAMINATION

Functional near infrared spectroscopy (fNIRS) is a developing non-invasive technique used for measurement of oxygenation in the adult and newborn human brain during cognitive tasks. The oxygenation in the brain is expressed as the change in the concentrations of the major absorbers such as oxy- and deoxy-haemoglobin in blood as a response to the brain activation during light-tissue interactions. The absorption of these absorbers at different wavelengths are calculated by using a Modified Beer-Lambert Law (MBLL). Depending on the aim of the fNIRS measurement, at least two different wavelengths are selected from the optical window (600-900 nm) for the detection of the concentration changes of these absorbers in order to minimise the undesired effect of "crass-talk". The probe of fNRIS containing a combination of various light sources (LD, LED, etc.) and detectors aims to pinpoint the activated regions of the brain relying on the theory of light path distribution known as "banana-shape" in literature. As a well proven technique, Monte Carlo Simulations which describes the photon migration multi layer media is used for modelling of head and fNIRS probe for investigation of the system. The most important disadvantage of the technique is the contamination of the brain signal with the signals received from the superficial layers of the head, namely; scalp and skull layers. For the decoupling of these signals, various signal regression and filtering techniques are used. In this thesis as a signal regression technique is presented, where a real fMRI data is used in Monte Carlo Simulations for assigning a near-far detector position which respectively contains the signal from the superficial layers only and the signals obtain from both the superficial layers and brain matter. The positions of these detectors were found to be around 17, 18 and 19 mm from the source for the head model with an average human skull thickness of 7 mm.

Keywords: MCML, fNIRS, Photon Migration in Biological Tissues.

ÖZET

Yakın kızılaltı spektroskopisi (YKAS: fNIRS) bilişsel görevler sırasındaki yetişkin ve yeni doğmuş insan beynindeki oksijenlenmenin ölçümünün gerçekleştirebilmesi için geliştirilmekte olan invazif olmayan bir görüntüleme tekniğidir. YKAS'de beyindeki oksijenlenme, ışık-doku etkileşimi sırasında beyin aktivasyonunun bir cevabı olan kan içerisindeki temel soğurucu moleküllerden oksi-hemoglobin ve deoksi-hemoglobin konsantrasyonunun değişimi olarak ifade edilmektedir. Farklı dalga boylarındaki ışığın bu moleküller tarafından soğurulması uyarlanmış Beer-Lambert Yasası (MBLL) kullanılarak hesaplanmaktadır. YKAS ölçümünde amacına göre soğurucu molekül konsantrasyonlarının değişimini ölçmek üzere istenmeyen "cross-talk" etkisinini en aza indirgemek için optik pencere olarak adlandırılan 600-900 nm aralığından seçilmiş iki ya da daha fazla dalgaboyu kullanılmaktadır. Çeşitli ışık kaynakları (LD, LED, vs.) ve algılayıcı kombinasyonundan oluşturulan YKAS probu, kaynaktan çıkıp istenilen algılayıcıya ulaşan fotonlarının dağılımının, literatürde "banana-shape" olarak tanımlanan, ışığın muz şeklindeki bir yol dağılımı takip ettiği teorisini temel alarak, beynin aktive olan bölgelerini belirlemeyi amaçlamaktadır. Başarısı kanıtlanmış bir metod olan, çoklu biyolojik katmanda foton göçünün tasvir edildiği Monte Carlo benzetimleri, kafa ve YKAS probunu istenilen ölçüme göre modelleyip, sistemi anlamaya olanak sağlamaktadır. YKAS'nin en önemli zayıf noktası beyni çevreleyen deri ve kafatası katmanlarından gelen sinyalin, gri maddede oluşan sinyal ile birleşerek, aktivasyonun ölçümü sırasında bozucu bir etki yaratmasıdır. Bu iki sinyalin ayrıştırılması için çeşitli yöntemler geliştirilmektedir. Bu tezde sinyal ayrıştırma tekniği olarak, YKAS prob tasarımında yakın ve uzak olarak adlandırılan, sırasıyla beyin dışı biyolojik katmanlardaki sinyali algılayan ve beyin dışı ile beynin kendisinden gelen cevaba sahip olan iki algılayıcı pozisyonun optimize edilmesi için gerçek fMRI datası Monte Carlo benzetimleri kullanılarak saptanmaya çalışılmıştır. 7 mm'lik bir insan kafatası kalınlığı için bu algılayıcı pozisyonlarının kaynaktan 17, 18 ve 19 mm uzaklığında olduğu bulunmuştur.

TABLE OF CONTENTS

LIST OF FIGURES

LIST OF TABLES

LIST OF SYMBOLS

n	Index of Refraction
μ_a	Absorption coefficient of the tissue
μ_s	Scattering coefficient of the tissue
μ'_s	Transport Scattering Coefficient
g	Anisotropy Factor
d	Layer Thickness

LIST OF ABBREVIATIONS

fNIRS	Functional Near-Infrared Spectroscopy
NIR	Near-Infrared
MCML	Monte Carlo Simulations for Multi Layered Media
TD-MCML	Time Dependent Monte Carlo Simulations for Multi Layered Media
CSF	Cerebro-spinal fluid
MBLL	Modified Beer-Lambert Law
BOLD	Blood Oxygen Level Dependent
CBF	Cerebral Blood Flow
HbO_2	Oxygenated Haemoglobin
HHb	De-oxygenated Haemoglobin

1. INTRODUCTION

Being a non-invasive technique with a great potential to monitor the cerebral haemodynamics, functional near infrared spectroscopy (fNIRS) measurements have found many applications in the field of functional neuroimaging. The areas of study of fNIRS spans neuro-rehabilitation, neonatal care, understanding of disorders such as autism, schizophrenia, depression, chronic pain, stroke.

fNIRS measurements are taken over the scalp with a specifically designed probe that houses light sources and detectors placed in a geometry suited for optimal light collection reflected from the tissues. Although this non-invasive probing of brain activation is the greatest advantage of this technique, it also results in a difficulty of establishing the exact origin of the related haemodynamic response within the brain due to the presence of systemic fluctuations within the non-brain tissues (i.e. surface layers).

The absorption of light in the activated region of the brain is due to the variation in the blood volume and oxygenation, therefore the detection of the intensity change of NIR light passing through theses areas enables one to measure brain activation [5].

However, the light transmitted passes through the surface layers as it reaches the brain and hence the returning light contains information on the absorption variations of these layers as well. Therefore, fNIRS suffers from the following various limitations:

1. Physical Limitations
    (a) Modest spatial resolution
    (b) Limited penetration depth
    (c) Uncertainty of optical path
    (d) Contamination from non-brain tissues

2. Physiological Limitations

   (a) Lack of absolute quantification of Hb concentration

   (b) Contamination from systemic fluctuations

   (c) Sensitive to regions with lesser blood vessel density

Many attempts have been made to overcome these limitations. These attempts have focused on optimizing the probe geometry (placement of source detector pairs to minimize the interference from surface layers) and signal processing techniques (i.e. elimination of non-brain tissue variation by denoising algorithms). Literature survey has shown that a combination of these attempts actually offers a better solution to the issue of non-brain tissue contamination in fNIRS signals.

1.1 Near-Far Detector: Elimination of Non-brain Tissue Contamination

In order to obtain an accurate haemodynamic response of the evoked brain, one needs to make sure that they measure the changes only in the corresponding regions of the brain. However, the non-invasive property of the fNIRS technology makes the device susceptible to the contamination of the received signal by the superficial layers of the human head, namely; physiological signals from scalp and the skull which the received signal from the brain is coupled with. Vascular signals present in these layers obscure the vascular signal from the brain tissues [6].

Elimination of these signals is a problem of great importance and different approaches have been developed in order to overcome this limitation.

Our approach for the elimination of non-brain tissue contamination uses the technique of superficial signal regression (SSR) imposing an assumption that the superficial hemodynamic changes are homogeneously distributed across the scalp, which

allows an estimation of the measurement performed at one position of the scalp from the scalp data at another position.

The depth sensitivity of a detector depends on the source-detector (SD) distance. Relying on the diffusion theory for photon migration through multiple scattering media, from which analytical theory for the "bananashape" photon path distributions is obtained [7], one can understand how closely spaced source-detector couple gathers information from shallow depths, whereas, the pairs for which that distance is larger, the penetration will be deeper, resulting in a collective signal from all of the layers. Fig. 1.1 illustrates this penetration difference between two detectors where one is farther from the source than the other one.

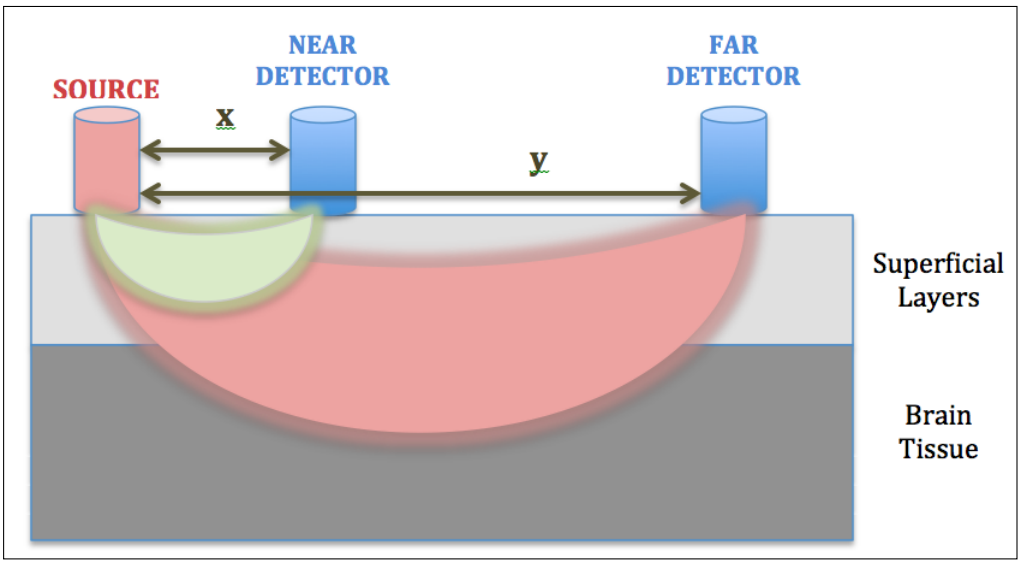

Figure 1.1 Near-Far Detector Signal Regression.

The aim of this thesis is to develop an algorithm in order to correctly assign near-far detectors using the data gathered from various simulation results where one detector (near detector) is only sensitive to scalp, skull, and systemic hemodynamic fluctuations, and the other (far detector) penetrates to the layers of the brain, most importantly the grey matter which is the region of interest 1.1. By subtracting the signals from these optimized two detectors, we aim to produce a more accurate estimate of the haemodynamic response corresponding to the evoked brain activity, which can be formulated as follows;

$$S_{far} = S_{noise} + S_{brain}, \tag{1.1a}$$

$$S_{near} = S_{noise}. \tag{1.1b}$$

then regressing the noise of superficial from the far detector data as;

$$S_{brain} = S_{far} - S_{near}. \tag{1.2}$$

Then in principle, this regression technique will provide a much more accurate measure of the brain activation.

In this thesis, a time dependent multi layered Monte Carlo (TD-MCML) simulation approach for mapping brain and scalp tissue absorbance attained from BOLD fMRI to fNIRS optical density (OD) changes as an initial step to i) facilitate the solution of finding an optimal NIRS probe geometry for monitoring brain hemodynamics and ii) eliminate non-brain tissue contamination in fNIRS signals is presented [4].

2. BACKGROUND

2.1 Functional Near Infrared Spectroscopy

fNIRS is a noninvasive imaging technique which uses the principles of near-infrared spectroscopy (NIRS), and it is widely used for the investigation of functioning human infant and adult cortex. This technology allows the indirect measurement of cortical activation that is coupled to functional haemodynamic responses to a variety of stimulations with an experimental set up which is both portable and inexpensive compared to other technologies used for brain studies and can be combined with other imaging modalities such as fMRI, EEG, PET and MEG. This technique shows great potential and continuous development in the field of neuroimaging [1]. Apart from being a completely noninvasive method, great temporal and relatively good spatial resolution, portability, the ability of a low-cost and low-power measurements are amongst the advantages over the other existing brain monitoring techniques. [3].

NIRS makes use of some basic facts of photon migration in tissues. One can list them as follows;

1. The range electromagnetic spectrum that is used in the NIRS (approximately 650 - 950 nm) is a region where the human tissues are relatively transparent, therefore this range is mostly known as "optical window" into the biological tissue, allowing the light at these wavelengths to penetrate several centimeters into the tissue where it still can be detected [3]. The absorption spectra of major tissue chromophores is the reason to why such region is selected for NIRS studies. Although many chromophores absorb light in the indicated spectral window, the oxygenation-dependent absorbance of the tissues by oxyhaemoglobin (HbO_2), deoxyhaemoglobin (HHb) -the two important markers brain activity- and oxidized form of cytochrome oxidase (CytOx) is what clinical NIRS studies mainly focuses on. A general absorption spectra of various human tissue chromophores can be

seen in a electromagnetic spectrum in Fig. 2.1, where Fig. 2.2 provides a deeper understanding of specific extinction coefficient for Hb, HbO_2 and CytOxin the NIRS monitoring region which are the main focus of the technology.

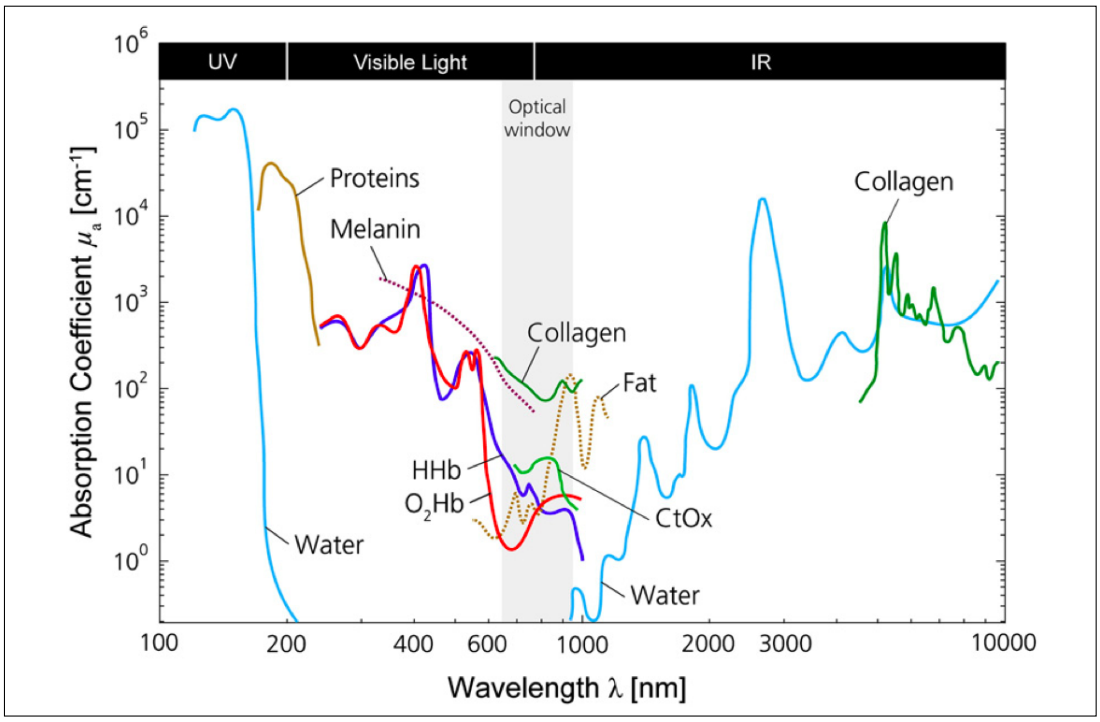

Figure 2.1 Absorption spectra for O2Hb, HHb, proteins, water, collagen, fat and cytochrome oxidase [1].

2. The possible interactions that NIR light can undergo is either absorption by chromophores or scattering in tissues. Absorption is from both chromophores of fixed concentration and absorption from chromophores of variable concentration, the quantification of the latter is what NIRS is mostly concerned with.

3. Due to the dominance of the probability of scattering (about 100 times more probable than absorption [2]), NIR light can penetrate through the human tissues. This property of tissues enables one to measure the amount of light that reaches the detector.

4. Haemoglobin is the main chromophore found in small vessels such as capillary, arteriolar and venular beds, therefore NIR light in tissues have relatively high attenuation. However, since NIR light is completely absorbed for vessels with

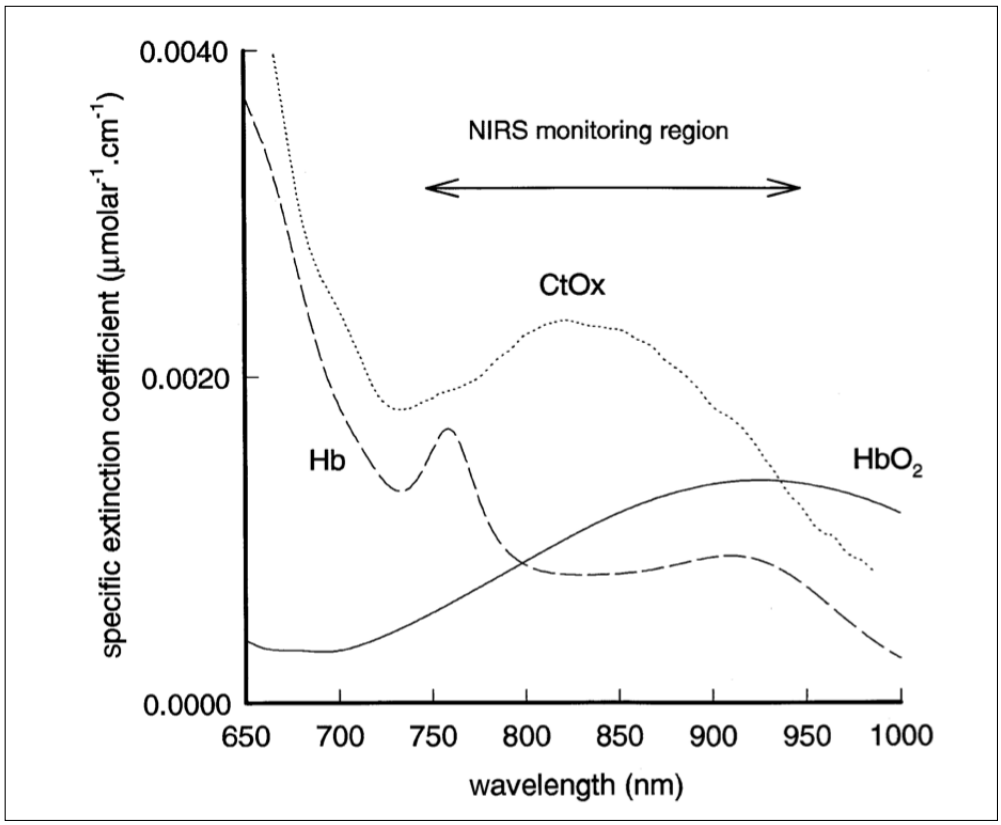

Figure 2.2 Specific extinction coefficient for Hb, HbO_2 and CytOx (oxidized minus reduced) in the NIR [2].

diameter larger than 1 mm, the technique is weakly sensitive to blood vessels with larger diameters.

Thus, NIRS wavelength range can propagate relatively easily through tissue non-invasively, and the absorption information reveals the activation in the brain.

Changes in absorption coefficients in brain and scalp tissues are caused by blood pressure changes such as heart beat, breathing etc. called Mayer Waves. However, the changes in the absorption coefficients of the gray matter where the neural activation occurs is caused by the heamodynamic response of the brain.

One wavelength per chromosome must be used for resolving their in order to determine the contribution of multiple chromophores Therefore for NIRS measurements least two different wavelengths of electromagnetic radiation during fNIRS experiments

are selected for a more accurate measurement of HbO_2 and HHb attenuation changes.

The measurement of the change in the intensity of detected light, the molar extinction coefficients of HbO_2 and HHb and the calculation of the partial optical path length which the detected light travels in the activated region by solving the simultaneous equation based on the modified Beer-Lambert law enables one to calculate the concentration change in oxy- and deoxyhemoglobin independently [8].

2.1.1 Modalities of NIRS

NIRS technologycan be utilised in three different modalities. Each of these three techniques are based on a specific type of illumination;

1. Continuous Wave (CW) Modality: This technique is realised by a constant illumination of the biological tissue at a constant intensity, giving an information only about the light attenuation through the layers of the head. The technique relies on measuring the change in the intensity of the light passing through the media.

2. Frequency Domain (FD) Modality: In this method one can obtain information on both attenuation and phase delay of the light leaving the tissue by selecting intensity-modulated light for the illumination. This technique provides information on the absorption and scattering properties of the underlying tissue compartment.

3. Time Domain (TD) Modality: By the illumination of the head with extremely short pulses of light, this technique provides the shape of the pulse after propagation through tissues. Time of flight measurement provides the choice of penetration depth of light in the tissue compartment.

The first modality, CW, is the most commonly used technique which takes advantage of a Modified Beer-Lambert Law (MBLL) for the calculation of the oxy-

genation changes of HbO_2 and HHb with respect to a previously set initial value. Also this technique show advantages of low cost and portability.

On the other hand, although the FD and TD modalities have much increased cost and higher technological complexity, these are the only NIRS techniques that promise a pure characterization of the optical properties of tissues from which one may extract knowledge about absolute HbO_2 and HHb concentrations for which a detailed explanation is provided by Scholkmann et al [1].

Measurement Type	Advantages	Disadvantages	Example Uses
Time domain	Spatial resolution Penetration depth Most accurate separation of absorption and scattering	Sampling rate Instrument size/weight Stabilization/cooling Cost	Imaging cerebral oxygenation and hemorrhage in neonates, breast imaging
Frequency domain	Sampling rate Relatively accurate separation of absorption and scattering	Penetration depth	Cerebral and muscle oximetry, breast imaging
Continuous wave	Sampling rate Instrument size, weight and simplicity Cost	Penetration depth Difficult to separate absorption and scattering	Finger pulse oximeter Functional brain experiments (as per fMRI)

Figure 2.3 Characteristics of NIRS Modalities [3].

2.1.2 Haemodynamic Correlates of Neural Activity

In a response to an external stimuli, an electrical signal is conducted between nerve cells, leading to neuronal activity which is a process that requires oxygen. Therefore, during this process the increased demand for oxygen is provided by the local increase of cerebral blood flow (CBF), predominantly in gray matter, resulting in increased amount of oxygen delivery to the oxygen-deprived cells.

Following this neuronal activation, a haemodynamic response is situated where an increase in oxy-haemoglobin HbO_2 is observed accompanying a decrease of deoxy-haemoglobin (HHb) (relatively less than the increase of HbO_2) indicating an increase in local arteriolar vasodilatation, which increases local cerebral blood flow and cerebral

blood volume and this mechanism known as *neurovascular coupling*. This mechanism results in the change in the absorption at a given wavelength and thereby the NIR-light attenuation, and this provides a method for the investigation of the differential absorption of near-infrared light by HbO_2 and HHb which this technique which relies on because the concentration change of these chromophores is recognised as an indicator of the brain blood flow variation [9].

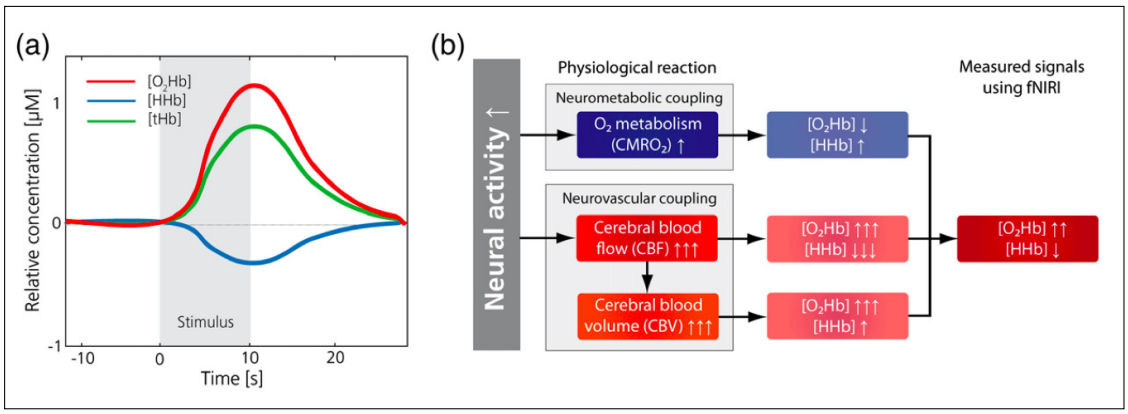

Figure 2.4 (a) Changes in cerebral oxygenation and haemodynamics due to brain activity. (b) Cerebral hemodynamics and their effect on the NIRS signals i for an increased neural activity. [O2Hb]: oxyhemoglobin concentration, [HHb]: deoxyhaemoglobin concentration and [tHb]: total haemoglobin concentration[1].

NIR-light attenuation is proportional to mean path length of the light that transverses through the activated region, namely gray matter during cerebral activation. Thus, the sensitivity of fNIRS to detect changes in HbO_2 and HHb concentrations directly depends on the traversed gray matter volume and the mean partial pathlength through this tissue type. The traversed gray matter volume and the mean partial pathlength through this tissue type directly effects the sensitivity of the NIRS measurements [10].

Although near-infrared (NIR) light is absorbed also by other molecules in biological tissue such as melanin, this additional absorbance will not have an effect concerning the measurement of relative change in NIR-light absorbance since the concentration of those molecules (chromophores) will be constant during the haemodynamic response [11]. However, these biological tissues are heterogeneous in nature which gives them the property of high scattering as they interact with light. These resulting scattering

events increase the amount of possible paths for photon to follow during the light-tissue interactions and consequently only around 10^{-3} to 10^{-4} of the light reaches the detector which is at a position of 3cm from the source on the head surface of adults [10]. The average path of these photons from a NIR light source can be described as a "banana shaped" path where the penetration depth is reported to be about 2 cm to 3 cm [12].

2.1.3 Physiological Relationship between fNIRS and fMRI

The functional behaviour of the brain can be better understood by multimodal approach i.e. the combination of different brain monitoring techniques, since the response of the brain during its activation, processes of neuronal and synaptic activity, vascular dilation, blood volume and oxygenation changes are all intertwined [13]. The connection of the blood oxygenation level-dependent (BOLD) signal and the haemodynamic changes in the brain are studied by a combination of functional magnetic resonance imaging (fMRI) and functional near-infrared spectroscopy. Functional magnetic resonance imaging consists of using various MRI modalities for temporal changes in blood flow, blood volume and oxygenation measurements.

Brain activation mapping by fMRI relies on the measurement of hemodynamic changes occurring in the active region which is followed by neural activity. As a result of an increased neural activity a substantial increase in cerebral blood flow (CBF) is observed however they are accompanied by a relatively lower increase in cerebral metabolic rate of oxygen (CMRO2) resulting in a reduced oxygen extraction fraction (OEF) [14]. As a general rule for the combination of fMRI and fNIRS, the temporal correlation of the BOLD signal with changes in oxygenation is considered to be the underlying foundation [15]. And the assumption that the correlation between a change in the oxygenation (an increase in HbO_2 content) in blood and an increase in BOLD contrast allows one to investigate the neurovascular coupling further.

2.2 Photon Migration in Biological Tissues

As the NIR light is sent through scalp, skull, and subarachnoid space filled with cerebrospinal fluid, gray and white matter of the brain tissue respectively, each source-detector pair gives a spatial distribution of this transversing light with two narrow ends and a curved inward toward the center which is called *banana* shaped. The middle segment of this shape is where the photons reach the deepest part of the media which is shown in Fig. 2.5. In the core of this "banana-shape" region lies the maximum probability of re-emitted photon paths. The analytical expressions for the so called "banana-shape" is discussed elsewhere [16].

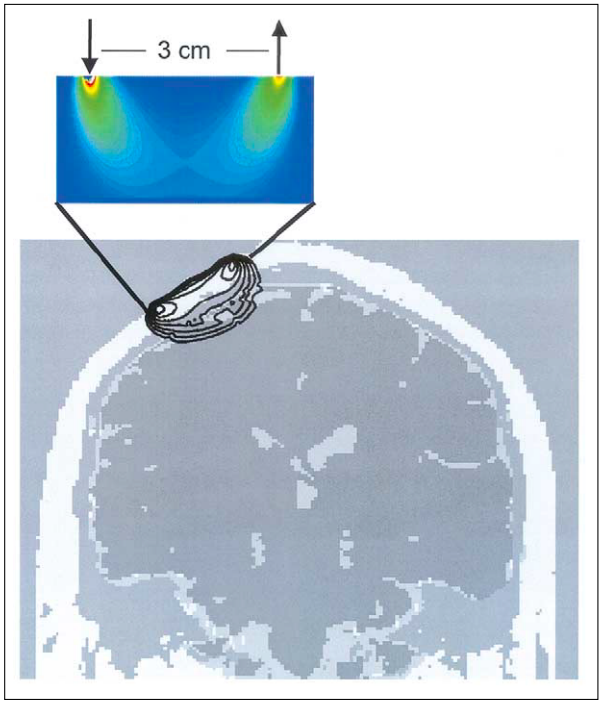

Figure 2.5 A sensitivity plot for light traveling in a homogeneous, highly scattering medium for a continuous-wave or frequency-domain measurement. Color indications: number of detected photons at any point in the homogeneous medium. White, red and yellow: high sensitivity region, blues and purples: lower sensitivity regions [3].

This kind of spatial distortion is caused by the optical heterogeneity of the head layers, however the partial optical path length in the gray matter is unaffected by this distortion because of NIRS sensitivity to brain activity [17].

2.2.1 Modified Beer Lambert Law (MBLL)

In order to quantify changes in concentrations of absorbing molecules, the light diffusing through the tissues must be modelled. Variations in the attenuation during a NIRS measurement can be converted into changes in the absolute concentration of a chromophore by the use of a Modified Beer Lambert Law (MBLL) which is an empirical description of optical attenuation in a highly scattering medium [18]. MBLL provides a proportionality between the concentration change and the logarithm of the detected light intensity during the change I divided by the light intensity prior to the change I_0.

$$\Delta OD(\lambda) = -log(\frac{I}{I_0}) \tag{2.1}$$

where $\Delta OD(\lambda)$ is the proportionality constant that is made up of a measure of the path length the scattered light actually traveled through the tissue, and the extinction coefficient of the absorbing species [3].

Accordingly, MBLL sets a relation between the change in measured optical density ΔOD and the change in concentration of oxyhemoglobin Δc_{oxy} and deoxyhemoglobin Δc_{deoxy} as follows [8].

$$\Delta OD(\lambda) = \left[\Delta c_{oxy}\epsilon_{oxy}(\lambda) + \Delta c_{deoxy}\epsilon_{deoxy}(\lambda)\right] \langle L(\lambda)\rangle \tag{2.2}$$

in which ϵ_{oxy} and ϵ_{deoxy} denotes the molar extinction coefficients of HbO_2 and HHb, and $\langle L(\lambda)\rangle$ is the mean optical path length of the detected light. Since the NIR light encounters many scattering events as it propagates through the medium, the mean optical path length becomes much longer than the optical distance between a source-detector pair.

Adding the assumption that the concentration changes take place only in the cortex during brain activation rather than a global change as assumed in the above equation 2.2, the intensity detected with NIRS instrument is given by [8];

$$\Delta OD(\lambda) = \left[\Delta c_{oxy}\epsilon_{oxy}(\lambda) + \Delta c_{deoxy}\epsilon_{deoxy}(\lambda)\right] \langle L_{cortex}(\lambda)\rangle \tag{2.3}$$

where $\langle L_{cortex}(\lambda)\rangle$ is the partial optical path length which is shorter than the mean optical path length.

Furthermore, in order to calculate the change in the concentration of oxy- and deoxy-hemoglobin separately, the change in intensity of the detected light at two wavelengths by solving the following simultaneous equation [8].

$$\Delta c^*_{oxy}(\lambda_1, \lambda_2) = \frac{\Delta OD(\lambda_2)\epsilon_{deoxy}(\lambda_1)\langle L_{cortex}(\lambda_1)\rangle - \Delta OD(\lambda_1)\epsilon_{deoxy}(\lambda_2)\langle L_{cortex}(\lambda_2)\rangle}{\left[\epsilon_{oxy}(\lambda_1)\epsilon_{deoxy}(\lambda_2) - \epsilon_{oxy}(\lambda_2)\epsilon_{deoxy}(\lambda_1)\right]\langle L_{cortex}(\lambda_1)L_{cortex}(\lambda_2)\rangle} \tag{2.4}$$

$$\Delta c^*_{deoxy}(\lambda_1, \lambda_2) = \frac{\Delta OD(\lambda_1)\epsilon_{oxy}(\lambda_2)\langle L_{cortex}(\lambda_2)\rangle - \Delta OD(\lambda_2)\epsilon_{oxy}(\lambda_1)\langle L_{cortex}(\lambda_1)\rangle}{\left[\epsilon_{oxy}(\lambda_1)\epsilon_{deoxy}(\lambda_2) - \epsilon_{oxy}(\lambda_2)\epsilon_{deoxy}(\lambda_1)\right]\langle L_{cortex}(\lambda_1)L_{cortex}(\lambda_2)\rangle} \tag{2.5}$$

and obtaining;

$$C_{oxy\to deoxy}(\lambda_1, \lambda_2) = \Delta c^*_{deoxy}(\lambda_1, \lambda_2)/\Delta c^*_{oxy}(\lambda_1, \lambda_2) \tag{2.6a}$$

$$C_{deoxy\to oxy}(\lambda_1, \lambda_2) = \Delta c^*_{oxy}(\lambda_1, \lambda_2)/\Delta c^*_{deoxy}(\lambda_1, \lambda_2) \tag{2.6b}$$

However, since concentration changes are not homogenous, the MBLL underestimates the size of the concentration changes in HbO_2 and HHb, therefore the approach requires further corrections as explained in [1].

2.3 Monte Carlo Method for Multi Layer Turbid Media

The Monte-Carlo method is a stochastic method that is based on random sampling of variables from probability distributions which is appropriate for the simulation of photon-tissue interactions along with the applications of a variety of other physical problems [19]. The simulations which offer a flexible yet rigorous approach to photon transport in turbid tissues, are able to score multiple physical quantities simultaneously.

The physical quantities to be simulated are photon absorption, fluence, reflectance and transmittance.

Launching of a photon to the tissue is the first step of the method. The coordinates of the photon are usually identical for all photons which allow convolution techniques to be used to determine fluence rates from a wide variety of beam shapes [20].

Photons are sent from the source and the photons that are;

1. Reflected
2. Absorbed, and
3. Transmitted

are recorded quantities where a grid system is set and the average value of the scored physical quantities in each grid element is provided. In the simulation program, the initial weight of photon packets is set to unity, which allows one to deal with a

relative fluence rates. The photon package is sent through the medium normal to the surface, then as they propagate, the total photon weight per grid element along the path of the beam is calculated via the recordings of photon deposition.

A multi-layered tissue is constructed as the medium where each layer is infinitely wide and, the thickness, the refractive index, the absorption coefficient are the parameters to be set. The simulation propagates photons in three dimensions, and a Cartesian coordinate system is used to trace photon packets [4].

The reflected photon fluence from the surface of the multi-layered model is of interest of this study since the detectors are placed on the surface of the scalp. The received number of photons on the pre-assigned detector positions gives information of the photon absorption by the in the oxygenated and de-oxygenated blood chromophores in the turbid media.

The simulation algorithm allows one to assign the optical parameters of the layers, which in our case are the tissues of the head layers, from outer to inner; scalp, skull, cerebrospinal fluid, gray matter and white matter. The parameters that one can assign to the layers are the thickness, scattering coefficient, absorption coefficient, anisotropy coefficient and index of refraction. And the photons sent into the medium can also be assigned.

Basic Assumptions

There are several assumptions used for the modeling of light propagation in a turbid medium. They are elaborated as follows;

1. One of the most basic assumptions is that macroscopical optical properties are assumed to extend uniformly over the small units of tissue volume,
2. Another important assumption is that the photons are treated as classical particles where the polarization and wave phenomenon are neglected

3. The modelled media are assumed to have homogeneous optical properties unless stated otherwise.

4. The tissue is assumed to have a uniform index of refraction is assumed for the tissues indicating a straight path for photons travelling until scattered or absorbed.

5. Also the boundaries between tissue layers are assumed smooth, which demonstrates a specular reflection according to Fresnel's law.

2.4 Mechanics of Photon Propagation

The photon package, which is a collimated arbitrarily narrow beam of photons, is introduced orthogonally to the multi layered media. Following the launching of the photon package, a photon has a range of possibilities after its propagation of a distance called step size Δs; the photon may be scattered, absorbed, propagated undisturbed, internally reflected within the previously defined layers, or may be completely transmitted out of the layers. Out of these probabilities, the absorption and reflection/transmission of the photon into or out of the tissue model ends in the recording of the relevant values, consequently allowing the launch of another photon into the media. This repeated process ends when the launch given number of photons is achieved.

As the number of photons propagated approaches infinity, the recorded reflection, transmission, and absorption values will approach true values (for a tissue with the specified optical properties) since the method is statistical in nature [21].

2.4.1 Coordinate Systems

In Monte Carlo simulations, what is basically done is tracing the photon packets and calculating their interaction as they propagate through the media that has been previously set. In order to quantify the interactions of the photon with the media at any spatial position, many different sets of coordinate systems can be described depending

on the purpose of the study. This thesis uses of the Monte Carlo Modeling of Light Transport in Multi-layered code written and published by Wang *et al*, therefore their coordinate system will be explained in detail [22].

In the simulations three coordinate systems used that are used simultaneously can be be listed as follows;

1. The cartesian coordinate system which is used to trace photon packets,
2. The cylindrical coordinate system the internal photon absorption are scored,
3. The moving spherical coordinate system for sampling of the propagation direction change of a photon packet.

The point where the incident photon enters the tissue is the origin of the cartesian coordinate system the xy plane constructs the surface of the tissue since the z-axis is defined as the normal to the surface at all times. The internal photon absorption A(r, z) score is obtained by the utilisation of the cylindrical coordinates where r and z denotes the radial and z-axis components of the system and this z-axis coincides with the z-axis with the cartesian coordinate system, and the origin is also shared. The radial component r of the cylindrical coordinates are also used for scored quantities; Diffuse Reflectance Rd(r,α) and Total Transmittance Tt(r,α) where α is the angle between the direction of the photon exiting and the normal of the tissue surface. The third coordinate system - Spherical Coordinate system, unlike the first two systems that are described, is a dynamic, in other words a ”moving” coordinate system constructed for for sampling of the propagation direction change of a photon packet. The z axis of the system is aligned dynamically with the photon propagation direction, and deflection angle θ and azimuthal angle ψ due to scattering are sampled then the direction with the use of the directional cosines in the Cartesian coordinate system is updated. Directional cosines are in essence are the cosines of the angle between photon's propagation axis and each of the Cartesian Coordinate axes, namely x, y, and z, and they

are denoted as μ_x, μ_y, and μ_z respectively [21]. For a distance Δs that the photon is travelled from points (x, y, z) in the direction (μ_x, μ_y, μ_z), the new coordinates will be obtained by;

$$x' = x + \mu_x \Delta s \tag{2.7a}$$

$$y' = y + \mu_x \Delta s \tag{2.7b}$$

$$z' = z + \mu_x \Delta s. \tag{2.7c}$$

2.4.2 Optical Parameters

In Monte Carlo methods, the propagation of each photon is described individually which is the source of the methods' precision and it makes use of rules that take the physical phenomena of photon propagation in tissue into account. These can be listed as follows;

1. the absorption probability of a photon,
2. the probability of the interaction of the photon with the medium which gives a new direction to the photon path described as scattering probability,
3. the reflection probability for a photon as it meets a boundary between two different tissues,
4. a rule giving the new direction of the photon after a scattering event which is mostly known as a phase function,

as it propagates through the tissue.

2.4.2.1 Absorption and Scattering Coefficient: μ_a and μ_s

A simple definition of the absorption coefficient μ_a can be given as the probability of photon absorption per unit infinitesimal pathlength and similarly scattering coefficient μ_s indicates the probability of photon scattering per unit infinitesimal pathlength [22].

2.4.2.2 Probabilistic Photon-Tissue Interactions: Henyey-Greenstein Phase Function and Anisotropy Factor: g

During a photon-tissue interaction, the photon will either be absorbed or scattered by the matter. The scattering case is a more complicated process than the absorption since there is a probability that the scattering angle, θ can take any value from which new direction for the photon is determined. Therefore one of the most critical points in MC simulations is to define the new photon direction after each scattering event. This scattering profile is called the "phase function" although it has no relation with the phase of the light waves. The most popular solutions to this problem is to use the Henyey-Greenstein phase function defined for galactic scattering for the modelling of the probabilistic photon scattering in biological tissues. This phase function provides a probability distribution can be written as;

$$P_{HG}(\theta) = \frac{1}{4\pi} \frac{1 - g^2}{(1 + g^2 - 2gcos(\theta))^{\frac{3}{2}}} (2.8)$$

which is described by Binzoni et. al. [23] where $P_{HG}(\theta)$ is a probability density function and $\theta \ \epsilon[0, \pi]$ (rad) is the angle between the direction of the incident photon and the scattered photon. The parameter g quantifies the anisotropy of scattering by $g = \langle cos\theta \rangle$

The derivation of the phase function is explained in detail in the work of Henyey and Greenstein [24].

2.4.2.3 Transport Scattering Coefficient: μ_s'

Depending on the anisotropy factor of the tissue, scattering is strongly affected thereby reducing the scattering coefficients of tissue and a new parameter Transport (or Reduced Scattering Coefficient: μ_s' is deduced from the diffusion approximation of the radiative transport equation as follows; defined by:

$$\mu_s' = (1 - g)\mu_s \tag{2.9}$$

For values of g close to 1, which implies a very forward scattering, the value of μ_s is very much reduced. As it will be detailed in Chapter 3, the experimental data of μ_s' will be used for characterisation for optical parameters of tissue layers rather than the Scattering Coefficient μ_s itself.

2.4.3 Scored Physical Quantities

In the output file provided by the program, regardless of the number of photons used for the simulation, the weight of the photons are given which prevents a possible confusion that the user may have while carrying out an analysis on simulations with variety number of photons. The photon package sent into the media is always 1, and the scored quantities are given by a radio of this weight instead of the number of photons.

The simulation used for this thesis records reflectance, transmittance and absorption.

2.4.3.1 Diffuse Reflectance R_d and Transmittance T_t

Right after the photon package is sent into the media, the weight is immediately reduced by the computation of specular reflectance and subtraction from the initial weight 1. Then the remaining weight of photons resume to propagate through the media.

There are two possibilities of the photon leaving the tissue; first one is when the photon departs from the uppermost layer from where it has entered and it is described as Diffuse Reflectance R_d and the second is when the photon leaves from the bottom layer described by Transmittance T_t

2.4.3.2 Internal Photon Distribution

The basic unit of length is taken to be cm for the optical and structural properties of the tissue model, such as grid elements of r and z, thicknesses of layers. Since the absorption and scattering coefficient represent, as described earlier in the section, probability of photon absorption per unit infinitesimal pathlength, these quantities have the unit of cm^{-1} for convenience.

2.4.4 Flowchart of Photon Tracing

Since the optical properties of tissues, possible light-tissue interactions and recorded physical quantities during the simulation are defined and described, it is appropriate to introduce the their implementations in a flowchart in Fig. 2.6. More details of the photon tracing are explained further in the manual for the Monte Carlo Simulation program used in this thesis [22].

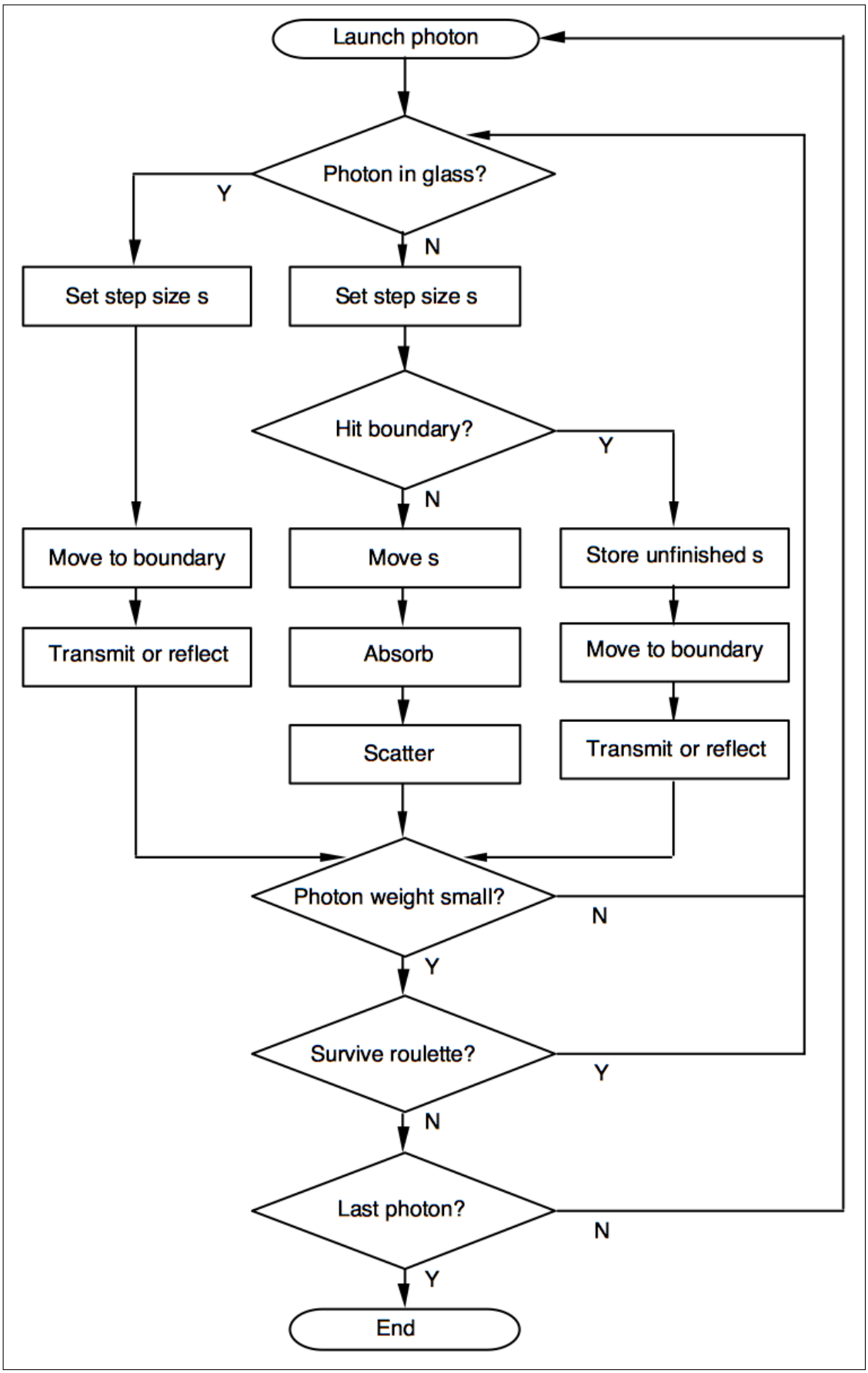

Figure 2.6 Flowchart for Monte Carlo simulation of multi-layered tissue [22].

3. METHOD

3.1 Modelling of Photon Migration In Multi Layered Turbid Media

3.1.1 Optimization of Simulation Parameters for a Realistic Model

The simulations were run by the program (MCML) Monte Carlo for Multi-Layered media provided publicly by the Oregon Medical Laser Center [25]. The Monte Carlo Simulation code used in this thesis, allows the user to adjust the parameters regarding the tissue model which is designed to mimic the real tissue under investigation and the parameters regarding the photon migration. Prior to the simulation, the user provides a rather simple input text file in which all of the adjustable parameters are set, and then this input file is introduced to the code.

These adjustable parameters can be grouped under two major categories; parameters that describe the fNIRS probe and those that describe the tissue. Since the purpose is to construct a model of the experimental set up of the fNIRS probe strapped around a human head, one has to specify the properties of the probe which are; the detector positions, number of photons sent to the media, number of simulation runs, dimensions of the grids (dz and dr).

Since the method is statistical in nature, the number of photons and simulation runs have to be assigned depending on the accuracy that is required for the specific investigation. To make this easy to perceive, Wang *et al* describes a good statistics by adjusting the number of photons to 10^5 ([20]) and in several studies this number varies from 10^5 to 10^8 [21], [20], [10]. However this number depends on the complexity of the model of the tissue that is also described i.e.; the more complex the tissue model, the larger amount of the photons may be required. As mentioned earlier while describing the MCML, a disadvantage of the method is the computation time that

increases with the increasing number of photons and the complexity of the media (due to path length that the photons travel), therefore, there will be a compromise between a good statistical result and a reasonable computation time which is achieved mostly by trial and error.

For the latter category that describes the tissue, the characterisation is achieved by assigning macroscopical optical parameters which are assumed to expand uniformly over the tissue model and geometrical specifications. The properties can be listed as; the layered structure of the model (number of layers and their thicknesses), index of refraction, absorption and scattering coefficients of the tissue at a specific wavelength, anisotropy factor. In one of the following sections 3.1.1.2, these parameters are discussed in more detail.

3.1.1.1 Probe Model

Photon Packages and Number of Simulation Runs

The first step for an accurate description of the system was the optimisation of the number of photons that were sent from the photon source statistically. It is theoretically expected that as the number of photons in the photon package sent increases, the standard deviation at the detector site will decrease. Yet one of the few disadvantages of MCML simulations is their relatively long time of computing compared to other similar techniques. Therefore, the user of the program must decide on an optimisation, which ensures achievable precision and accuracy of the output data in a reasonable period of time which is of great importance for the reliability of the technique.

Various studies have been conducted with different number of photons ranging from 10^5 to 10^8, therefore in order to find the optimised number of photons, the simulations were performed for three sets of photon numbers, for ten individual runs. These numbers were selected to be; 10^5, 10^7, 10^8 photons, which are the commonly used val-

ues for the MCML simulations of the photon propagation in brain tissue studies. The resulting photon intensities at the pre-located detectors, namely *Diffuse Reflectances* were analysed for each of these numbers, and for each of the ten simulation runs which revealed a statistical information of mean, standard deviation, hence the coefficient of variation.

Lastly, the number of photons in the photon package for which the standard deviation and coefficient of variation is at a reasonable degree with respect to computation time, were selected for the rest of the simulations. Once this number is decided on, the photon migration was simulated through the media for a set of head models, which various optical parameters and geometrical properties were previously assigned for.

Detector Positions

Diffuse Reflectance information was collected at 100 different points on tissue surface with increments of 1mm away from the source. These points represent detectors on fNIRS probe. A 100 points of detection with 1mm apart means that the distance between the photon source and the last detection point is 10cm, however in practical case where fNIRS probe is placed on the forehand for prefrontal cortex haemodynamics measurements, this distance is unrealistic, even more, it is claimed that for fNIRS measurement of the evoked brain activity, the depth sensitivity is quite low for a source-detector distance larger than 30 mm [10]. Also, the statistical noise of the simulation becomes important after around these distances.

Most importantly, the aim of this thesis is to eliminate non-brain tissue contamination by assigning a near-far detector position, and both of these detector positions are suggested to be between a source detector distance of 3cm where the banana shaped photon distribution contains information on the Gray Matter haemodynamics. It is also indicated that once the source-detector separation exceeds 30 mm the partial mean optical path lengths of the Gray Matter layer change slowly since at these distances, the detected light passes mainly through the CSF layer, preventing it to reach deeper

into the GM [26].

Therefore, although the complete points of detector outputs were readily available and was provided in the graphs, the part of the near-far detector investigation was mainly shown in a scale where the distances larger than 30 mm for the source-detector separation is omitted. This approach prevents the statistical noise effects shadowing the desired signal information.

The arrangement of the detector positions in our model was built according to the the spatially resolved spectroscopy approach [1]. For a good approximation to the practical fNIRS probe, instead of including complete detector positions at every mm inside the 3-cm source-detector separation, the Diffuse Reflectance at the source-detector pair in 0.5-cm increments along the surface of the head was used as previously studied by Strangman *et al* [27]. A drawing of the detector positioning along with the general head model can be seen in figure 3.1.

3.1.1.2 Description of Head Model for Photon migration Simulations

Firstly, a simulation with a model with one thick homogeneous layer medium is performed in order to assure that the MCML works properly for our purposes. The expected behaviour of the photon Diffuse Reflectance is an exponential decrease in intensity as the detector distance from the source increases due to the absorption events in the medium. Then new layers with different optical parameters was introduced for a new set of simulation and the purpose of this was to observe the depth sensitivity profile that is theoretically derived. Specifically, the head model in order to better mimic a realistic human head the alterations were made.

In order to simulate the photon migration in adult head, a simplified model of a slab consisting of five layers which mimic the optical properties of scalp, skull, subarachnoid space, gray matter and white matter (from outer to inner) is constructed. Thicknesses of these layers are taken to be 3.0, 7.0, 2.0, 4.0, 3.4 mm as shown in figure

3.1, respectively relying on a recent study using a similar approach [28]. A simplification made on the model is the exclusion of the geometries of the sulci which is found to have an insignificant effect the optical path in the adult head [26].

The MCML calculates the output of the reflected beams at each mm in distance as if arranged as a continuous linear set of detectors which allows the user to acquire the information at any detector distance. However in practice, the detector distances in an fNIRS device is preset, therefore the detectors in Fig. 3.1 are merely representative and the positions used for the analysis are varied depending on the purpose of the investigation. Yet the farthest detector position used for the analysis in this thesis is usually 30mm since spatial sensitivity profile for detector spacing larger than this distance is claimed to be statistically insufficient for the measurement of haemodynamics of the gray matter [26].

The Cerebrospinal Fluid Layer

Although, a near-far detector approach concerning the structure of cerebrospinal fluid (CSF) layer will be introduced in a later section (3.3.1), a brief explanation may become handy while discussing the head model for the simulations. This layer differs from the other head and brain tissue layers in terms of absorption. A major absorber of tissues of the head; haemoglobin is not found in a normal CSF layer, therefore its content does not contribute to the change in the intensity of the photons received at detector positions.

However, one must treat the structure of this layer with caution since the light propagates without diffusion in the CSF acting according to the radiosity equation which is investigated in detail in works of Firbank *et al* [29], therefore playing a great role in light propagation, acting as a tunnel as light reaches this layer, enabling the photon to reach deeper layers of the brain which in return improves the depth sensitivity of the method also due to it low absorbance, increases the intensity of photons detected at large distances therefore improving the statistics [26]. In the same work of Okada *et al*, it has been pointed out that CSF layer affects light propagation in the adult head

beyond the source-detector distance of 15 mm, which is a region of great interest in this study.

Relying on these findings, through the end of the near-far detector analysis the thickness of the head model layers were slightly changed, however the CSF layer was kept intact. This analysis will be discussed in more detail in section 3.3.1

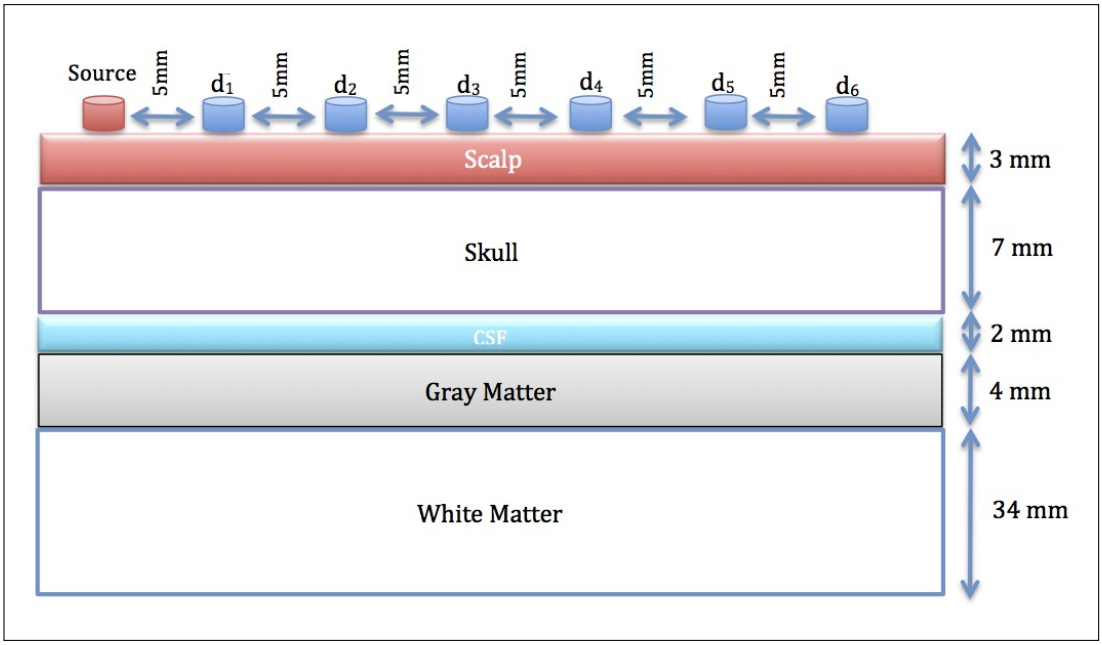

Figure 3.1 Simulation geometry with five layers and the positions of the optodes.

Choice of Wavelength

In order to assign optical parameters to tissues which are imitated by the head model, a certain wavelength must be chosen for the photon beam. The fNIRS probe under investigation uses dual-wavelength for the purpose of eliminating the undesired effect of Cross Talk which is explained in detail in section sec:MBLL. Although the selection lower wavelength of this dual-wavelength couple shows variety in previous studies, the longer wavelength of 830nm is most commonly used [8], [27], and therefore throughout the analysis, the Absorption Coefficient μ_a, and Scattering Coefficient μ_s of the tissues were assigned accordingly.

Absorption Coefficient μ_a, and Transport Scattering Coefficient μ_s'

Recent studies by Binzoni *et al* and Haeussinger *et al* had shed light on the topic of the effect of anisotropy factor g on randomly generating the angle defining the new direction of a photon after a collision.

During MC simulations, the g dependent value of μ_s' is used instead of μ_s assuming isotropic scattering (g=0) instead of anisotropic (g=0.9) scattering which is the case in brain tissues of GM and WM.

This approached used and investigated by Haeussinger *et al* and Binzoni *et al* gives the user an advantage of reduced MC calculation time [10], and most importantly, is not vulnerable to scattering angle calculation errors as described in detail by [23].

Absorption Coefficient μ_a and Transport Scattering Coefficient μ_s' of the living tissue mainly depends on the wavelength of the beam that is propagates through the tissue. The values of layer optical parameters for the selected wavelength of 830nm are shown in Table 3.1. This data of μ_a, μ_s' and thicknesses of modelled layers was provided by the reported data of experimental studies on dermis [30], pig skull [31] and human brain [32] in the light of a cross talk study conducted by Okui *et al* [8].

Table 3.1
Absorption Coefficients, Transport Scattering Coefficients and Thicknesses of Tissue Layers used for Simulating Photon Propagation at 830nm.

	830 nm				
	Scalp	**Skull**	**CSF**	**GM**	**WM**
$\mu_a(mm^{-1})$	0.019	0.017	0.0056	0.041	0.018
$\mu_s'(mm^{-1})$	1.84	1.47	0.22	2.1	8.82
Thickness (mm)	3	7	2	4	34

3.1.2 Introducing Arbitrary Inhomogeneities in the Medium

The optical properties of the tissues are assigned based on the selected wavelength for the simulations. However merely inserting these values into an input file and performing a simulation does not provide one with information on a functioning brain since during cognitive task, these values especially the absorption coefficient $_a$ change due to the oxygenation changes in Scalp, Skull and the brain tissues GM and WM because of the tissues' haemoglobin content. Since in a normal CSF layer haemoglobin is not found, such alterations were never carried out for this layer . It may be appropriate to mention that the μ_s' of the layers were kept constant since absorption changes are predominantly induced by changes in the concentrations of haemoglobin content, whereas the relation between changes in the HbO_2 and HHb are scattering changes within the head is not completely apprehended [3].

In order to see whether these changes and the attenuation of the light have a linear dependence, a set of models with various μ_a changes in percentages was introduced with increments of 5% from -20% to +20%. These changes were implemented on gray matter layer only for a more simplified model. A symmetry between these values were investigated also.

A more complex, hence a more accurate approach for the observation of haemodynamic response, namely a realistic change both in scalp and gray matter layers was also proposed and will be described in following sections.

3.1.2.1 Inhomogeneity in Whole Gray Matter Layer versus Partial Inhomogeneity in Gray Matter Layer

The increments of 5% change from -20% to +20% in gray matter were implemented in two ways; firstly, as percentage changes in μ_a of a 1mm thick layer inside the GM layer mimicking a blood vessel oxygenation that resides inside GM, leaving the rest of the GM layer (3mm) μ_a unchanged, and secondly as percentage changes in

μ_a in the entire GM layer of 4mm. In both methods, the relative intensity curves were obtained via the division of attenuation curves where a change was carried out by a baseline where μ_a was not objected to percentage changes.

The results were compared in order to gain insight on whether the detected fNIRS signal is sensitive to changes in such thin layers or the measurement is responsive to wider spatial arrangements. From this point on, instead of observing relative detector positions, the diffuse reflectance was analysed for the entire detection points.

3.2 An Approach for Realistic and Time Dependent Inhomogeneities in the Medium: Translating fMRI to fNIRS

In order to work with a more realistic model of the human brain activation to a given task, a novel approach combining fMRI and fNIRS is proposed [4].

An asynchronous measurement of the human brain response by fMRI and fNIRS using the same breath hold task. A sponge-like probe housing was placed on the subject's forehead with all the LEDs and detectors removed and their positions replaced with vitamin E gel capsules to mark source and detector locations on the MRI images. Following the registration of source and detector locations on the subject specific head model a set of techniques are used for obtaining fMRI blood oxygenation level dependent (BOLD) signals described in detail elsewhere [4].

Using a wavelength dependent expression derived from MBLL explained in earlier sections;

$$\Delta OD^{\lambda}(t) = -\log(\frac{I}{I_0}) = \Delta\mu_a^{\lambda}(t)\left\langle L^{\lambda}\right\rangle \tag{3.1}$$

where ΔOD is the change in the optical density due to a change in the tissue absorbance ($\Delta\mu_a$) and L the mean optical path length of photons traveling from the source to a far away detector.

The method presented in this section assumes that a time dependent fMRI BOLD signal changes which was quantified as a percentage change in the oxygenation of tissue layers with respect to a baseline, can be interpreted as μ_a changes in the corresponding areas of the tissue. By rewriting Eqn. 3.1 in the light of explained approach;

$$\Delta\mu_a^{\lambda}(t) = \Delta\mu_a^{\lambda}(0)(1 + \Delta BOLD(t)) \tag{3.2}$$

was obtained [4].

3.2.1 BOLD Signal Data Implementation Only on Gray Matter Layer versus Implementation on Gray Matter and Scalp Layer Simultaneously

BOLD signal provided by the fMRI measurements can be seen in Fig. 3.2 where during the breath hold task shown as a shaded area in the figure both Scalp and gray matter seems to undergo a slight deoxygenation followed by a significant increase. The quantitative values of the percentage changes are given in Table 3.2.

From 25 time dependent (TD) percentage changes of the BOLD data provided by fMRI, 9 of them were selected in increments of two seconds until the stimulus begins and three seconds after the stimulus in order to avoid unnecessary simulation time loss since most of the values were did not show significant difference (see Table 3.2).

These selected time points, which will be referred to as "Time Labels", are the time structure of the time dependence analysis. The adjusted absorption coefficient

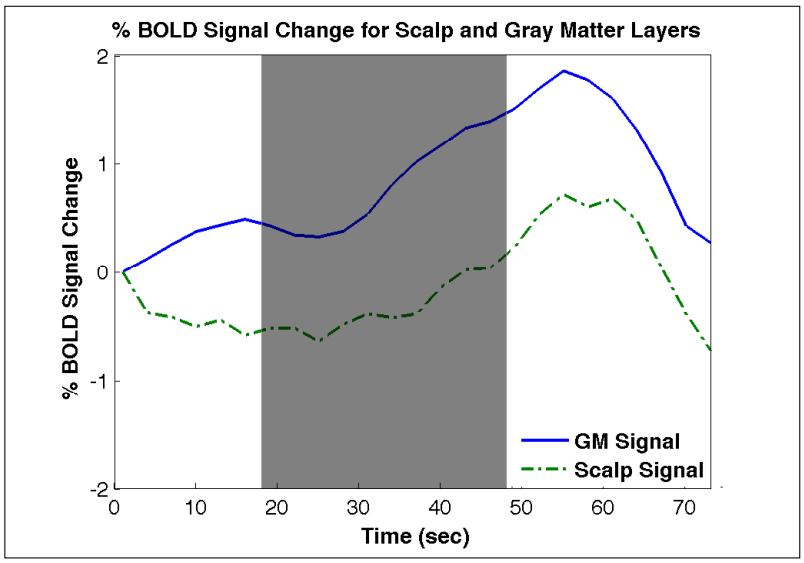

Figure 3.2 Percentage Changes of BOLD Data in Scalp and Gray Matter. Shaded area indicates the time period of the breath hold task (30 seconds) [4].

values at each time label were inserted in simulation input file and analysed for each time label in a following manner;

1. In one set of simulations, only the values for GM μ_a provided by the table 3.2 were used and the scalp μ_a remained constant,

2. The same set of simulation were performed again but with both scalp and GM μ_a values.

Then the behaviour of attenuation were observed for both these sets of simulations and the two sets were compared in order to test for spatial sensitivity of the detectors the scalp sensitivity respectively.

Time 2 was chosen as a baseline for the fNIRS simulations since this point stands right before the stimulus, then the attenuation for entire time labels were divided by the baseline attenuation curves (at Time 2) in order to convert the series to a time dependent measurement.

3.3 Optimal Probe Geometry Algorithm: Near-Far Detector

3.3.1 Verification of Far-Near Detector Positioning: Thin Skull Layer Approach

Following the analysis of BOLD data implementation on head model, as a validation tool for the near-far detector investigation, a set of simulations based on a head model where the skull thickness is altered in order to imitate a model where the gray matter layer is closer to the surface. Since the basic assumption is that as the source detector separation increases, the photons detected at those detectors would have information from a deeper layer [16], the change in GM can be seen with detectors relatively closer to the source.

For this purpose, however, the thickness of the subarachnoid space is kept constant since it is filled with cerebrospinal fluid, making it a low-level scattering media which therefore strongly affects the light propagation in brain [28].

3.3.2 Detector Clustering

The Monte Carlo Simulation Code used for this thesis [22] allows the user to obtain the Diffuse Reflectance at detector positions with centres that are 1mm apart. However, these data points that are collected at those grid elements are merely an average of detected intensities therefore an averaging tool was required.

More importantly, the detectors inserted in the fNIRS probe during measurements have the dimensions of 2.5 x 2.5 mm^2 which indicates that reporting the data for smaller detector areas as provided by the program, may be inadequate for an accurate estimation of the real model. Therefore, a moving average method was used, where instead of inspecting the data at each point given by the program, detectors were grouped in groups of three which will be referred to as “detector clusters” from here on.

These clusters are interrelated in such a fashion that each cluster of three detector points has two consecutive detector points in common with the adjacent clusters. To elaborate, Cluster 1 is the group of detector point values 1-2-3, and the next cluster, Cluster 2, has detector points 2-3-4. Therefore one has N-2 number of clusters, where N is the number of detectors that are being investigated. Although, all 100 points of detector values were analysed and plotted, the first 30mm of source-detector distance were emphasised since the statical noise beyond these points shadows the main trend which will be taken as the indicators of near and far detector positions. A simple illustration of the cluster pattern is given in Fig. 3.3

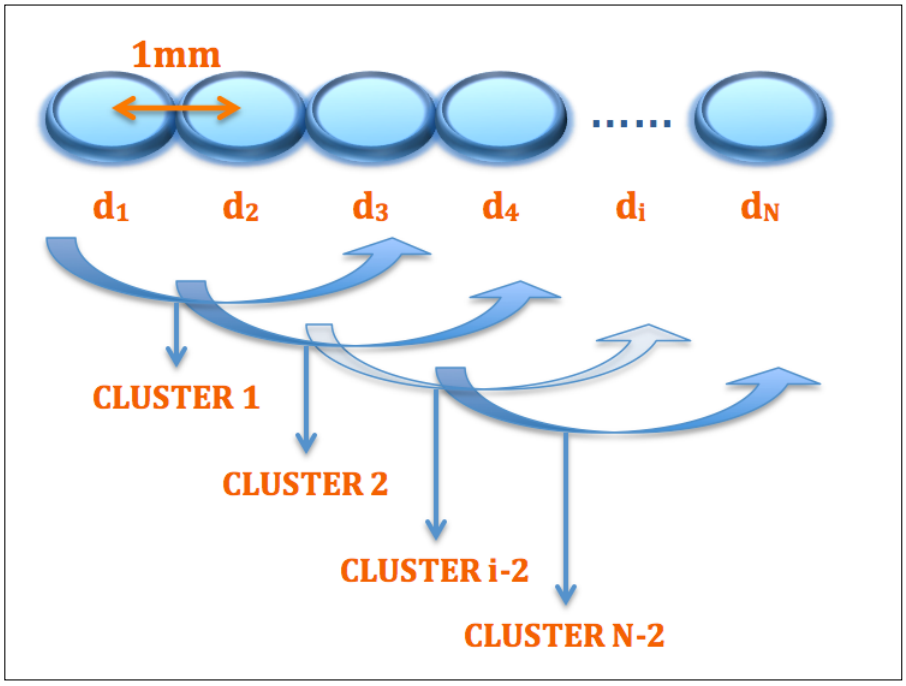

Figure 3.3 Detector Cluster Formation.

The data gathered from these clusters are basically three values of detector points, and in order to examine the relation both in between detector clusters and also the detector points within one detector cluster, a straight line was fitted to those three values and the slope of this line was calculated. This slope was expected to provide an information on a trend of the increase of the attenuation, from which one might observe discrete jumps in their plot indicating a switch to another media with different μ_a.

The reason why these clusters are formed as such, is due to the fact that, the exact positions where a cut-off value cannot be found in a case when each cluster is independent of an adjacent one, then instead of observing a gradual increase in slopes with distinct jumps, one would have many peaks in between the clusters.

Table 3.2
Percent Changes in fMRI BOLD Data and Corresponding Time Dependent (TD) Absorption Coefficients Values.

	% Mua Change		TD Value (mm^{-1})		
Time (sec)	**GM**	**Scalp**	**GM**	**Scalp**	**Time Label**
1	0	0	0.0410	0.0190	**Time 1**
2	0.1240	-0.3755	0.0411	0.0189	
3	0.2556	-0.4159	0.0411	0.0189	**Time 2**
4	0.3758	-0.5039	0.0412	0.0189	
5	0.4351	-0.4428	0.0412	0.0189	**Time 3 (stimulus)**
6	0.4884	-0.5830	0.0412	0.0189	
7	0.4301	-0.5185	0.0412	0.0189	
8	0.3444	-0.5141	0.0411	0.0189	**Time 4**
9	0.3264	-0.6384	0.0411	0.0189	
10	0.3778	-0.4842	0.0412	0.0189	
11	0.5356	-0.3850	0.0412	0.0189	**Time 5**
12	0.8084	-0.4209	0.0413	0.0189	
13	1.0192	-0.3864	0.0414	0.0189	
14	1.1694	-0.1408	0.0415	0.0190	**Time 6**
15	1.3313	0.0189	0.0415	0.0190	
16	1.3923	0.0383	0.0416	0.0190	
17	1.5110	0.2317	0.0416	0.0190	**Time 7**
18	1.6961	0.5323	0.0417	0.0191	
19	1.8574	0.7166	0.0418	0.0191	
20	1.7714	0.6030	0.0417	0.0191	**Time 8**
21	1.6026	0.6775	0.0417	0.0191	
22	1.3075	0.4752	0.0415	0.0191	
23	0.9132	0.0385	0.0414	0.0190	**Time 9**
24	0.4277	-0.3870	0.0412	0.0189	
25	0.2726	-0.7234	0.0411	0.0189	

4. RESULTS and DISCUSSION

4.1 Optimized Simulation Parameters

4.1.1 RelativeDetector Positions

The number of photons reaching the surface of the model is collected at points that are 1mm apart. However, since the detectors on the actual fNIRS probe are set at greater distances, the resulting photon fluence information will not be analysed at every existing point but will be taken for certain detector positions of interest only which will be called the "relative detector positions".

During the preliminary analysis for the testing of MCML and head model, the relative detector positions are assigned at 6 mm, 11 mm, 16 mm, 21 mm, 26 mm and 31 mm. Since beyond these SD pairs, as it is discussed in literature [10], no significant information provided therefore the signals from the rest of the detectors are not used for the analysis.

4.1.2 Optimisation of Number of Photon Packages and Simulation Runs

Accordingly, the first step in the MCML simulation studies was to achieve optimisation of the number of photons and also the number of runs of the simulations in order to obtain results with good coefficient of variation.

The simulations were performed for three sets of photon numbers, for ten individual runs. These numbers were selected to be; 10^5, 10^7, 10^8 photons, which are the commonly used values for the MCML simulations of the photon propagation in brain tissue studies.

Relevant detector positions calculations of standard deviation and coefficient of variance are given below, however the calculation is realised for all detector positions for purposes of future comparisons which might become handy for further assumptions.

Table 4.1
Coefficient of Variation for 10^5, 10^7, and 10^8 Photons for Selected Detector Positions.

Det Pos.	100K CV	10M CV	100M CV
6 mm	%2.1753	%0.1744	%0.0000
11 mm	%3.4086	%0.4491	%0.0000
16 mm	%9.5379	%0.4914	%0.0000
21 mm	%11.2612	%2.1722	%0.0000
26 mm	%30.4628	%4.0924	%0.0000
31 mm	%56.6014	%4.0025	%0.0000
36 mm	%37.5969	%7.3582	%0.0000
41 mm	%99.6809	%9.7219	%0.0000
46 mm	%84.4357	%14.8124	% 0.0000

It can be seen from the table of the results that although the simulations using 10^8 number of photons show the smallest (zero to an insignificant digit) coefficient of variation values, the time it takes for one run of 10^8 number of photons is almost ten times longer that what it takes for one run of simulation time of 10^7 photons. (780 sec = 0.22 hr. Simulation time of one run for 10^7 photons and 10513 sec = 2.92 hr. Simulation time of one run for 10^8 photons. See Appendix 10M output and 100M output) However, when the simulations are performed with 10^7 number of photons at each run for a total of ten individual runs, the coefficient of variation are within a tolerable range for detector position that are used for analyses. This finding agrees with the study conducted by Haeussinger *et. al.* where it was presented that the normalised absorption overlap comparing 5x10^6 and 10^7 photons found to be greater than 99.8% [10].

4.2 Inhomogeniety Analysis

4.2.1 fMRI BOLD Data Interpretation

The simulated data by the implementation fMRI BOLD data for one channel from one subject shown in figure 3.2 and quantified in table 3.2 is compared with the real fNIRS measurement where the BOLD data collected over four blocks are averaged.

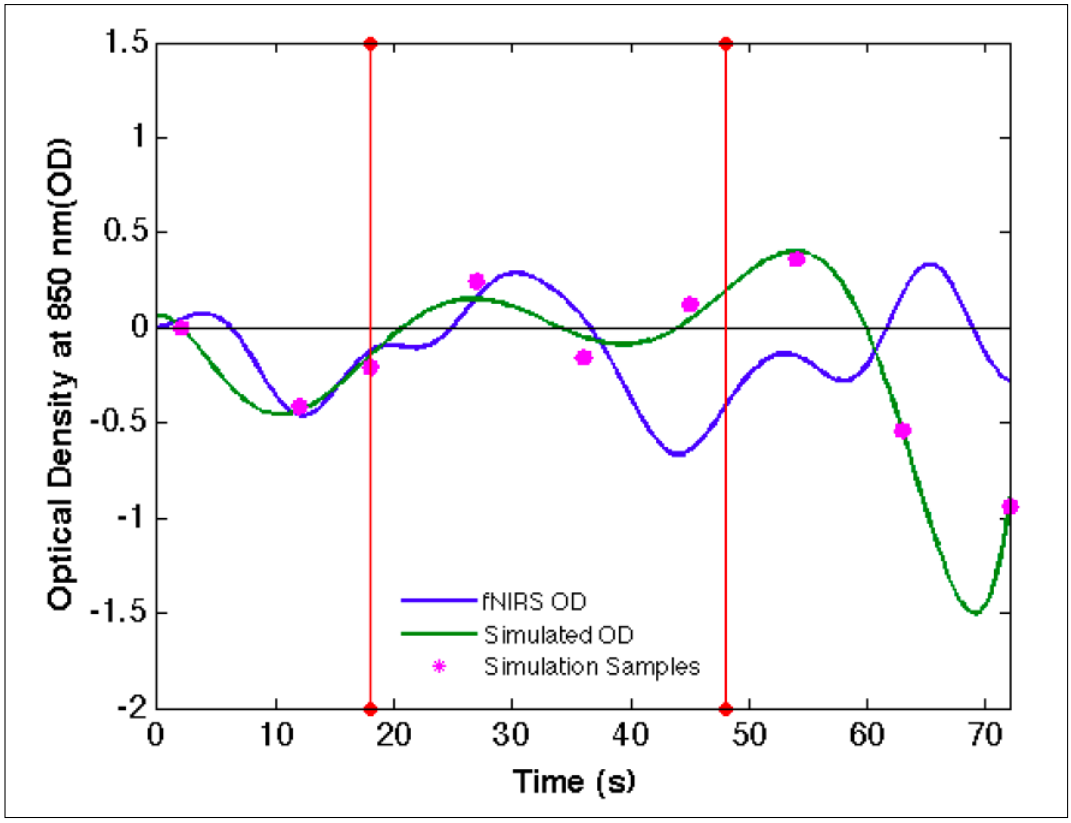

Figure 4.1 Simulated OD and Real OD from fNIRS.

In Figure 4.1 a 6th order polynomial is fit to the simulation data points and compared with the actual optical density values of the realtime fNIRS measurement results. The data points coincide numerous times with the fNIRS OD curve until the end of the breath hold task and the two curves show the same trend for the optical density. The similarity between the two curves indicate that the approach shows a great promise to test the validity of fNIRS measurements. By increasing the number of simulation samples, and the number of subjects a further investigation seems worth trying.

4.3 Near-Far Detector Analysis

Two sets of computations were carried out for the determination of a near and a far detector arrangement, on data sets of;

1. Simulation of the Arbitrarily Assigned Changes in MCML
2. Simulation of the fMRI BOLD Data Changes Only in the GM Layer
3. Simulation of the fMRI BOLD Data Changes in both GM and Scalp Layers
4. Simulation of the Thin Skull Model Absorption Changes

respectively.

For all data sets mentions, two sorts of comparison methods were used. Firstly, a separate relative intensity curve plot is constructed by dividing each intensity curve (I) an assigned change is divide by the baseline intensity (I_{base}) curve which is called "Relative Intensities". Secondly a curve plot which shows the absolute value of relative intensity differences between detection points is represented by "Differentiation of the Relative Intensities".

Although all detection points are plotted and given, it can be clearly seen from the graphs that near-far detector analysis the plot of detection point up to 30mm is more than sufficient.

4.3.1 Simulation of the Arbitrarily Assigned Changes in MCML

4.3.1.1 Relative Intensities

Below in figure 4.2, nine curves are constructed which represent the percentage μ_a changes implemented in gray matter on the same head model. The baseline for this figure (I_{base}) is the curve of the simulation where the scattering and absorption coefficients are of a resting state of the brain, and the other curves are the simulation results with changes of the absorption coefficients. These changes start from a 20% decrease and continue with increments of 5% up to a 20% increase. The baseline (I_{base}) simulation in this graph is represented as Time Label 1 and the rest of the time labels increase with the increasing μ_a percentage change, i. e., Time Label 2 corresponds to -20% and Time Label 9 corresponds to +20% change in μ_a.

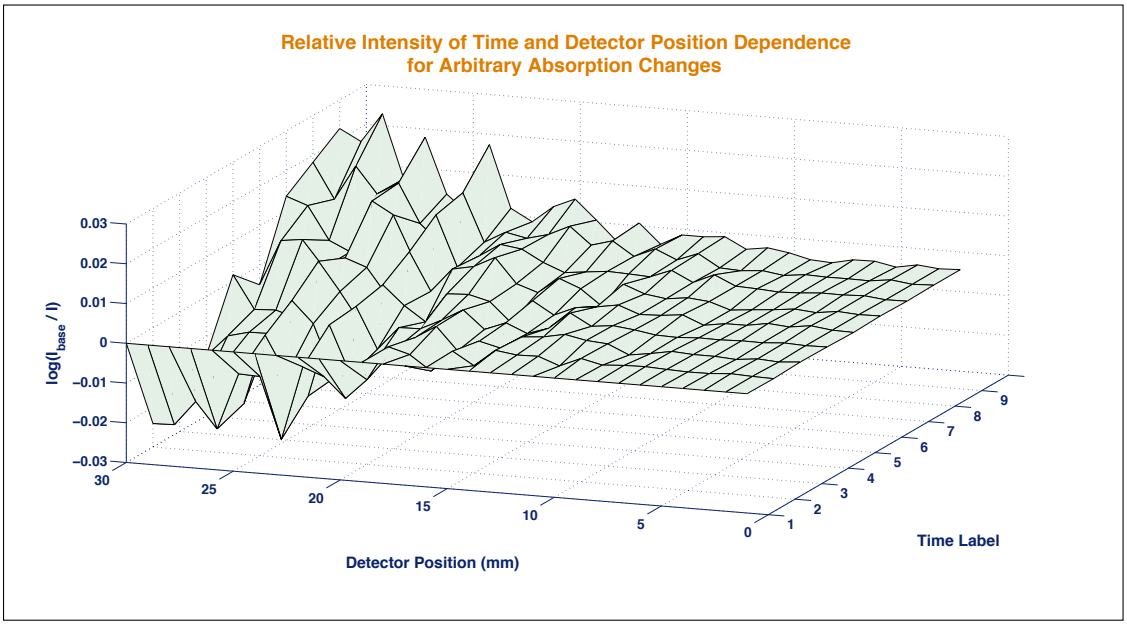

Figure 4.2 Arbitrarily Assigned Changes MCML Detector Positions 1 - 30 mm.

In the figure it can be clearly observed that as the Time Label increase there is a logarithmic increase in the relative intensities which agrees with the basic assumption that as the absorption increase in the gray matter, the optical density will also increase logarithmically as formalised in equation 2.1.

Visually, one can observe the peaks forming at positions 15 - 20 mm where the near detector position is expected to lie, yet there are indifferent peaks above the detector position 20 mm and this requires for a more detailed investigation.

4.3.1.2 Differentiation of the Relative Intensities

Since the analysis shown in graph 4.2 is inadequate to precisely position the near-far detectors which would indicate that the photon path distribution has moved to another layer, the derivative of the previous intensity results is taken in order to acquire an information on how much the intensity changes with respect to the previous detector position. This analysis gives way to perceiving the earlier main peaks with the shadowing of the peaks through the end of the detector position at 30 mm, n addition, this analysis also shows which peaks after the 20 mm show real jump from the adjacent detector positions.

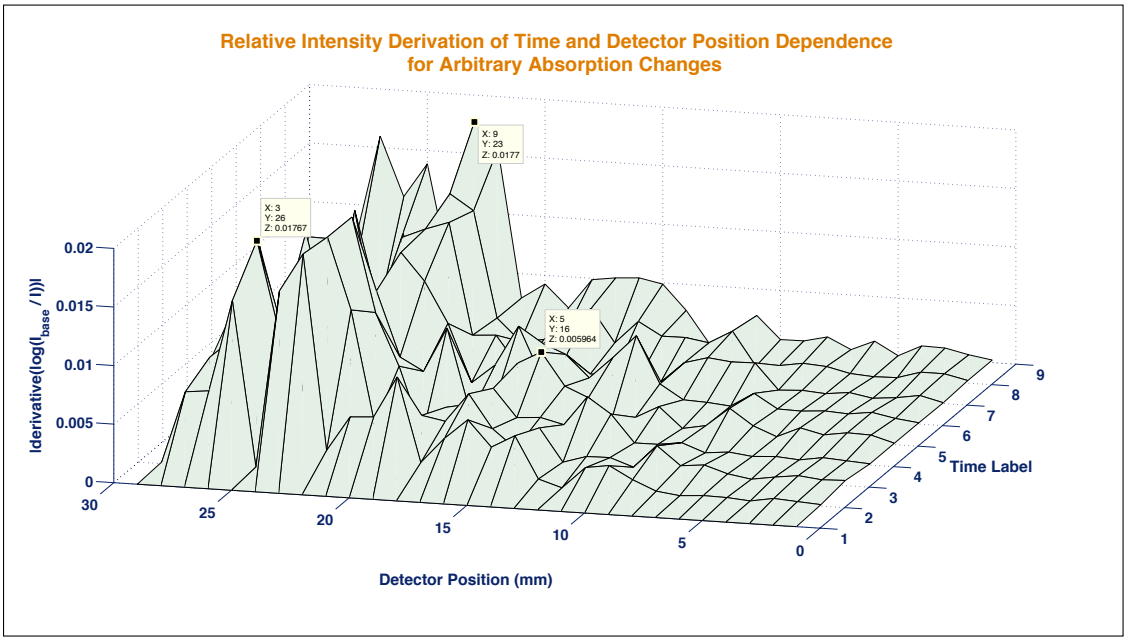

Figure 4.3 Arbitrarily Assigned Changes MCML Detector Positions 1 - 30 mm.

As labelled in graph 4.3, the abrupt peaks indicate a photon distribution entering a media with a different absorption coefficient. Although an increase or decrease of 20% in the absorption coefficient may be observed in muscle oxygenation, it is non-realistic

to expect such changes is the gray matter during a cognitive task. This analysis shows a broad understanding of the near-far detector positions, however a more accurate approach is required.

4.3.2 Simulation of the fMRI BOLD Data Changes Only in the GM Layer

In order to provide a realistic time dependent approach, starting from this section the simulations are carried out with percentage μ_a changes that represent a more accurate approach; by the implementation of fMRI BOLD data percentage changes as explained in detail in section . By taking one step further in order to be able to compare the result from the previous section where only GM layer absorbance was altered, in this section also only GM will be subjected to changes but this time with much smaller amounts.

In this part of the analysis, time labels correspond to the percentage changes quantified in table 3.2 where there is not a stable increase but rather a fluctuation in μ_a percentage changes.

As of this section, the baseline curve for the analysis of intensities will be chosen to be Time Label 2 which corresponds to the data set taken right before the breath hold test has begun. The rest of the time labels are again indicated in table 3.2 obtained from the fMRI data acquisition.

4.3.2.1 Relative Intensities

In this part of the analysis, even in the relative intensity graph 4.4 the near- far detector positions begin to appear around positions at 18 and 27 mm. The relative intensity values in this graph is much lower (one third's) than the values obtained from simulations of a much higher absorption changes. This is quite expected since the real percentage changes correspond to values around 1%, whereas in the analysis arbitrary changes were assigned not only the values much higher but also those values had great differences amongst each other.

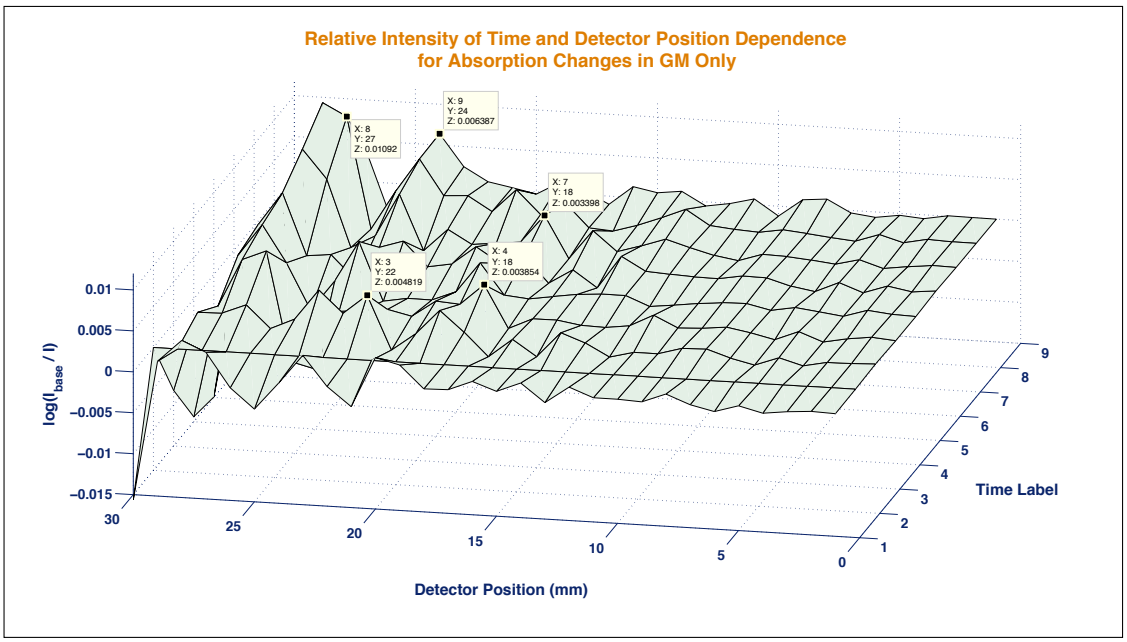

Figure 4.4 Relative Photon intensities of the GM Layer μ_a Changes.

4.3.2.2 Differentiation of the Relative Intensities

When the derivative of the changes between the detector positions are taken, and plotted in figure 4.5, peaks around 17 mm and between 23-26 mm become more observable.

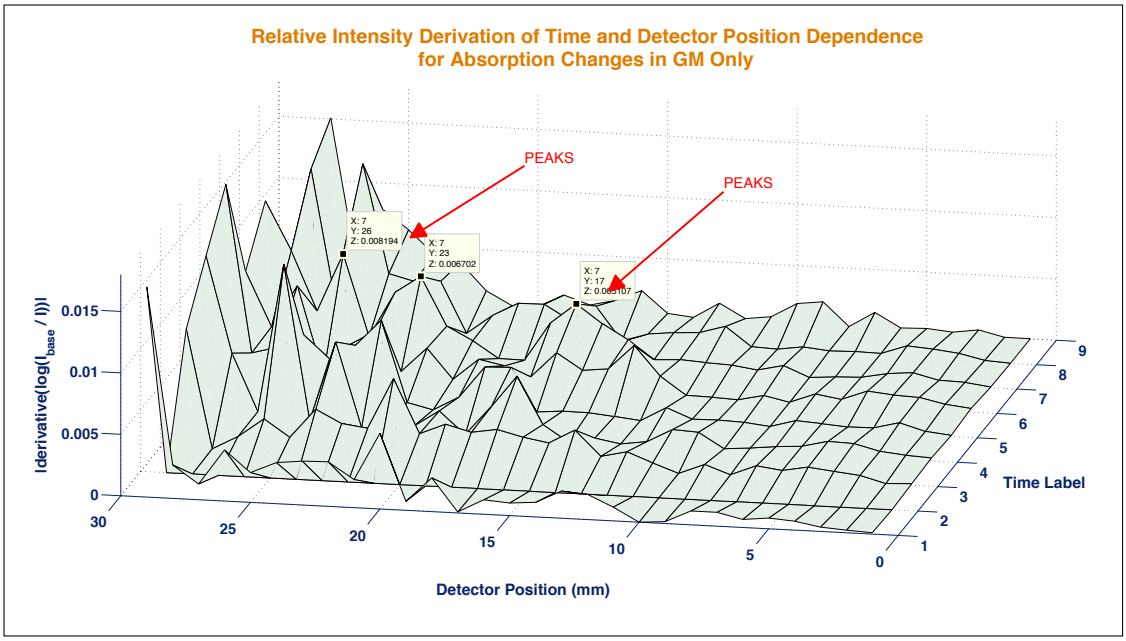

Figure 4.5 Differentiation Photon intensities of the GM Layer μ_a Changes.

4.3.3 Simulation of the fMRI BOLD Data Changes in both GM and Scalp Layers

Although in the previous subsection, μ_a changes are used only for the gray matter layer, due to systemic fluctuations, there is also a change in the μ_a of the scalp layer. And in this section, the results where changes in the absorption in both layers (scalp and gray matter) is presented.

4.3.3.1 Relative Intensities

In this part of the analysis, when the intensity curves are compared, a picture where there are a lot of fluctuations in the peaks are observed. Not only one can see many peaks around where the near and far detectors are supposed to be, there are also new peaks appearing in graph4.6 compared to the graph in figure 4.4 where the scalp μ_a is left unchanged. Therefor these fluctuations are normally expected since the scalp μ_a changes bring a different set of dynamics inside the picture.

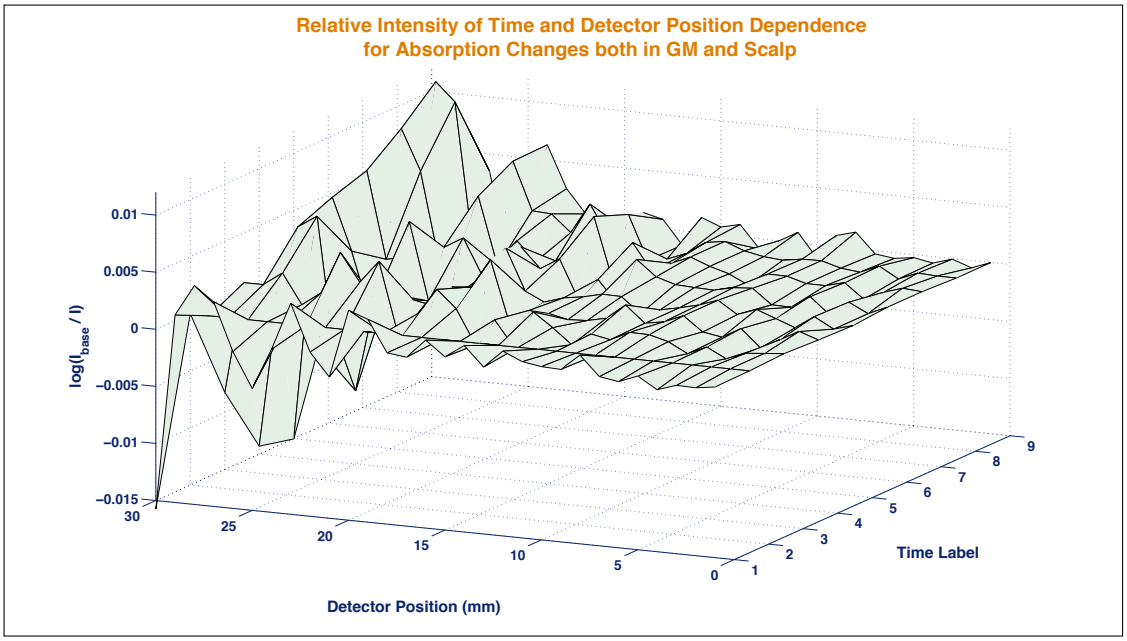

Figure 4.6 Relative Photon intensities of the GM and Scalp Layers μ_a Changes.

4.3.3.2 Differentiation of the Relative Intensities

When the differentiation analysis is applied to fMRI BOLD changes for both scalp and GM layer, a more explicit set of peak appear. For almost all time labels, a discrete jump at around 14-15-17 mm and a second cluster of peaks become visible around 25-26-27 mm. And also there seems to be tiny but observable changes around 5 mm, which is though to be related to the scalp μ_a changes.

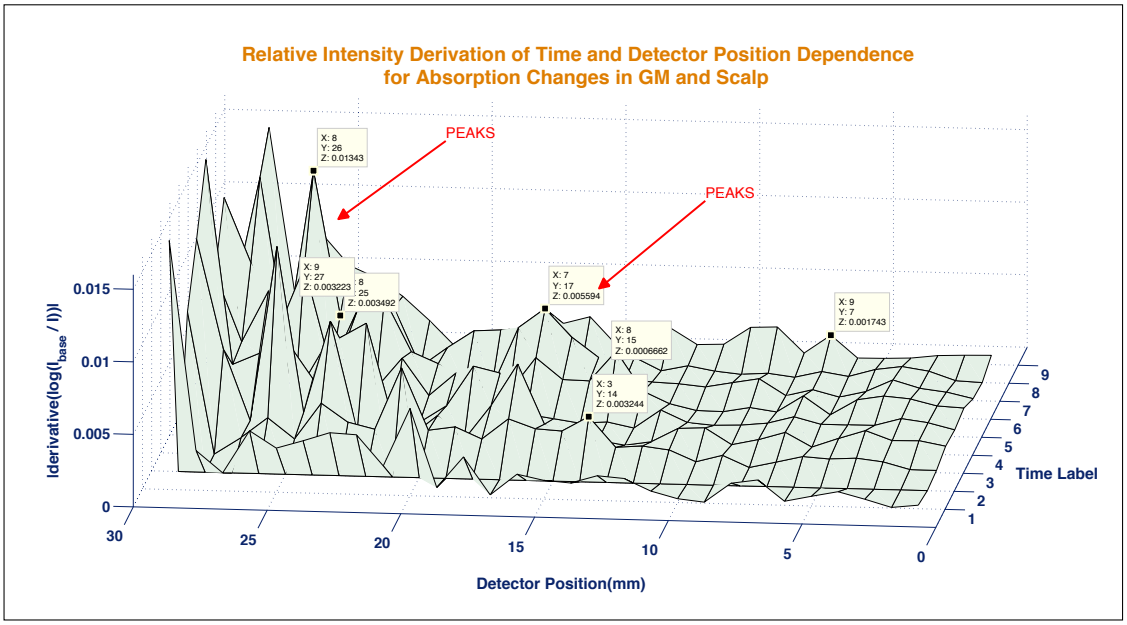

Figure 4.7 Differentiation Photon intensities of the GM and Scalp Layers μ_a Changes.

4.3.4 Simulation of the Thin Skull Model Absorption Changes

The previous graphs shown in figures 4.7, 4.5 and 4.4, points to an existence of a near detector, where the photons reaching that detector contains information on the scalp, skull and CSF layers- previously described as superficial layers, and a far detector where the information carried is extended to the gray matter. However, although this conclusions seem reasonable, there is way to reinforce this statement and it again goes through the idea that as the GM layer moves closer to the surface where the light enters the medium, the near-far detector positions must shift toward the source (a decrease SD pair distance) relying on the theory of the "banana-shape" photon distribution.

In the next two figures, a representation of a model with a thinner skull (4 mm instead of 7 mm) is supplied which implies a GM layer starting from a 3 mm distance above as explained in detail during the method part of the study. However, in order to prevent any misunderstanding, this is a good loin to repeat that the thickness of GM layer remained unchanged, merely the whole layer is moved towards the surface of the head model.

4.3.4.1 Relative Intensities

As expected, the relative intensity analysis does not give an adequate information on whether the near-far detector positions are shifted, although it does give some clue about where the peaks begin to show themselves.

Figure 4.8 Relative Photon intensities with a Head Model Mimicking Thin Skull.

4.3.4.2 Differentiation of the Relative Intensities

The following figure 4.9 can be seen a great indicator that the previously observed peaks in the regular head model belonged to near-far detectors since the very similar peak clusters seen in figure 4.7, now show themselves around detector positions around 11-12 and then at 17 mm as expected.

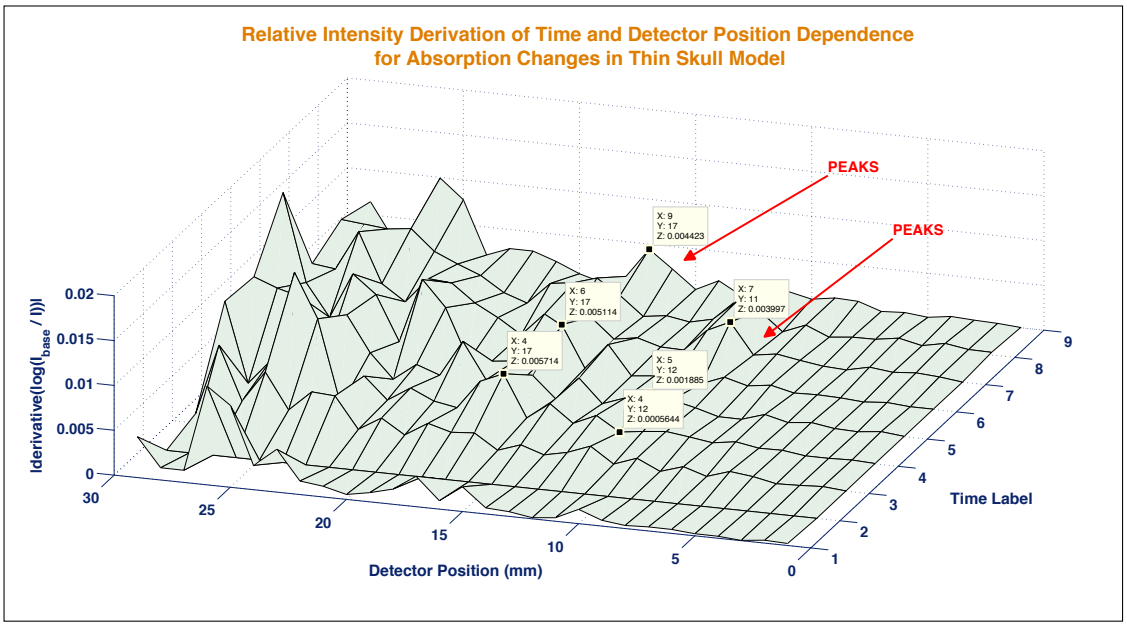

Figure 4.9 Differentiation Photon intensities with a Head Model Mimicking Thin Skull.

This part of the analysis therefore provides a good proof that the peaks emerge where there is a change between two layers of different absorption coefficients.

4.4 Detector Clusters

Although in the previous analyses the indications that the near and far detectors are assigned, there is still a point which requires more attention namely the the detectors themselves. As explained in much detail in section 3.3.2, an approach called as clustering is proposed. This clustering approach enables one to analyse a more realistic approach for the detector intensities since from now one, the detectors contain a wider range of data as in a real fNIRS probe detector, and also the moving average of the detector clusters is expected to provide information on where the real differences takes place.

4.4.1 Absorption Change in Gray Matter

When arbitrary μ_a changes was inserted inside the simulations, their cluster information contains high amount of absorption changes therefore lacks a clear representation of the near-far detector position, still there are some visible peaks in the slopes of cluster 17 in figure 4.10.

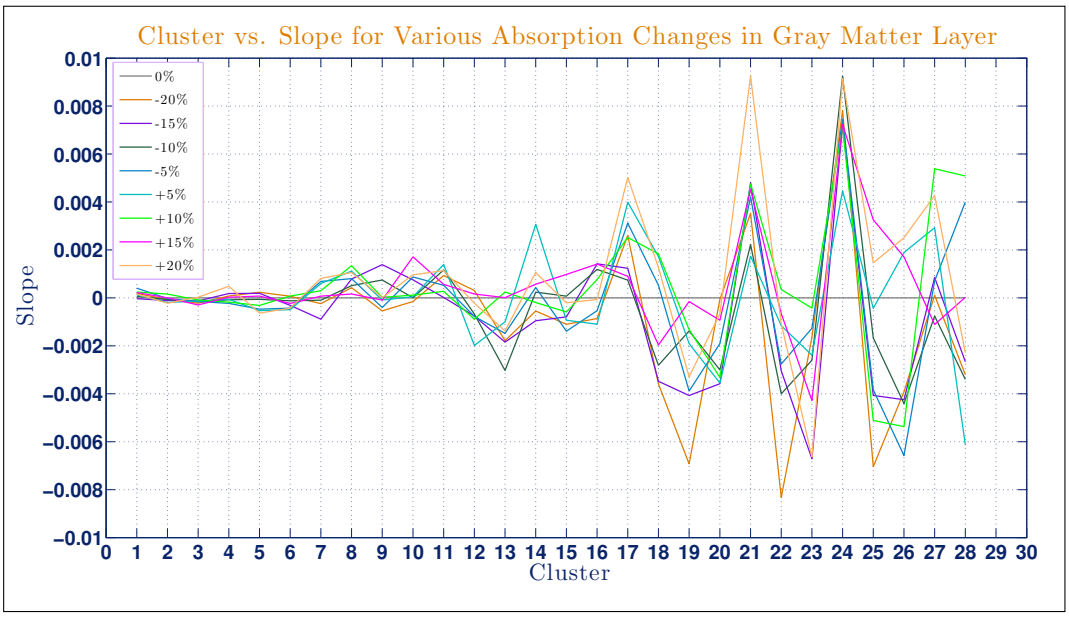

Figure 4.10 Slope Values for Arbitrary Absorption Changes.

4.4.2 Absorption Changes Only in Gray Matter

The slope calculations for fMRI BOLD implemented μ_a changes represented in figure , the peaks for all time labels show a similar trend and around clusters 17, 22 and 26 reveal significant peaks that point to the positioning of near-far detectors.

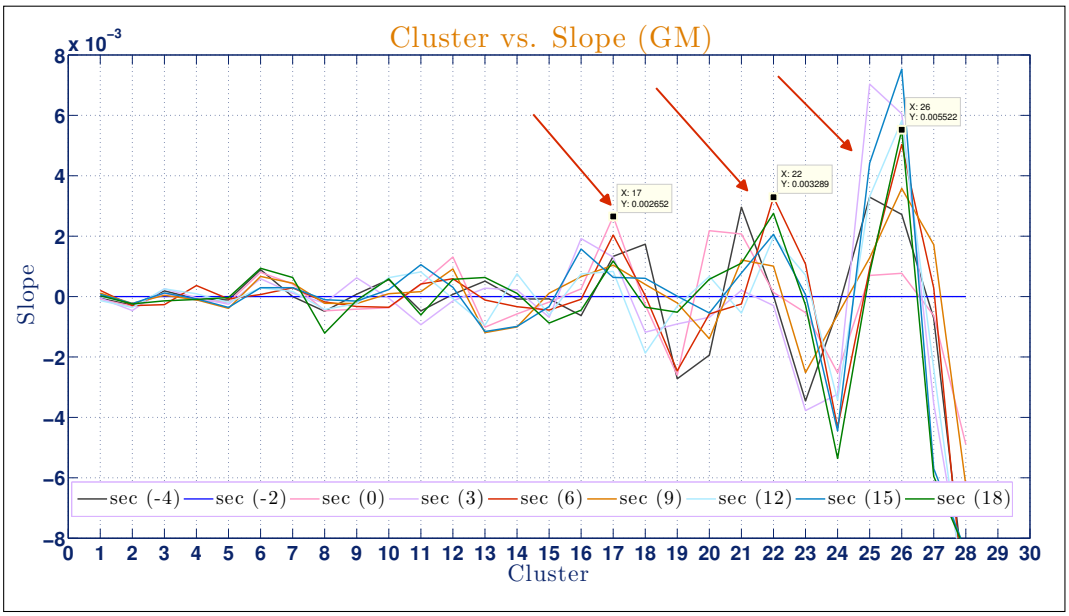

Figure 4.11 Slope Values for Measured Intensity Corresponding to Gray Matter Absorption Changes.

4.4.3 Absorption Changes in Scalp and Gray Matter

The main difference between this analysis and the analysis of the slopes corresponding to GM μ_a changes is that, one must also be able to see the fluctuations due to the scalp layer as well as the GM layer.

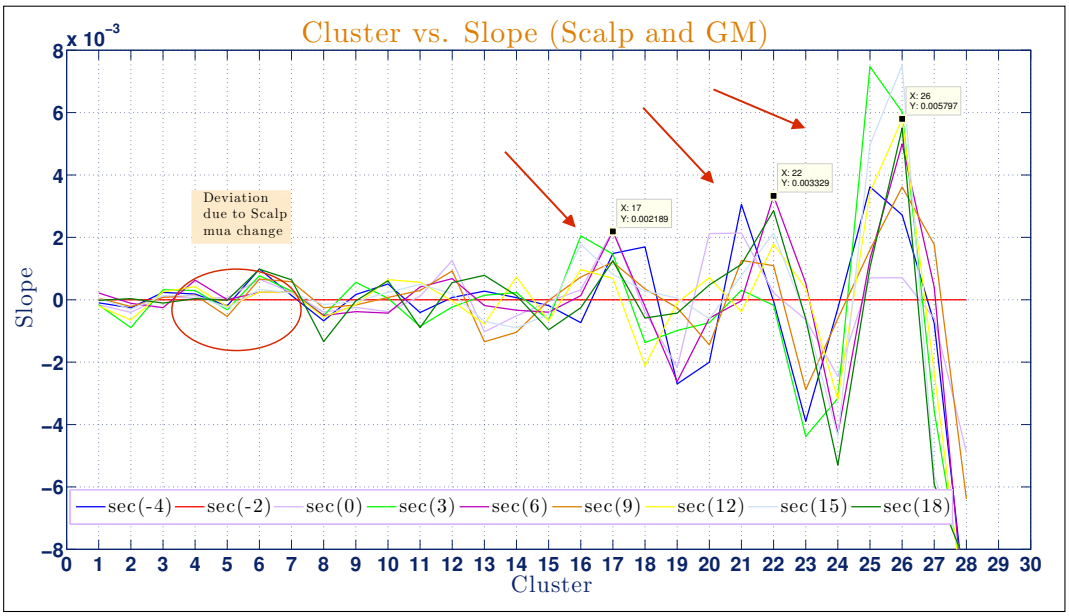

Figure 4.12 Slope Values for Measured Intensities Corresponding to Gray Matter and Scalp Absorption Changes.

The peaks at detector clusters in figures 4.4.5.1 are in good agreement in the peak positions of figure 4.11 except for some other visible peaks encircled in red which are thought to belong to the scalp μ_a changes.

4.4.3.1 Absorption Changes in Scalp and Gray Matter, Emphasized

In the following figure, in order to emphasise the differences in slope peaks, the values of the previous analysis is squared leading to a much more explicitly.

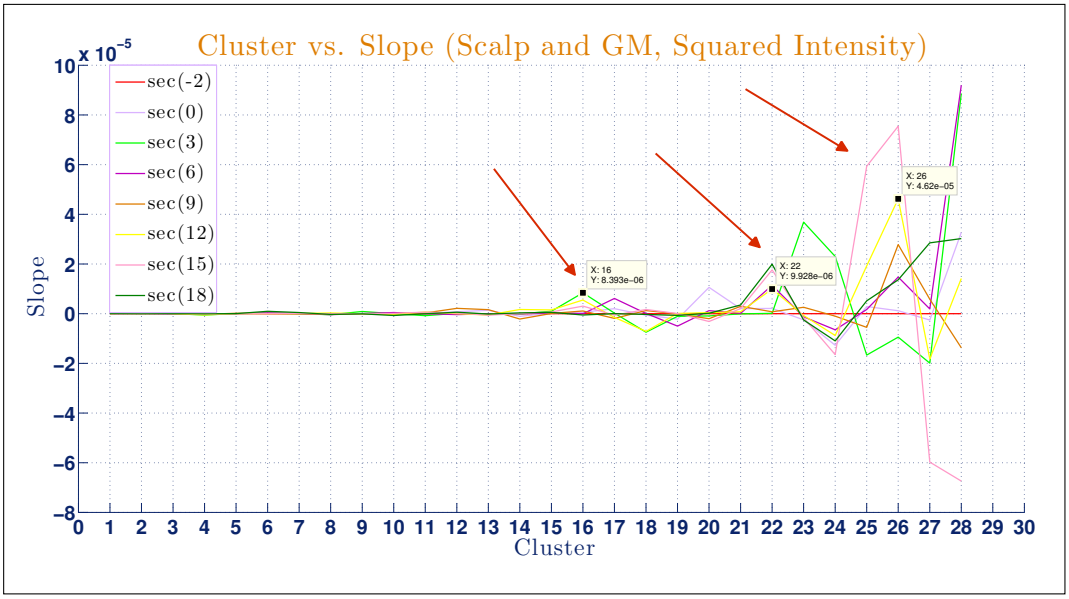

Figure 4.13 Slope Values Corresponding to Squares of The Relative Intensity Values.

4.4.4 Validation of the Method for Near-Far Detector Assignment

The slope values of the thin skull model of the head is also calculated in order present the shifts in clusters with a greater accuracy. It can clearly be seen from figure 4.14 that the new peaks appear at clusters 10 and 16, where in figure 4.4.5.1 those corresponding peaks belonged to detector clusters 17 and 22. Therefore it can be stated with confidence that these clusters are where one should position the near-far detectors however this illuminating approach reveals a much bigger problem that the skull thickness has great influence on where these detectors should be assigned at. Which means, in order to be able to assign near-far detectors, one should have an estimate of the skull thickness of the head.

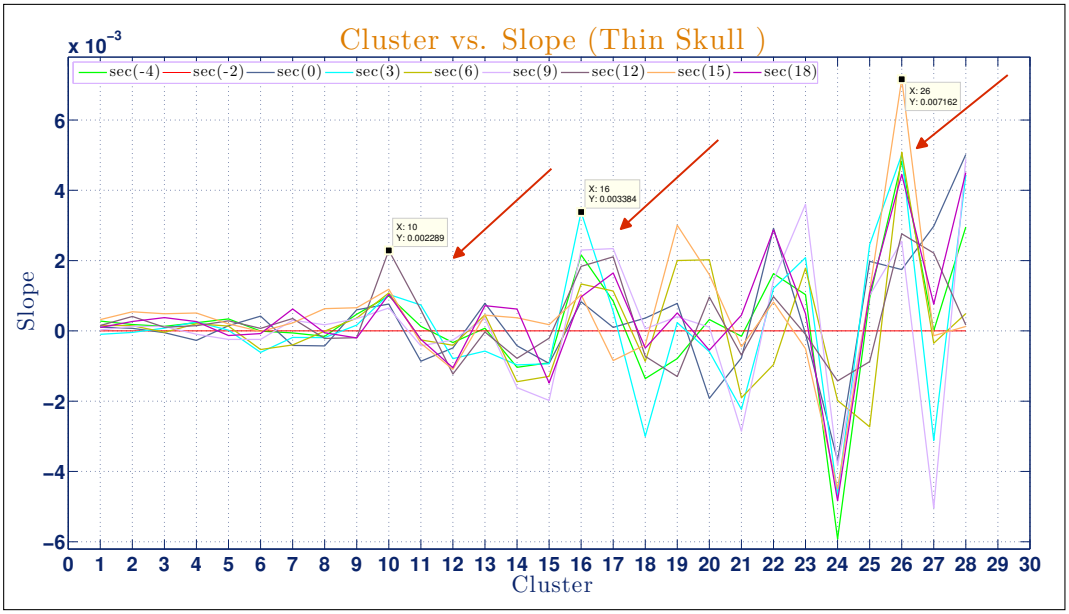

Figure 4.14 Slope Values for a Reduced Skull Thickness.

4.4.5 Time Based Comparisons of Slopes between Different Data Sets

4.4.5.1 Comparing the Simulation with μ_a Changes for Only in GM and both in Scalp and GM

Qualitatively, from skimming through figures 4.11 and , there seems to be a differentiation between slope calculations of the head model simulations where a change

of μ_a only in GM and both in scalp and GM layer were implemented. This difference between the values of the slopes is further investigated by a time label based analysis where these two sets of data was compared for each time labels individually. Two of these comparison graphs are shown below, and the rest of the figures can be found in appendix.

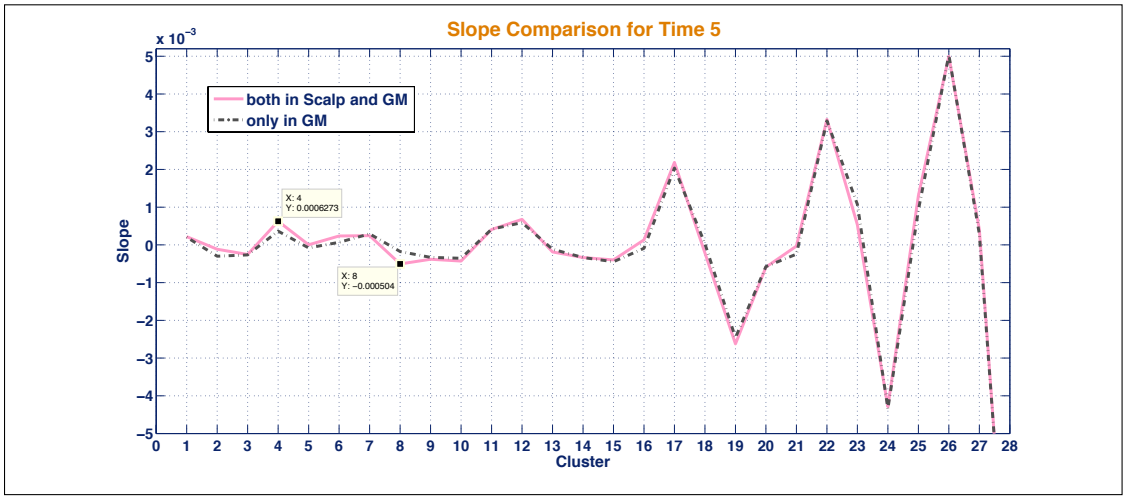

Figure 4.15 Slope Comparisons at Time 5.

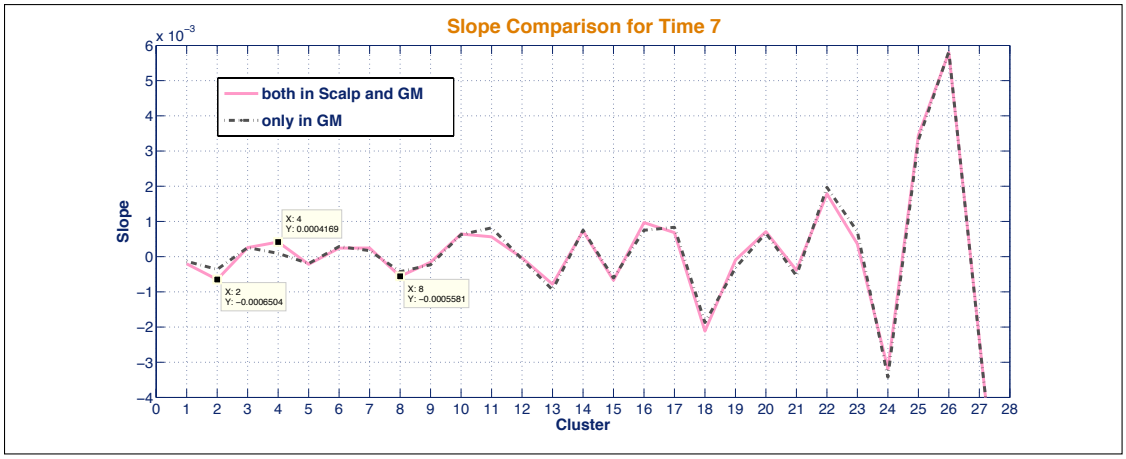

Figure 4.16 Slope Comparisons at Time 7.

When presented on the individual time based graphs, indeed there is a perceptible differences around detector clusters 2, 4 and 8.

4.4.5.2 Comparing the Simulation with the Basic Head Model and the Model with Thinner Skull Layer

Figure 4.14 shows a clear shift between the values of the slope peaks for the basic model where the skull thickness is taken as 7 mm, and a thinner skull layer (4 mm) model. The near-far detector positions move closer to the source for a thinner skull layer model since this model represents a GM layer closer to the surface where probe is placed. Instead of viewing slope values for all time labels, the data sets again is compared based on the time labels in order to provide a quantitative understanding of this detector position shift. The comparison between two models, namely; the basic model and thin skull model, is shown below for selected time 3, whereas the rest of the comparisons are provided in Appendix.

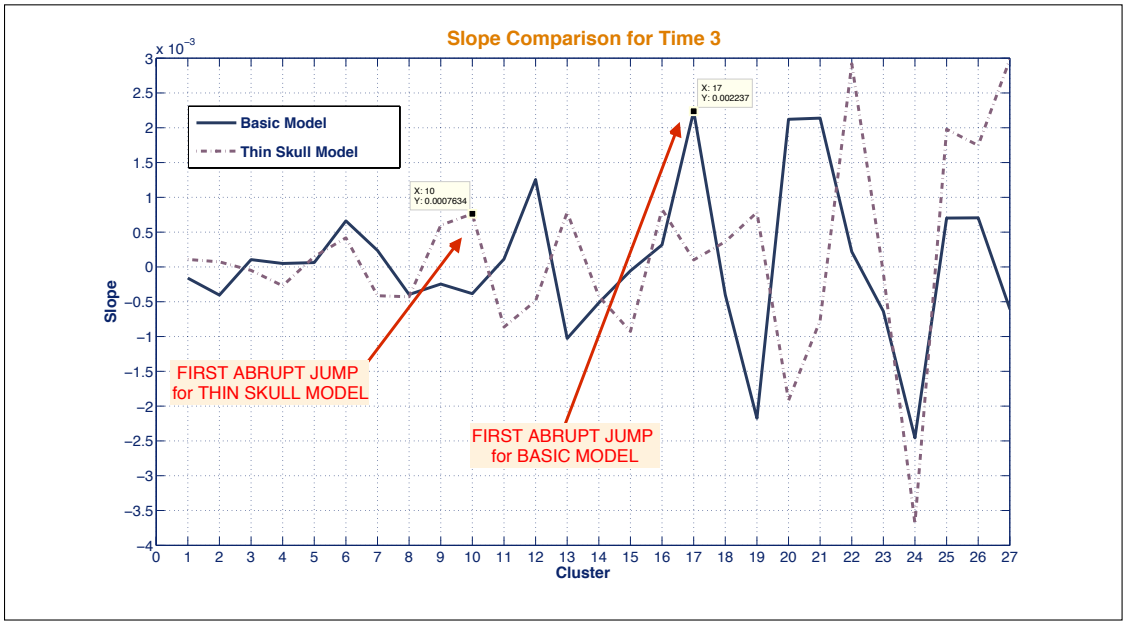

Figure 4.17 Slope Comparisons at Time 3.

From the graph shown in figure 5, the first abrupt jumps in slope values are indicated. The first abrupt jump in the peak values (almost doubled in size) is seen at 10 mm for the thin skull model, whereas the abrupt jump for the basic model remains at position 17 mm.

5. CONCLUSION and FUTURE DIRECTIONS

In order to describe a realistic model, firstly the monte carlo method was used for simple geometries for the testing of a good photon propagation model in multi layer tissue. After obtaining the banana shape behaviour of the photon diffusion, a more complicated model was introduced to the simulations. The model was constructed by a thorough research on optical parameters of superficial and brain tissue which is the key to a realistic approach.

Arbitrary assignment of blood oxygenation changes as increments of 5% ranging from -20% to 20% given as a simulation input for MCML is seen to be much larger than the measured changes in the fMRI BOLD signal which has a value of maximum 2% for the breath hold task [4]. However, it can be seen from Fig. 4.10, that the clusters 17, 21, 24 corresponding to detector positions 17-18-19 mm, 21-22-23 mm and 24-25-26 mm, show a similar trend to that of slope of simulated fMRI Gray Matter data shown in Fig. 4.11, only of course as the percentage changes increase up to 20% a maximum slope value of about $4x10^{-3}$, $9x10^{-3}$ and again $9x10^{-3}$ for clusters 17, 21 and 24 respectively, which are much larger than the slope values of simulated fMRI Gray Matter of $2x10^{-3}$, $3x10^{-3}$ and $6x10^{-3}$. It can be concluded that the method is still valid generally for most changes applied, however a precaution is required since as higher oxygenation changes are implemented the slope analysis may overestimate the actual changes inside the gray matter.

As a part of this thesis, a methodology for translation of oxygenation changes both inside the scalp (a part of superficial layer) and the brain, where the real brain activity information is hidden, to the actual optical density changes obtained from real fNIRS data is presented. The changes in the haemodynamics of the brain activation was modelled by using an approach that combines fNIRS and fMRI techniques in which the changes in blood oxygen level dependent (BOLD) signal from the activated regions of the brain was assumed to have a linear dependence to the absorption coefficient

changes int the relative region. By using this approach the Monte Carlo method was transformed into a technique that reveals a time dependency of the the evoked brain activity.

For the purpose of validation of this approach, which makes use of fMRI BOLD data as an input for MCML simulations for fNIRS, a statistical significance must be achieved since currently for this thesis, only the fMRI simulated and real fNIRS data from one channel of one subject was compared. In other words, a wider range of the fMRI BOLD data should be simulated by increasing the number of both the subjects and the channels belonging to those subjects should be analysed. By achieving such analysis, a temporal evolution of the non-brain signal contamination during a cognitive task may be qualified.

Following the formulation shown in eqn. 3.2 that combines fMRI and fNIRS, the attenuation changes at each detector position were calculated. These attenuation changes were calculated by the selection of a baseline that is represented as I_{base}. Since the changes of both an increase and decrease imply a mere difference between the depth of banana shape path distributions, the absolute values of the intensity differentiation are presented. Although these analyses give a broad idea of where the near-far detectors lie, a further investigation was needed therefore realised.

Due to the fact that, the detectors used in fNIRS probes usually have the dimensions of 2.5x2.5mm^2, the probe model used for the MCML simulations were not similar in nature, and there is a probability that one can lose significant information held by the detectors. In order to overcome such inaccuracy, another approach called detector clustering is used. These clusters is shown to provide a more realistic solution to the problem of the near-far detector assignment.

The near-far detectors were assigned to the model of fNIRS probe by the investigation of abrupt slope changes in the formed detector clusters. And a validation of their positions were per formed by a differentiation in the head model where, the similar signal were shifted by caring out same simulation except for a GM layer which is closer

to the surface. In figure 4.13 in which the slope changes are emphasised by squaring the slope values, there is a significant change at clusters 16, 22, and 26, corresponding to 16-17-18 mm, 22-23-24 mm and 26-27-28 mm, yet when the thin skull model is investigated in figure 4.14, the values are seen to shifted to the detector clusters 10, 16, and 26. a clearer shift can be observed in figure . This can be seen as a good indicator of the depth sensitivity of the detectors, since when the GM layer was moved closer to the surface, the photon path distribution information is collected at detectors closer to the source which is well described and in agreement with the literature [16]. However this validity analysis causes another big problem to emerge which can be stated as; as the skull thickness changes the near-far detector positions significantly shifts since the path that the light travel changes as explained in more detail by Okada *et. al.* [5]. The skull thickness of humans shows a variation from 4 mm to 12 mm which indicated that without the exact knowledge of this parameter, one can not correctly assign a near-far detector positions.

The differences between the slope values of two data sets presented in figures 4.15 and 4.16 can be attributed to the higher absorption in the scalp and this gives evidence that these detector clusters are indeed sensitive to this layer.

In conclusion, we have presented an analytical method to determine the positions of near-far detectors in fNIRS imaging modality that can be reliably used to extract brain derived haemodynamic optical changes from the changes in the overlying extracerebellar tissues (i.e., skin, skull, pia matter). The validity of this technique was first verified by Monte Carlo based simulations and then simulations with real fMRI data followed by a clustering analysis of the detector signals.

APPENDIX A. Complete Analysis Figures

A.1 Time Dependent Near Far Detector Analysis Figures

A.1.1 Arbitrarily Assigned Changes: Near Far Detector Analysis Figures

A.1.1.1 Relative Intensities

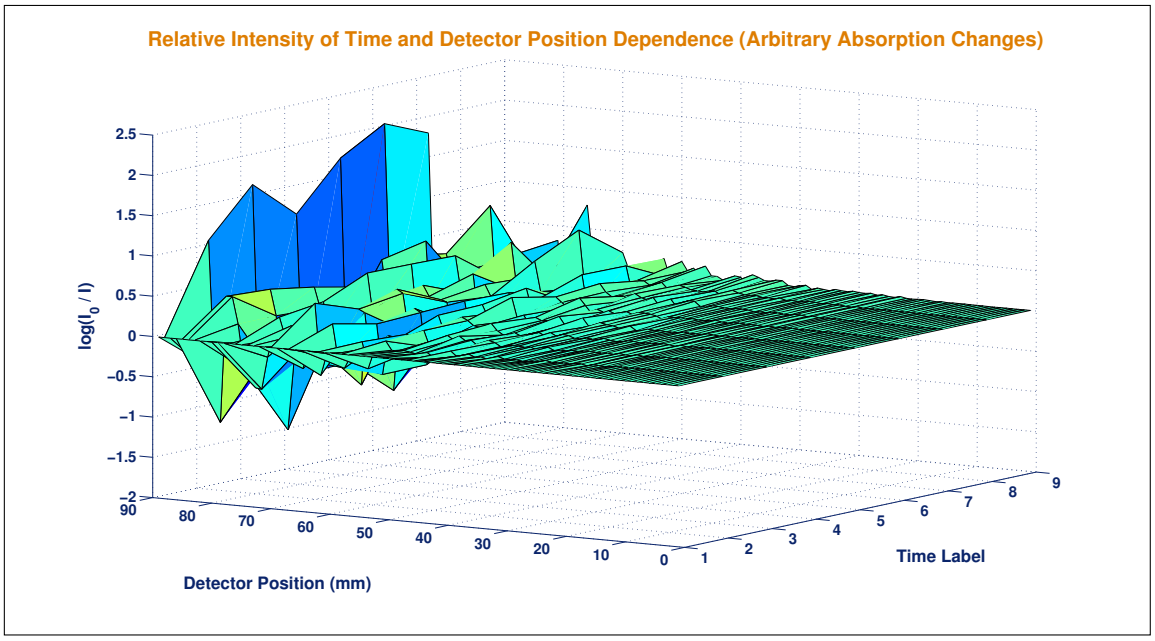

Figure A.1 Arbitrarily Assigned Changes in MCML.

A.1.1.2 Intensity Curves for each Time Label

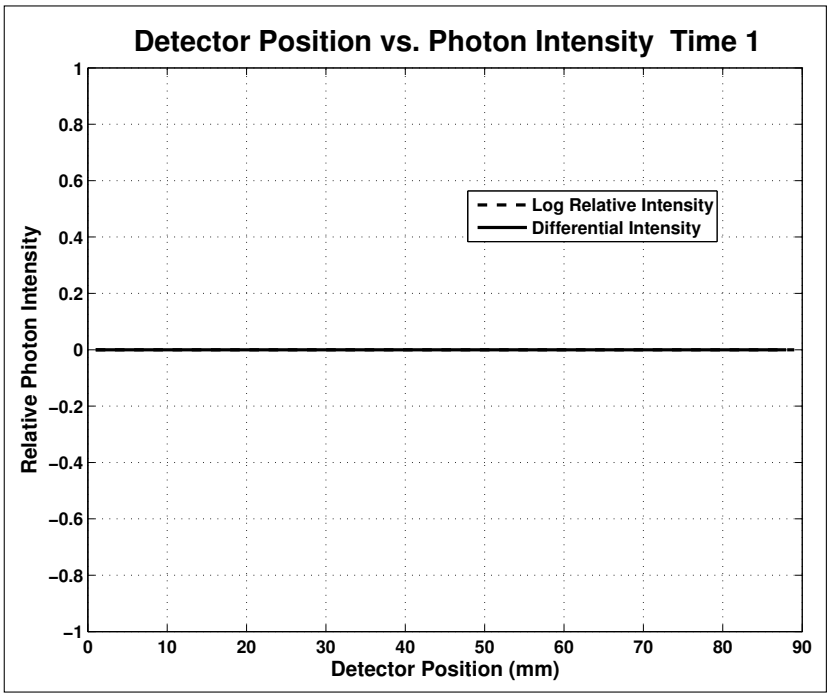

Figure A.2 Intensity Curves for Time 1, 1-100 mm, Arbitrary Changes.

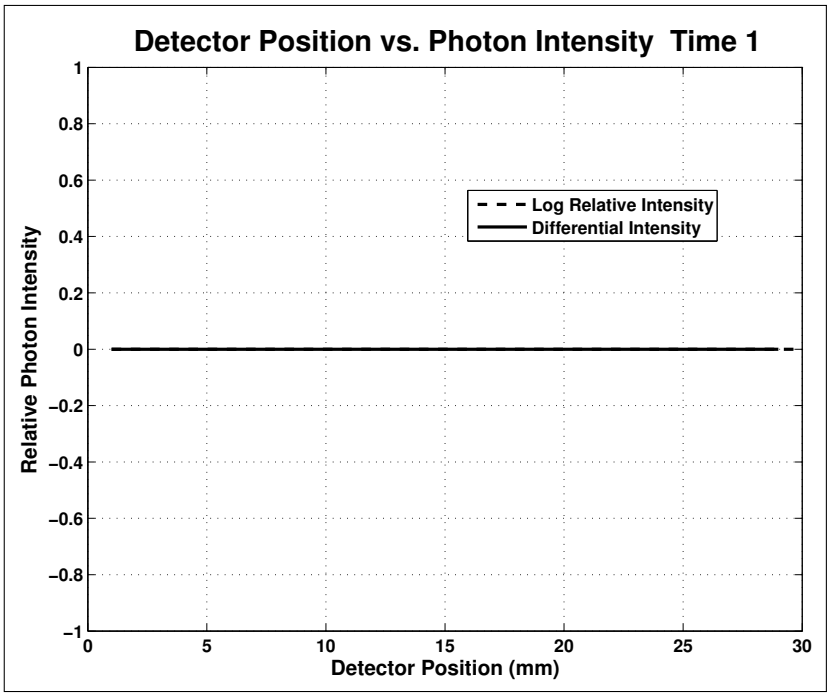

Figure A.3 Intensity Curves for Time 1, 1-30 mm, Arbitrary Changes.

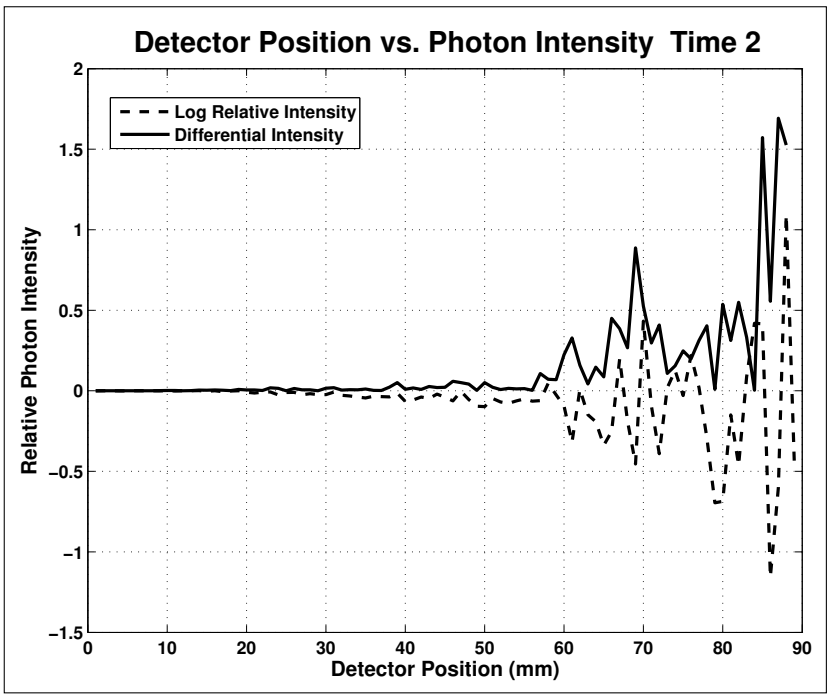

Figure A.4 Intensity Curves for Time 2, 1-100 mm, Arbitrary Changes.

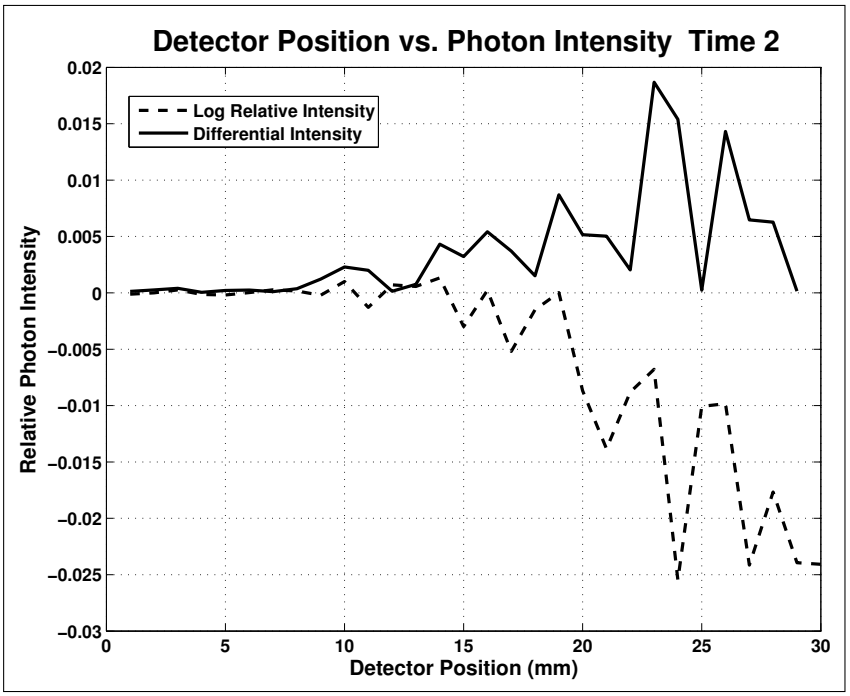

Figure A.5 Intensity Curves for Time 2, 1-30 mm, Arbitrary Changes.

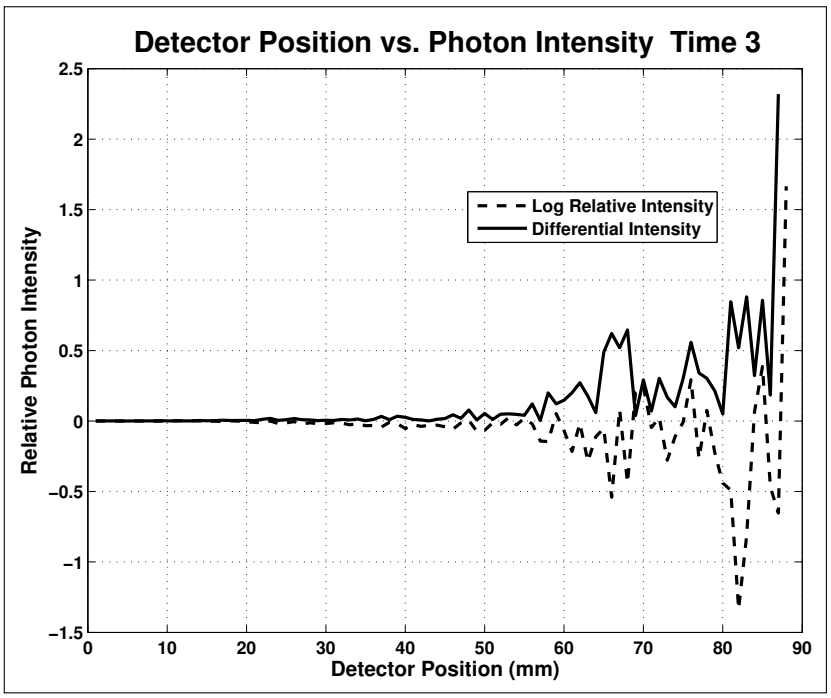

Figure A.6 Intensity Curves for Time 3, 1-100 mm, Arbitrary Changes.

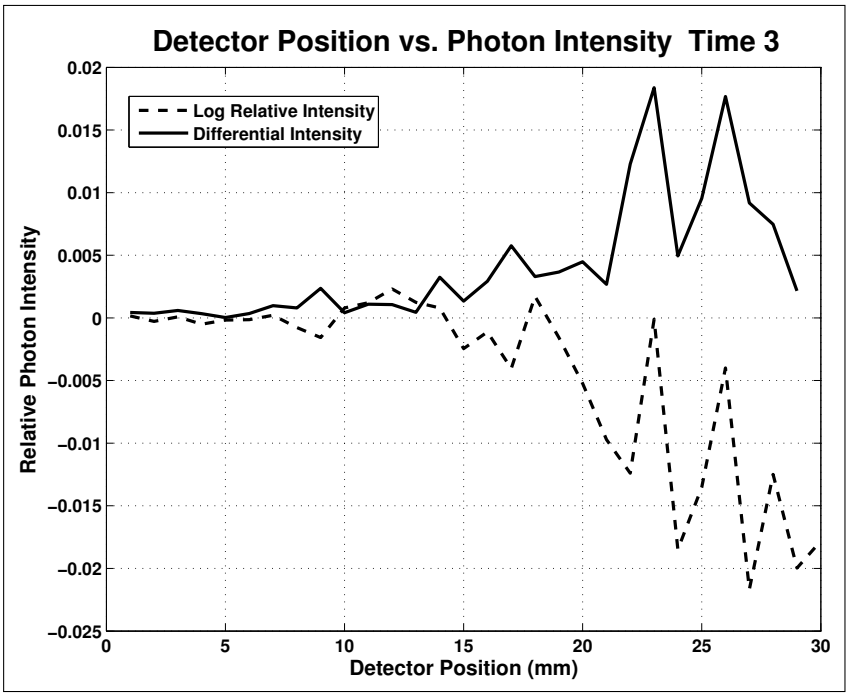

Figure A.7 Intensity Curves for Time 3, 1-30 mm, Arbitrary Changes.

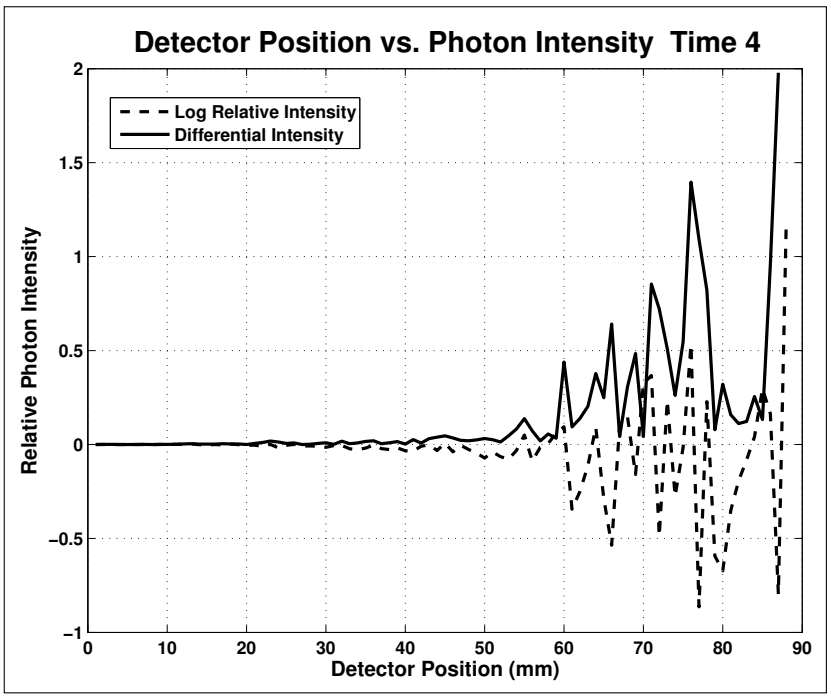

Figure A.8 Intensity Curves for Time 4, 1-100 mm, Arbitrary Changes.

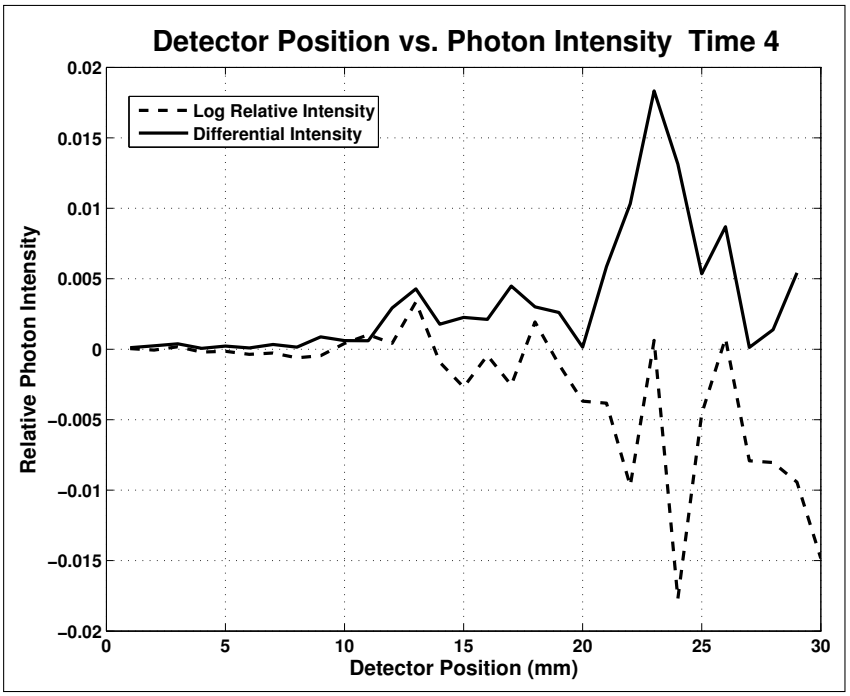

Figure A.9 Intensity Curves for Time 4, 1-30 mm, Arbitrary Changes.

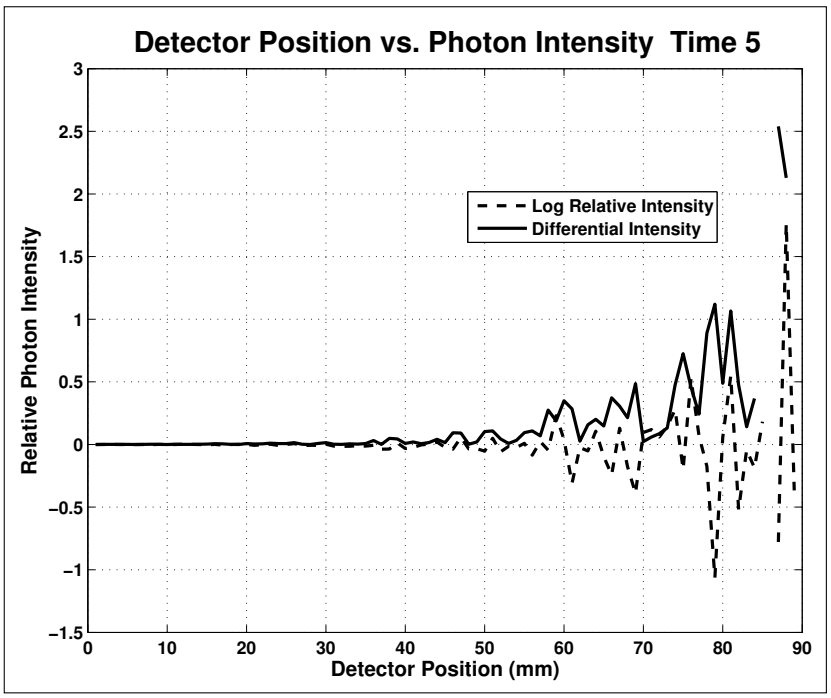

Figure A.10 Intensity Curves for Time 5, 1-100 mm, Arbitrary Changes.

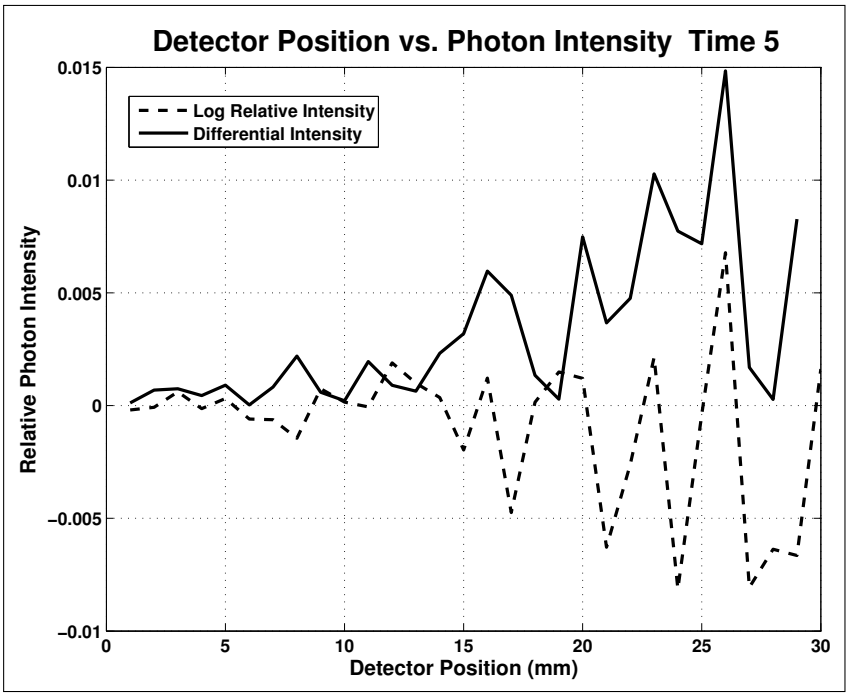

Figure A.11 Intensity Curves for Time 5, 1-30 mm, Arbitrary Changes.

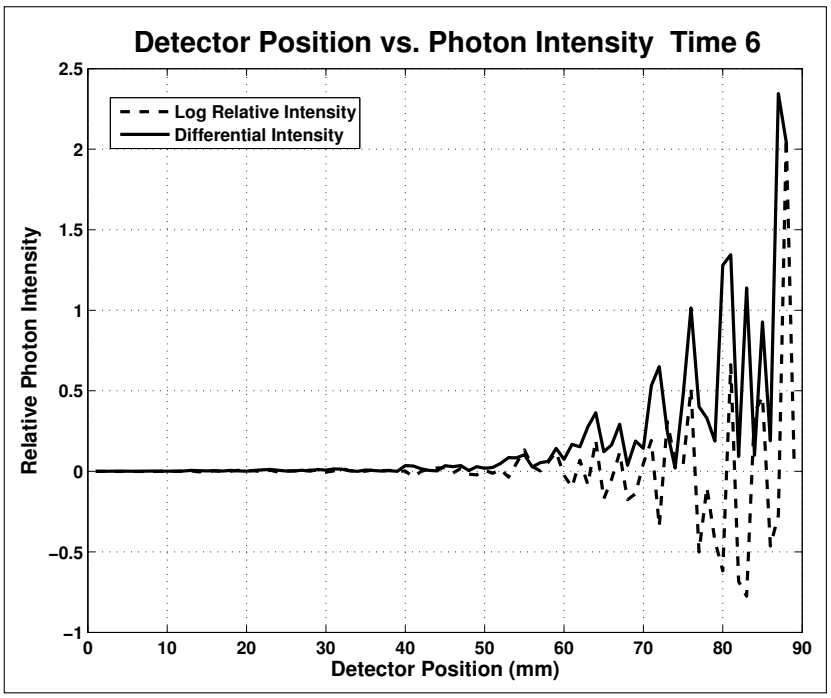

Figure A.12 Intensity Curves for Time 6, 1-100 mm, Arbitrary Changes.

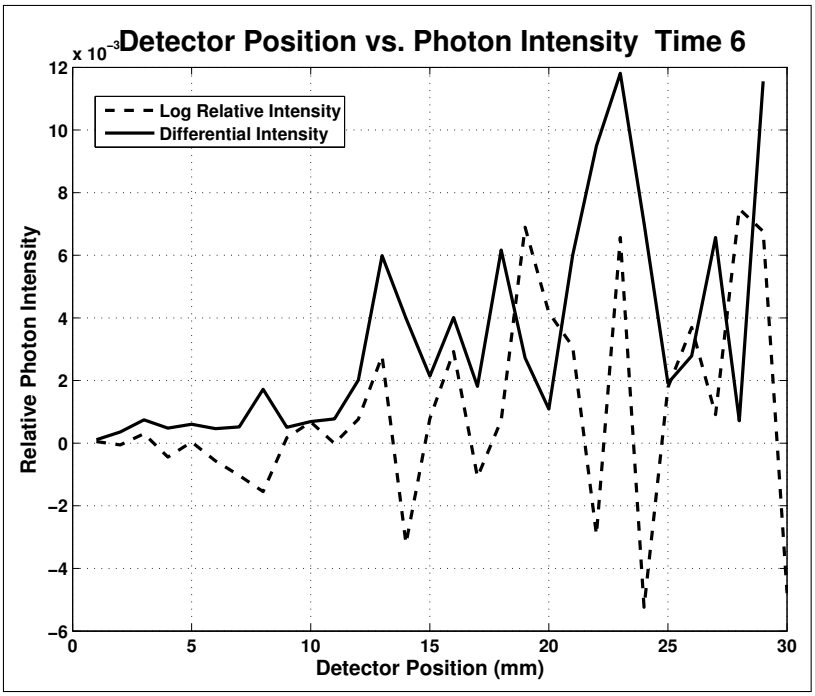

Figure A.13 Intensity Curves for Time 6, 1-30 mm, Arbitrary Changes.

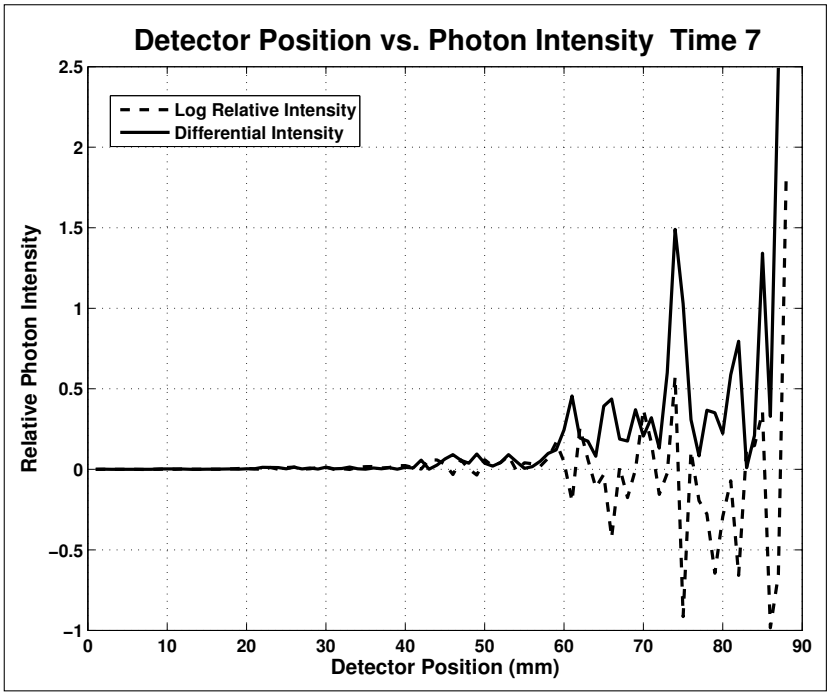

Figure A.14 Intensity Curves for Time 7, 1-100 mm, Arbitrary Changes.

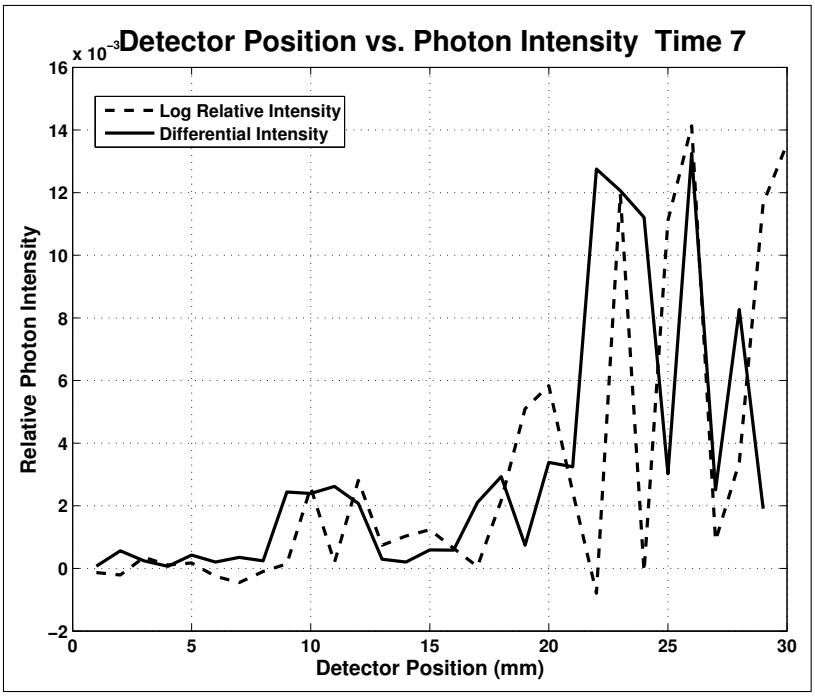

Figure A.15 Intensity Curves for Time 7, 1-30 mm, Arbitrary Changes.

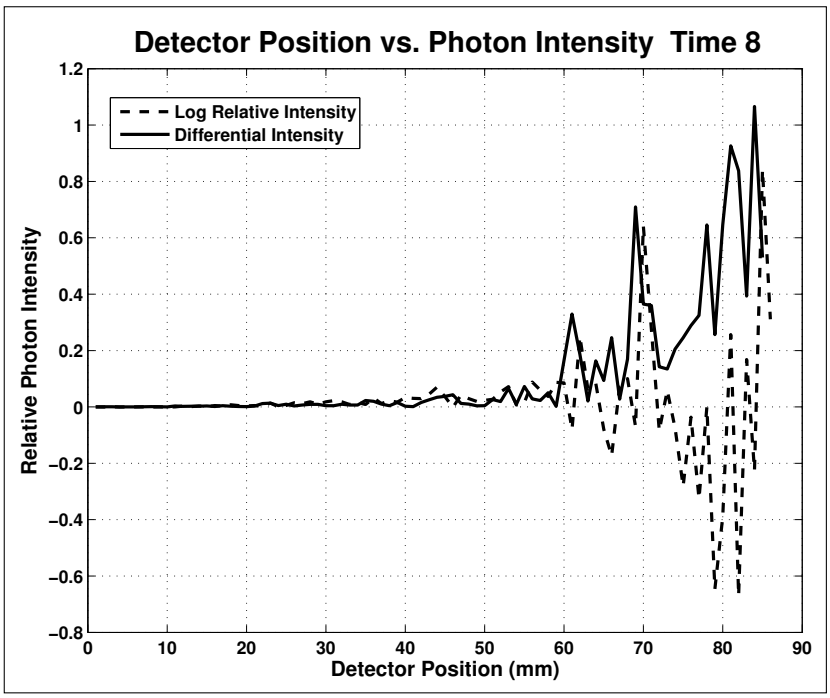

Figure A.16 Intensity Curves for Time 8, 1-100 mm, Arbitrary Changes.

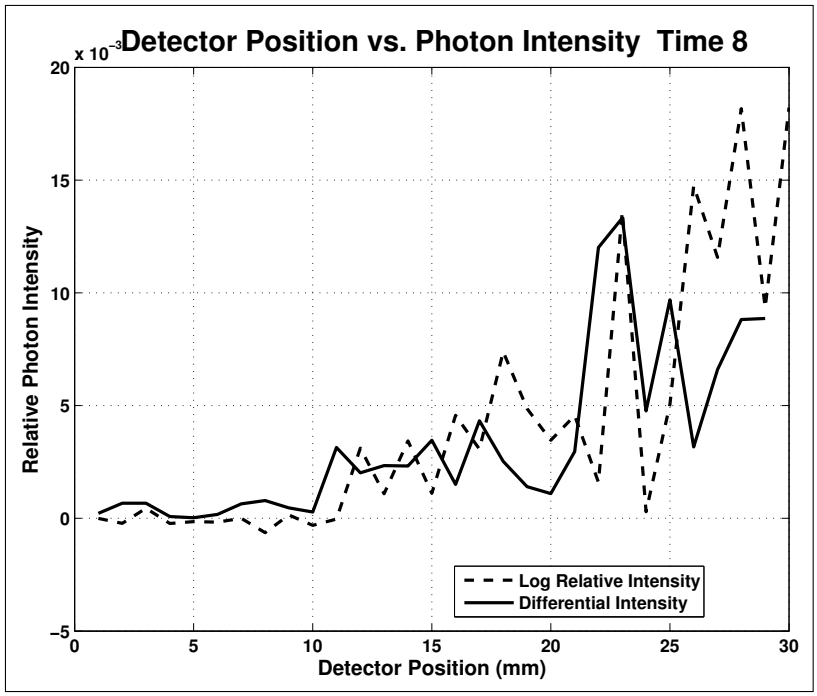

Figure A.17 Intensity Curves for Time 8, 1-30 mm, Arbitrary Changes.

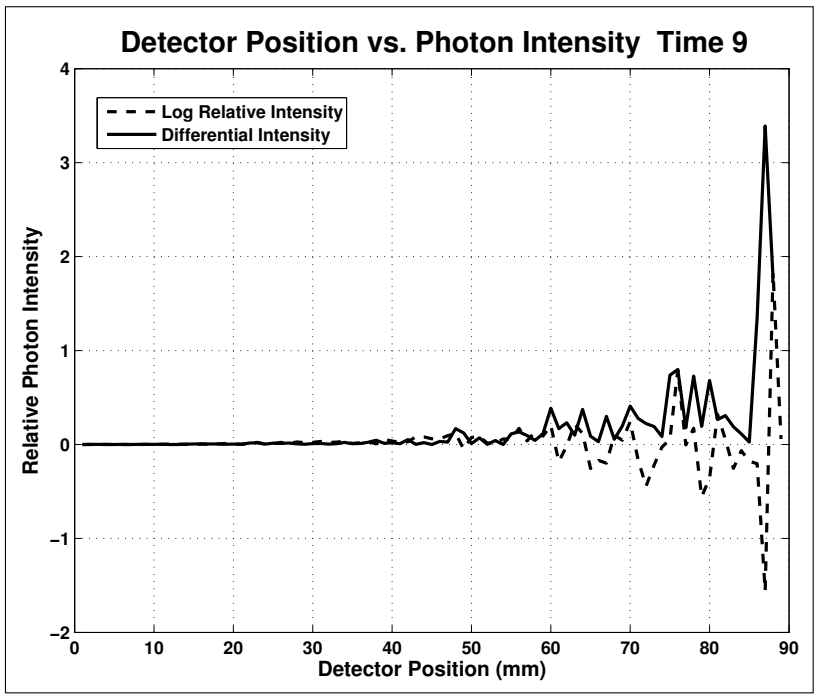

Figure A.18 Intensity Curves for Time 9, 1-100 mm, Arbitrary Changes.

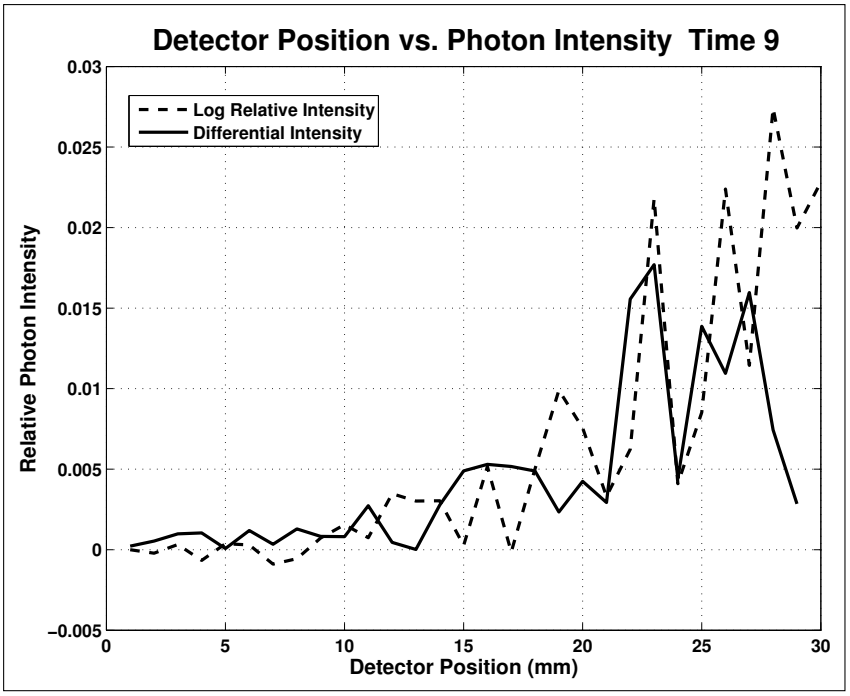

Figure A.19 Intensity Curves for Time 9, 1-30 mm, Arbitrary Changes.

A.1.2 Absorption Changes in GM Layer: Near Far Detector Analysis Figures

A.1.2.1 Relative Intensities

Figure A.20 Relative Photon intensities of the GM Layer μ_a Changes.

A.1.2.2 Differentiation of the Relative Intensities

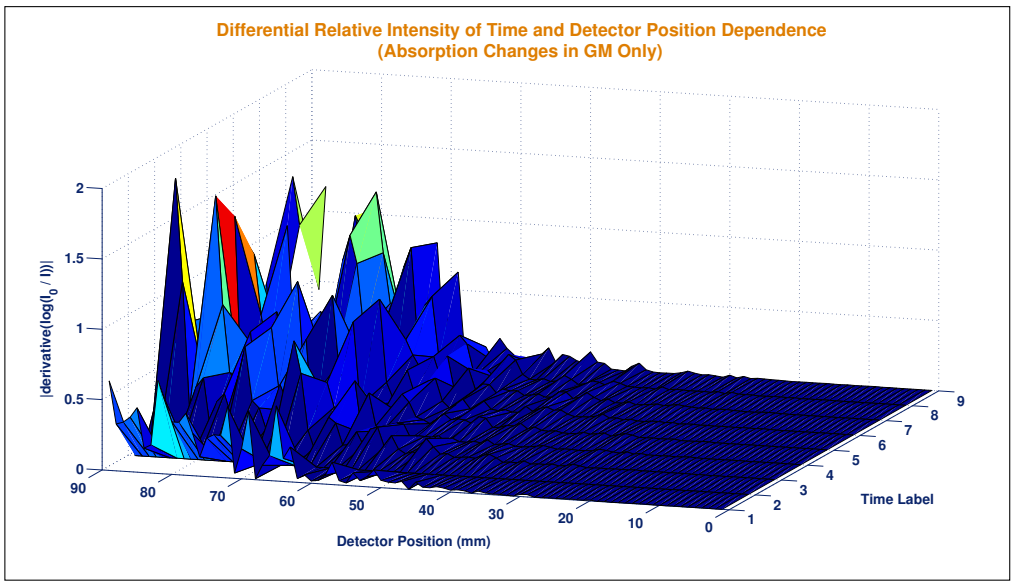

Figure A.21 Differentiation Photon intensities of the GM Layer μ_a Changes.

A.1.2.3 Intensity Curves for each Time Label

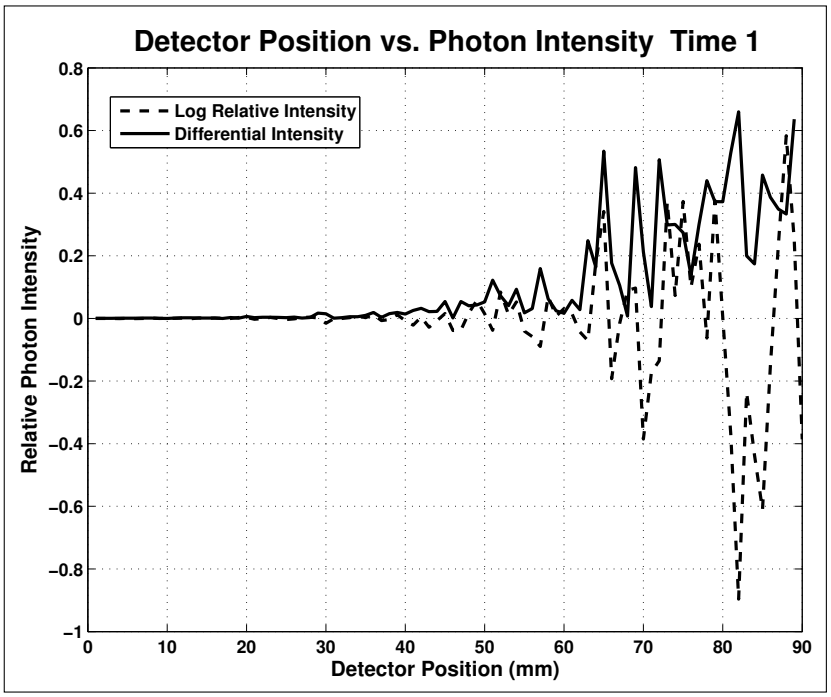

Figure A.22 Intensity Curves for Time 1, 1-100 mm, GM Changes.

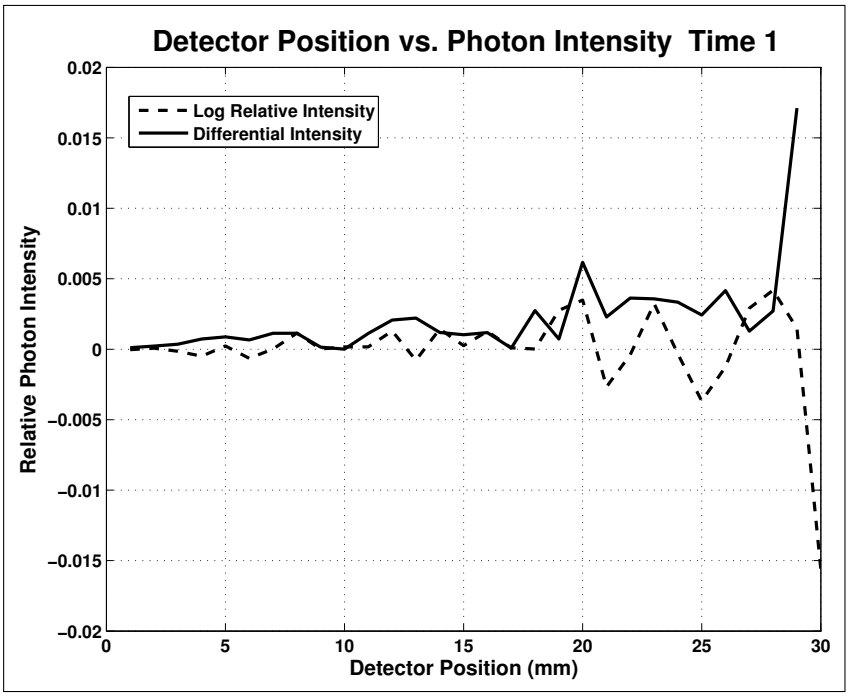

Figure A.23 Intensity Curves for Time 1, 1-30 mm, GM Changes.

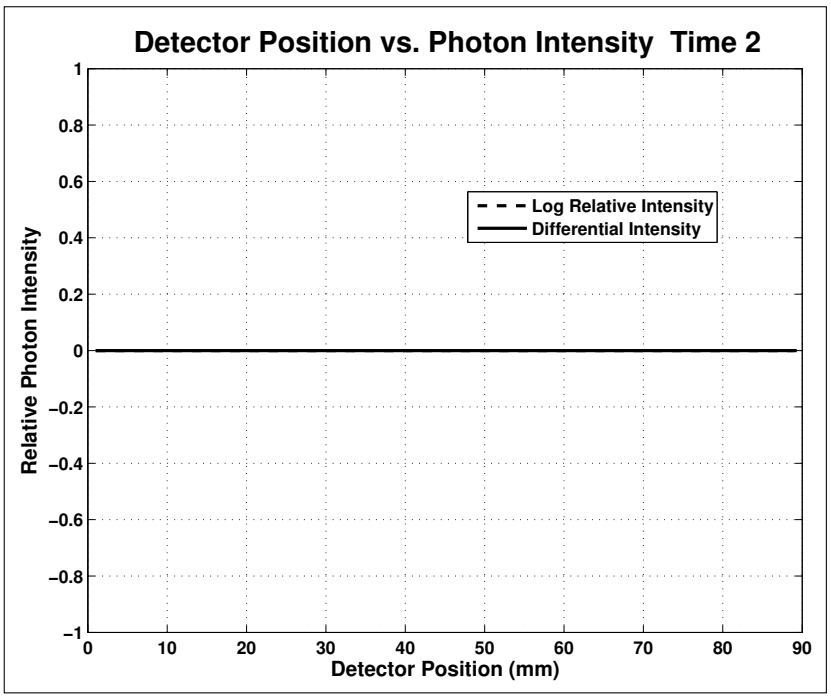

Figure A.24 Intensity Curves for Time 2, 1-100 mm, GM Changes.

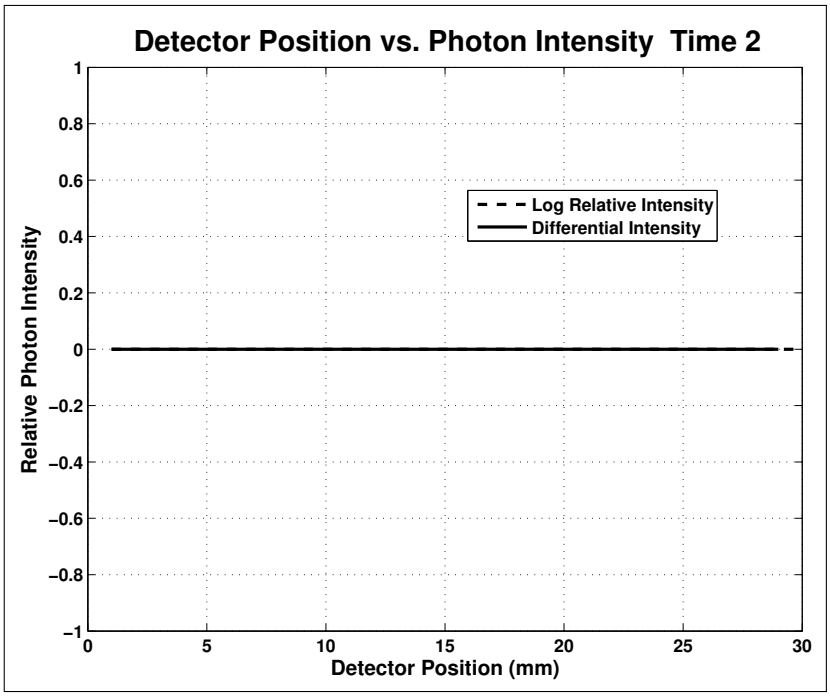

Figure A.25 Intensity Curves for Time 2, 1-30 mm, GM Changes.

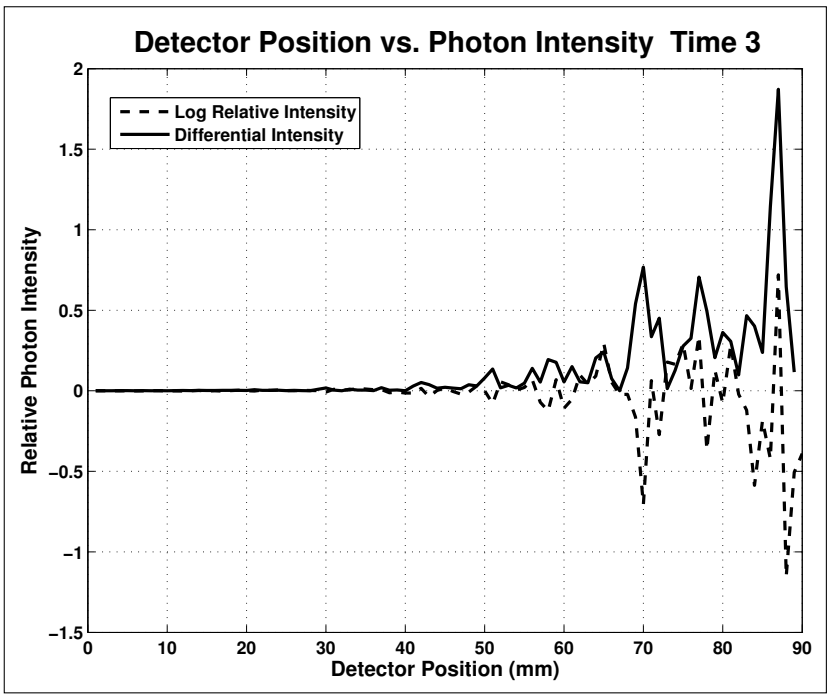

Figure A.26 Intensity Curves for Time 3, 1-100 mm, GM Changes.

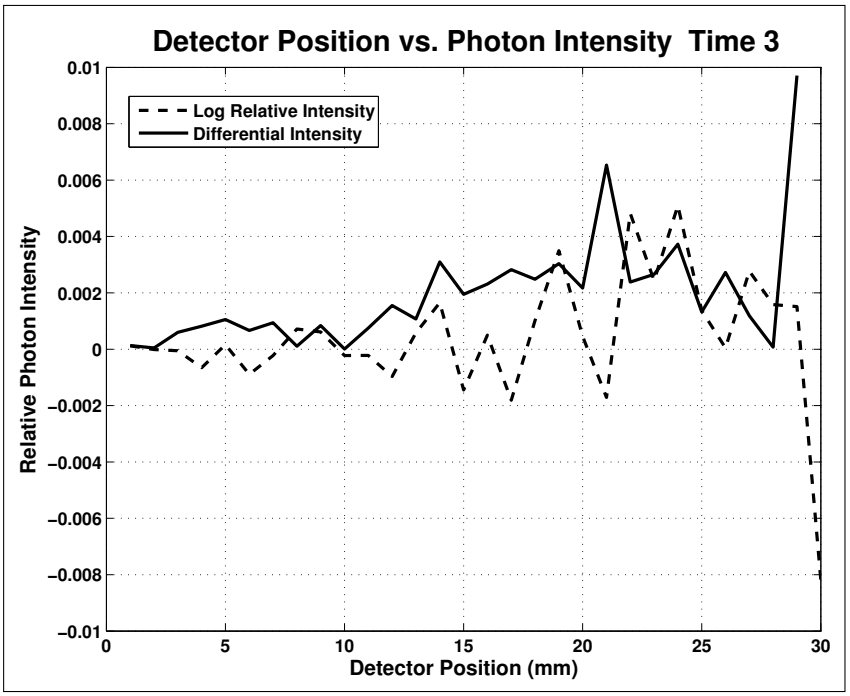

Figure A.27 Intensity Curves for Time 3, 1-30 mm, GM Changes.

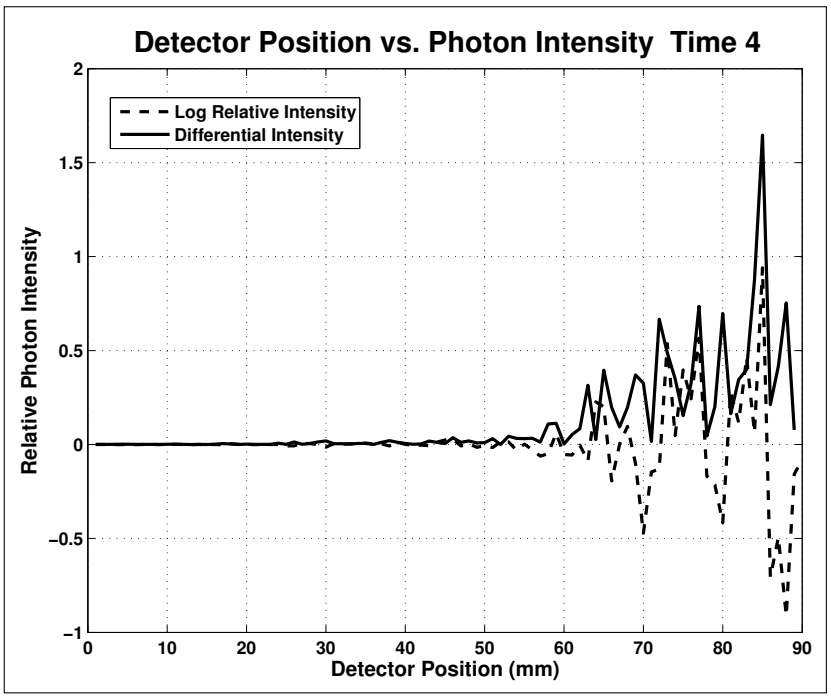

Figure A.28 Intensity Curves for Time 4, 1-100 mm, GM Changes.

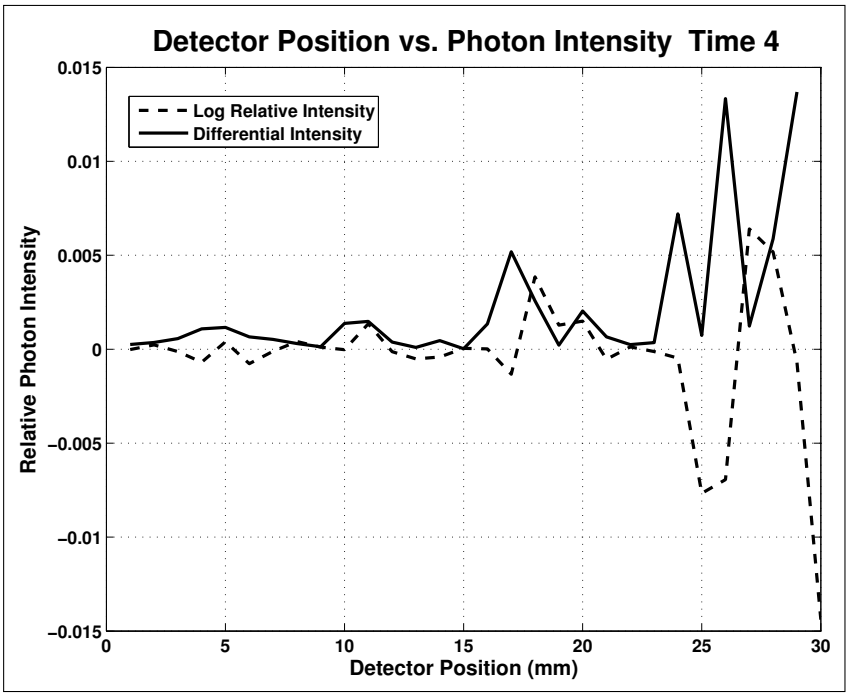

Figure A.29 Intensity Curves for Time 4, 1-30 mm, GM Changes.

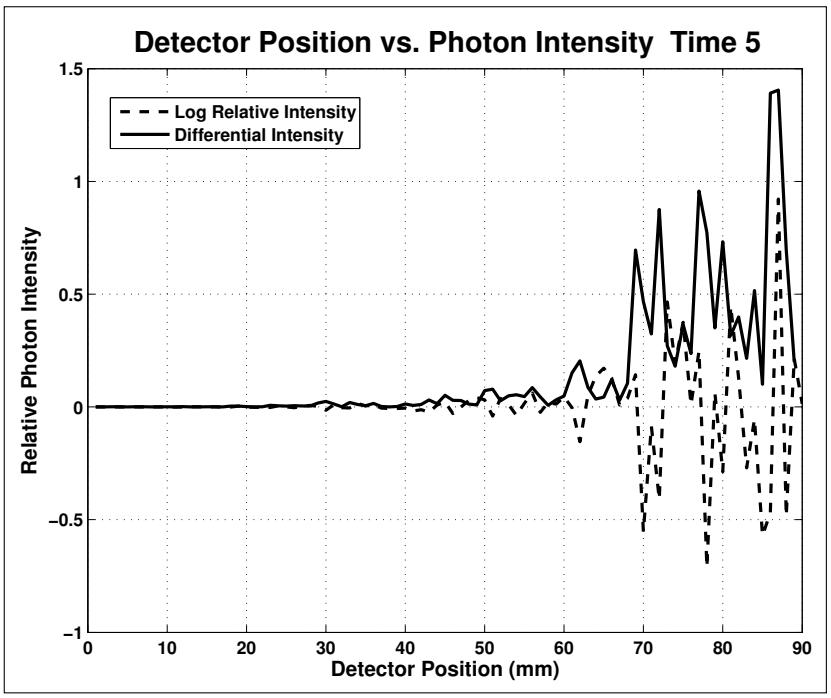

Figure A.30 Intensity Curves for Time 5, 1-100 mm, GM Changes.

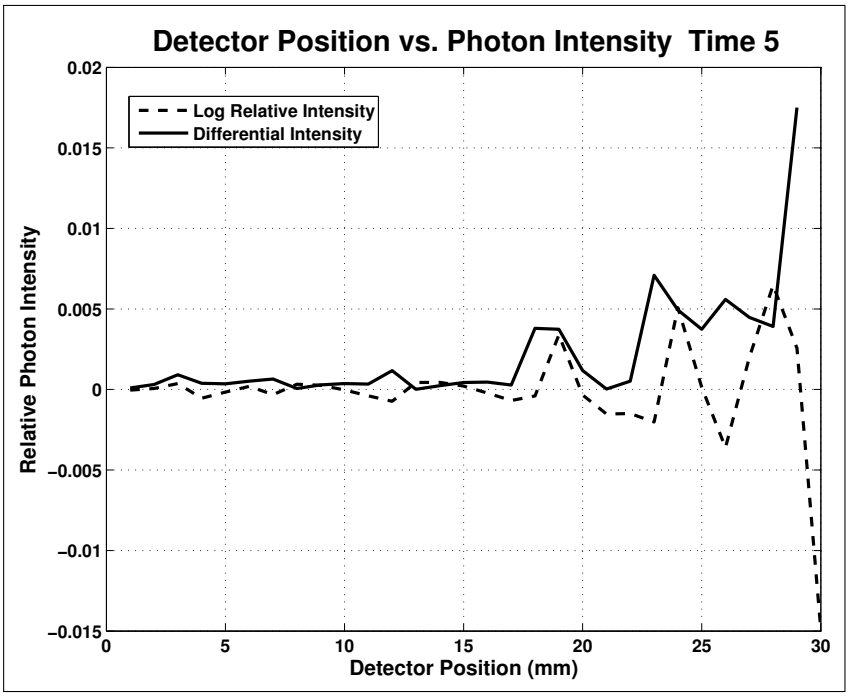

Figure A.31 Intensity Curves for Time 5, 1-30 mm, GM Changes.

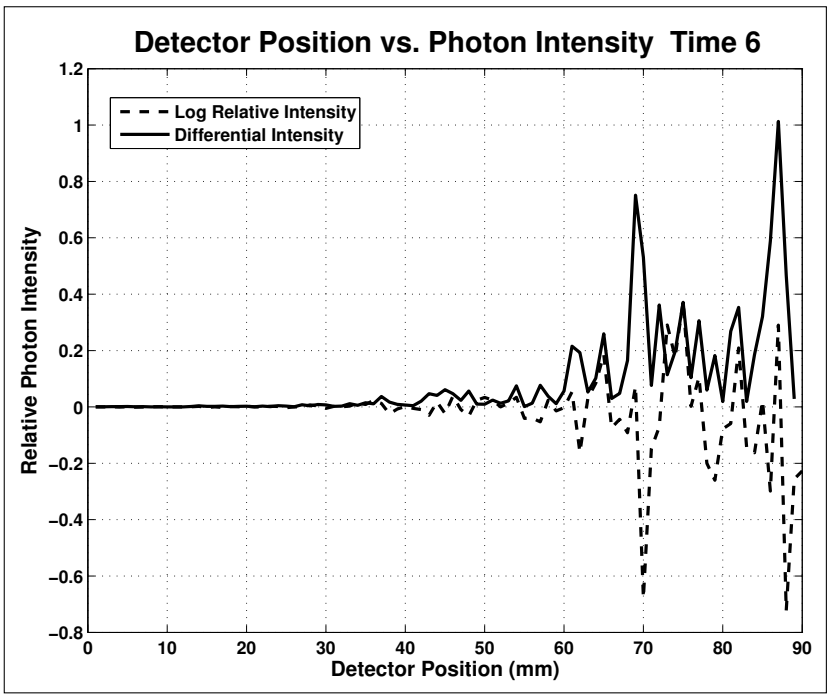

Figure A.32 Intensity Curves for Time 6, 1-100 mm, GM Changes.

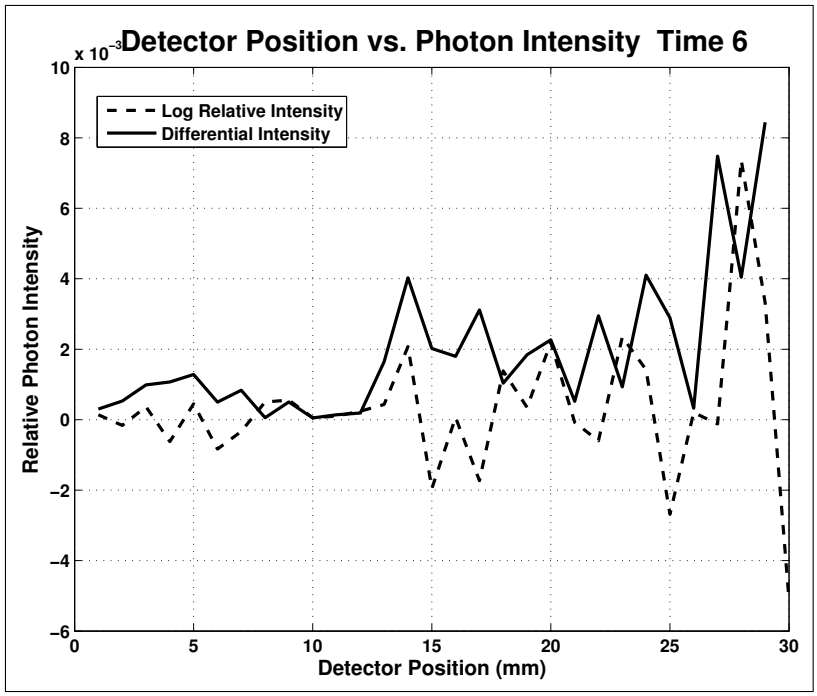

Figure A.33 Intensity Curves for Time 6, 1-30 mm, GM Changes.

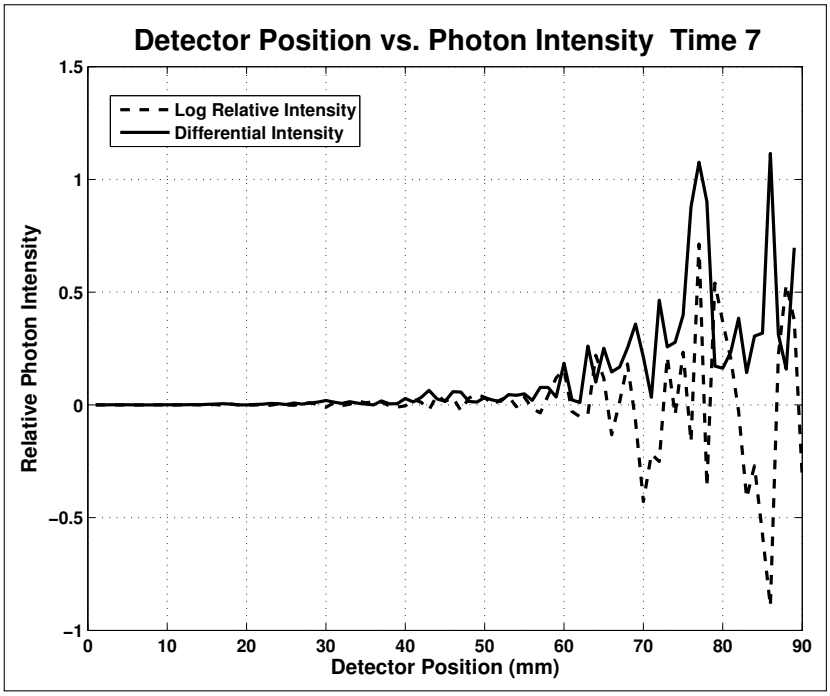

Figure A.34 Intensity Curves for Time 7, 1-100 mm, GM Changes.

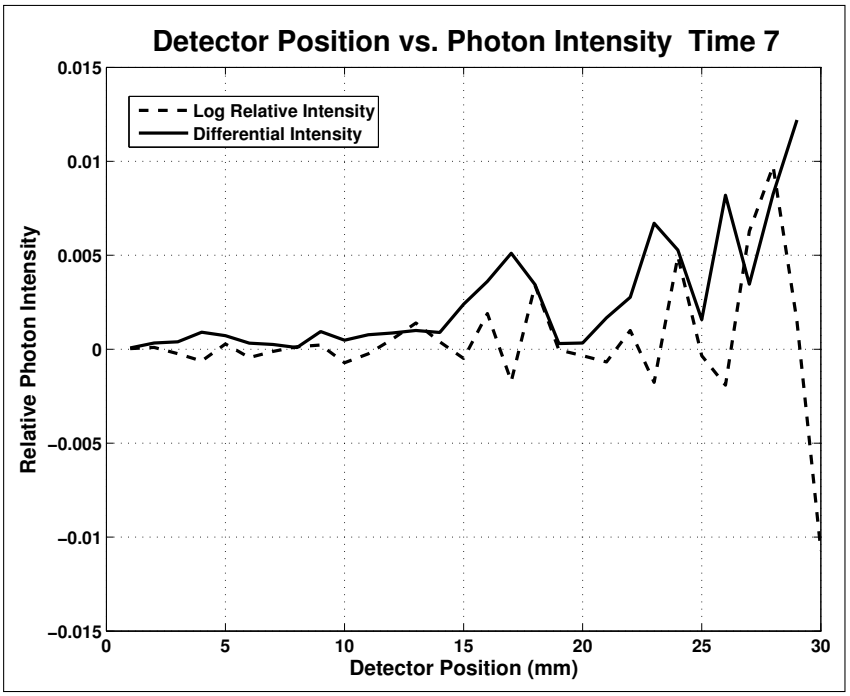

Figure A.35 Intensity Curves for Time 7, 1-30 mm, GM Changes.

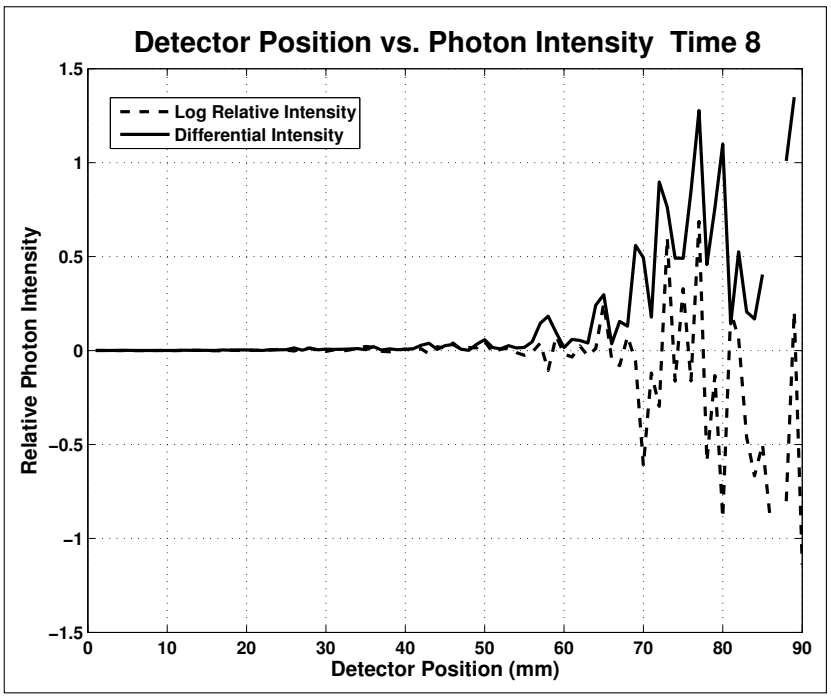

Figure A.36 Intensity Curves for Time 8, 1-100 mm, GM Changes.

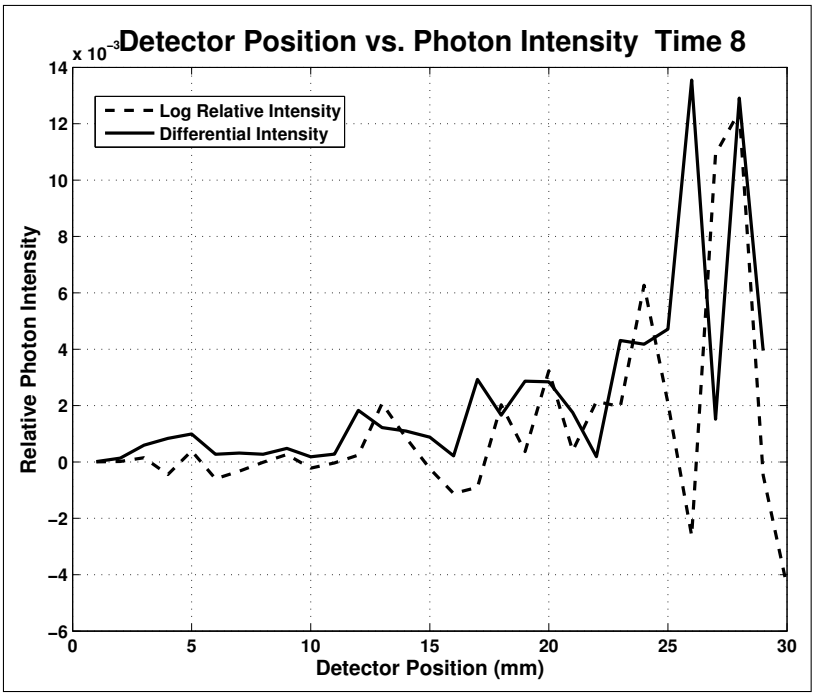

Figure A.37 Intensity Curves for Time 8, 1-30 mm, GM Changes.

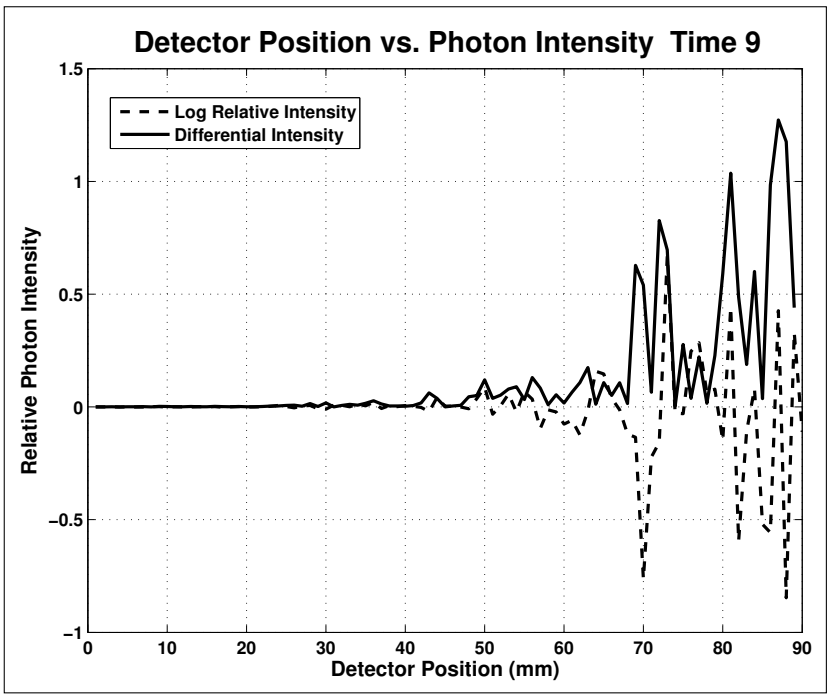

Figure A.38 Intensity Curves for Time 9, 1-100 mm, GM Changes.

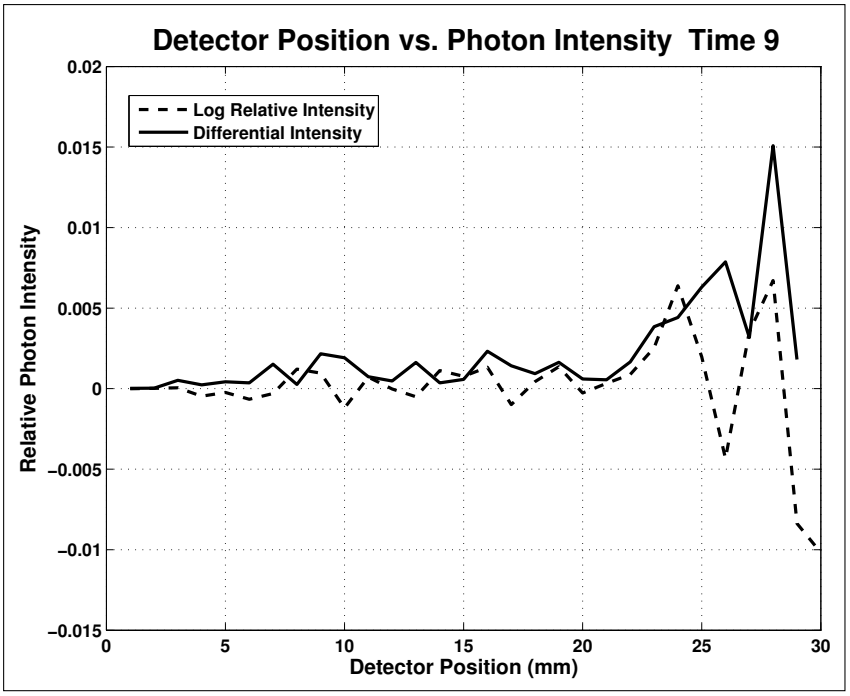

Figure A.39 Intensity Curves for Time 9, 1-30 mm, GM Changes.

A.1.3 Absorption Changes in GM and Scalp Layers: Near Far Detector Analysis Figures

A.1.3.1 Relative Intensities

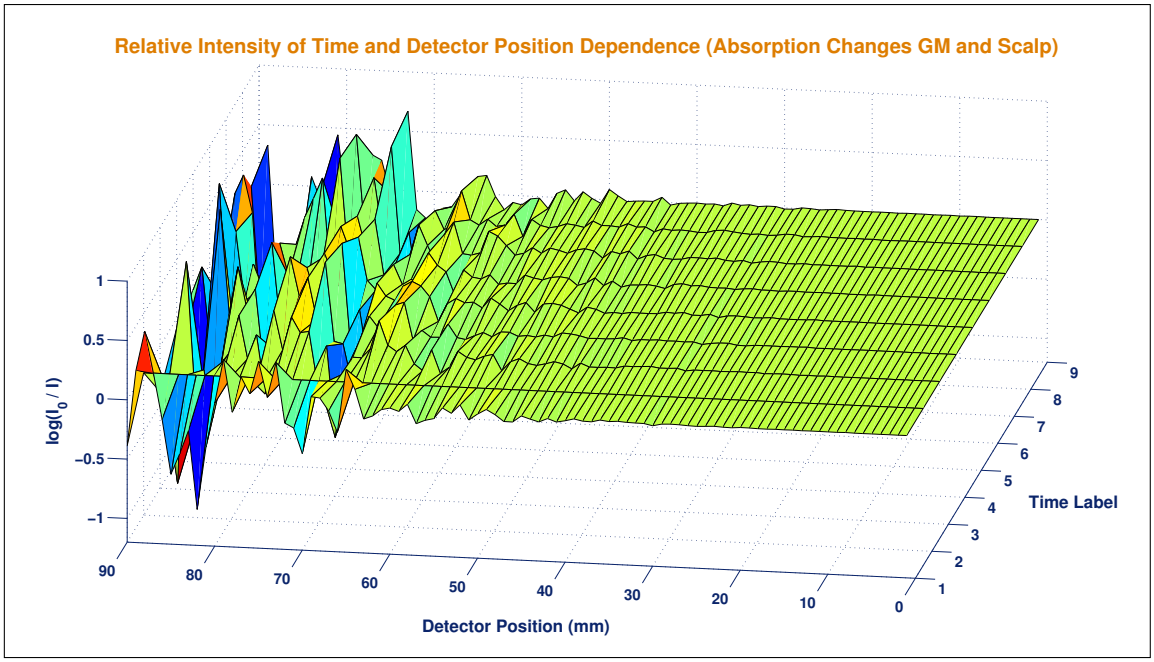

Figure A.40 Relative Photon intensities of the GM and Scalp Layers μ_a Changes.

A.1.3.2 Intensity Curves for each Time Label

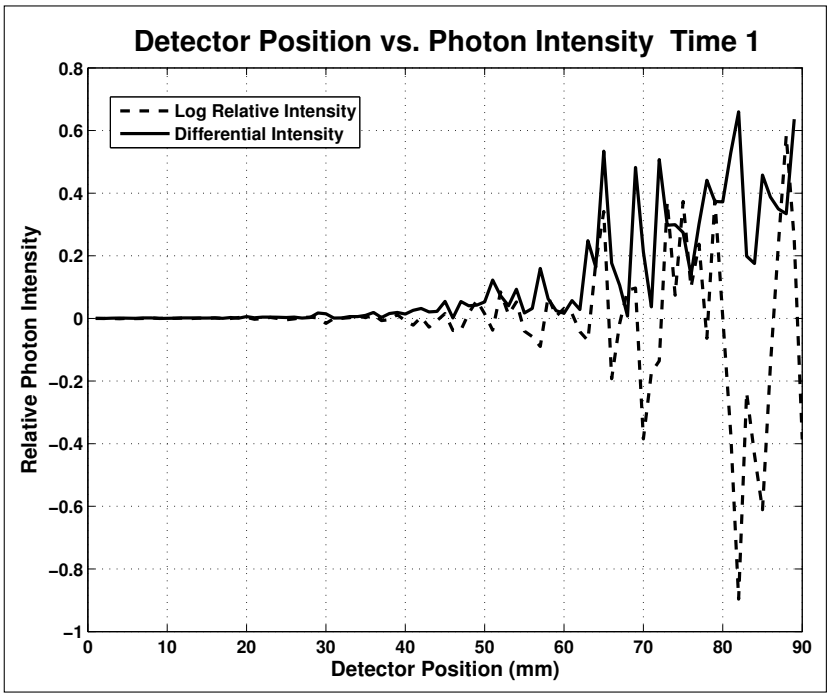

Figure A.41 Intensity Curves for Time 1, 1-100 mm, GM and Scalp Changes.

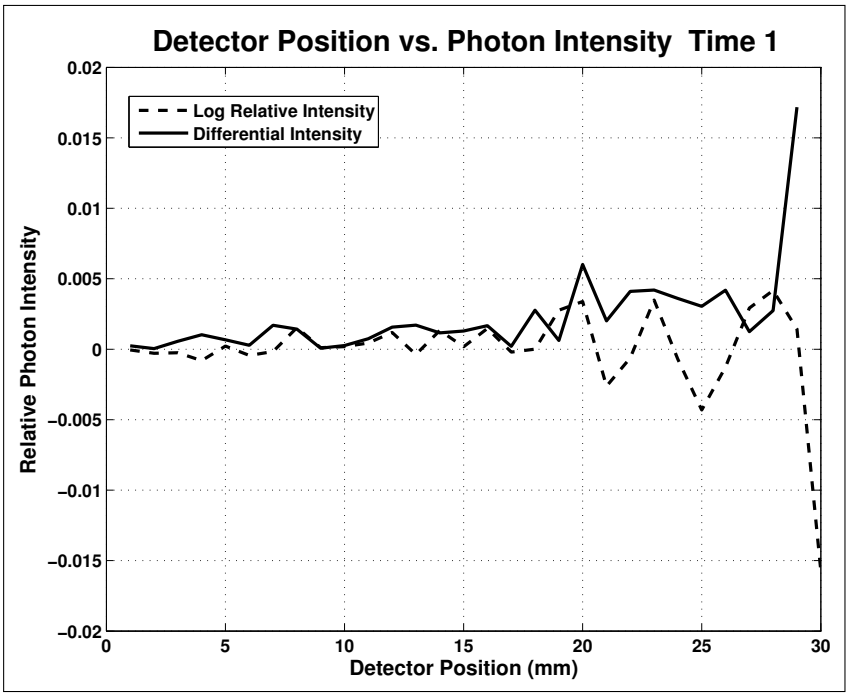

Figure A.42 Intensity Curves for Time 1, 1-30 mm, GM and Scalp Changes.

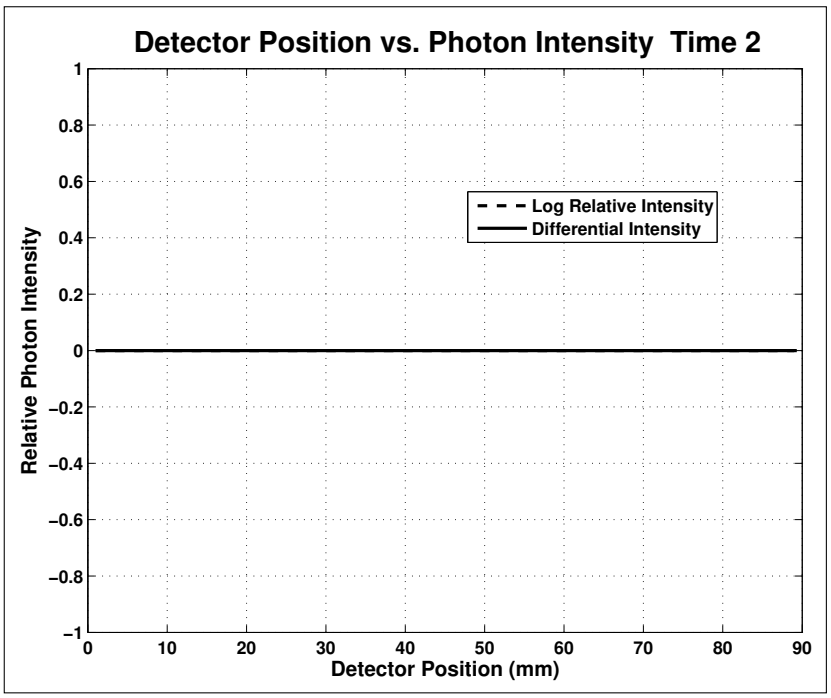

Figure A.43 Intensity Curves for Time 2, 1-100 mm, GM and Scalp Changes.

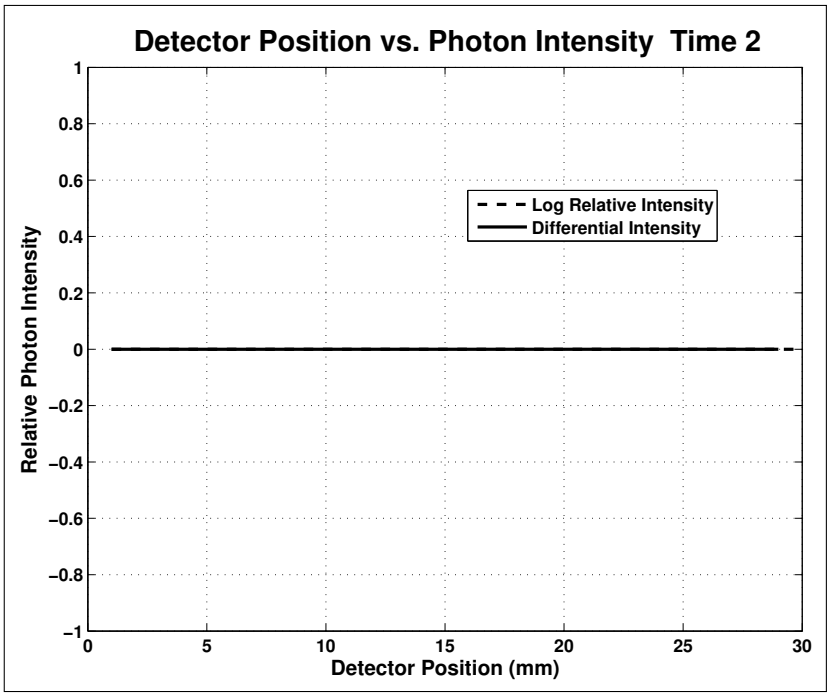

Figure A.44 Intensity Curves for Time 2, 1-30 mm, GM and Scalp Changes.

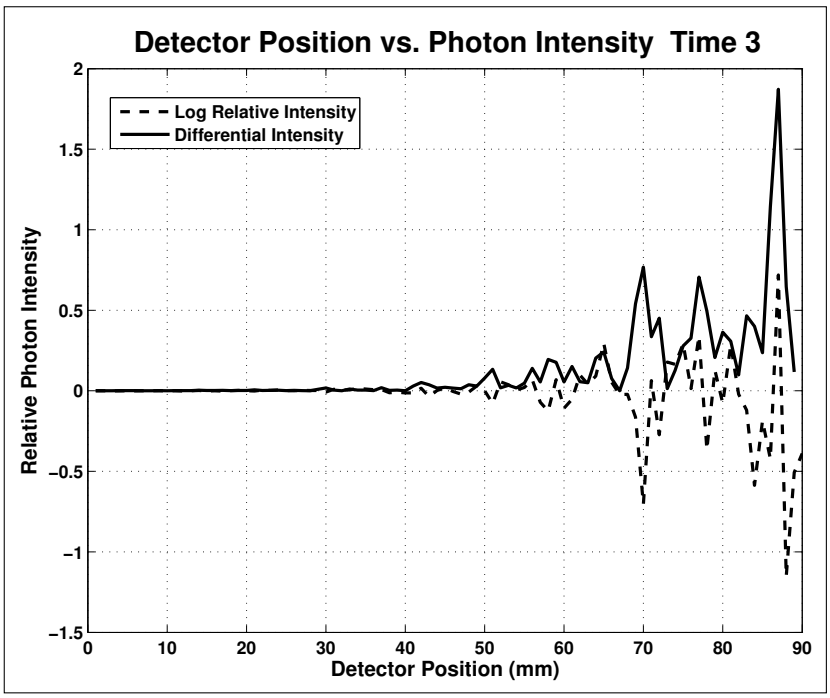

Figure A.45 Intensity Curves for Time 3, 1-100 mm, GM and Scalp Changes.

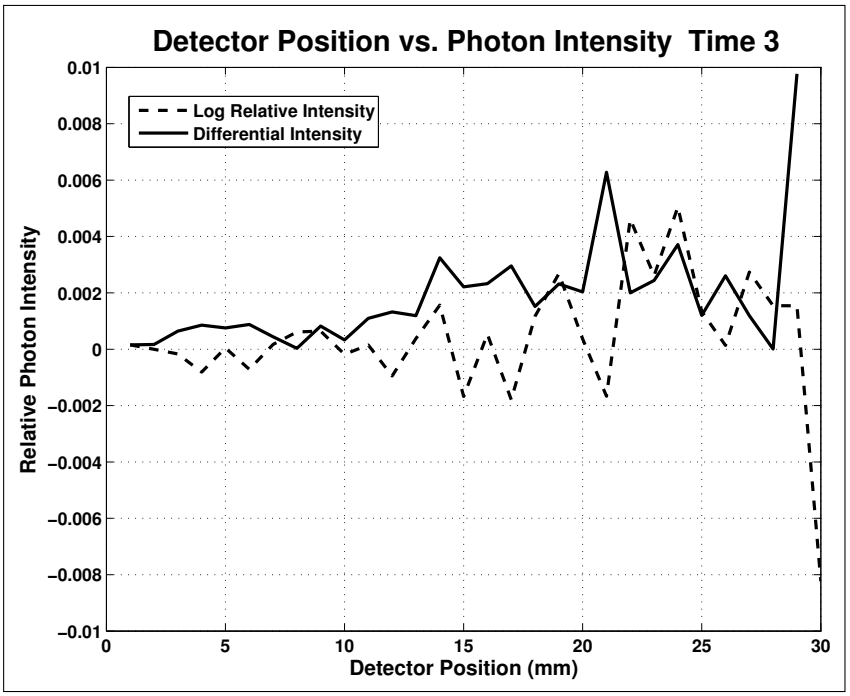

Figure A.46 Intensity Curves for Time 3, 1-30 mm, GM and Scalp Changes.

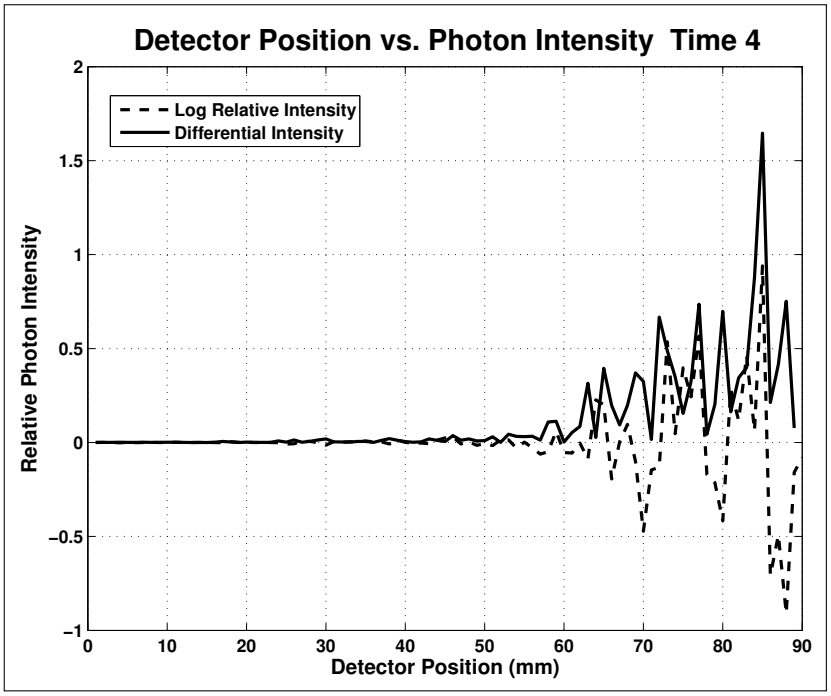

Figure A.47 Intensity Curves for Time 4, 1-100 mm, GM and Scalp Changes.

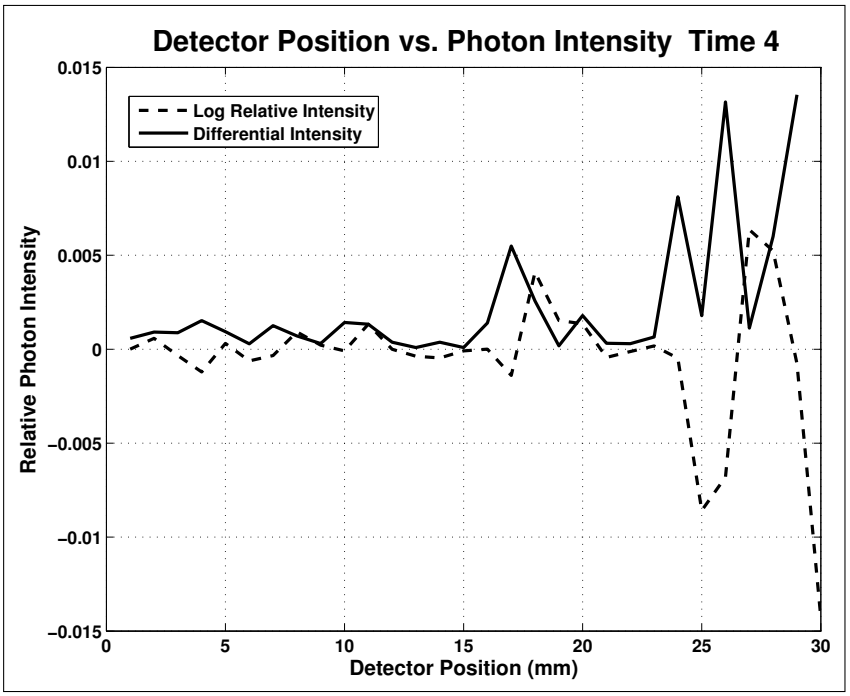

Figure A.48 Intensity Curves for Time 4, 1-30 mm, GM and Scalp Changes.

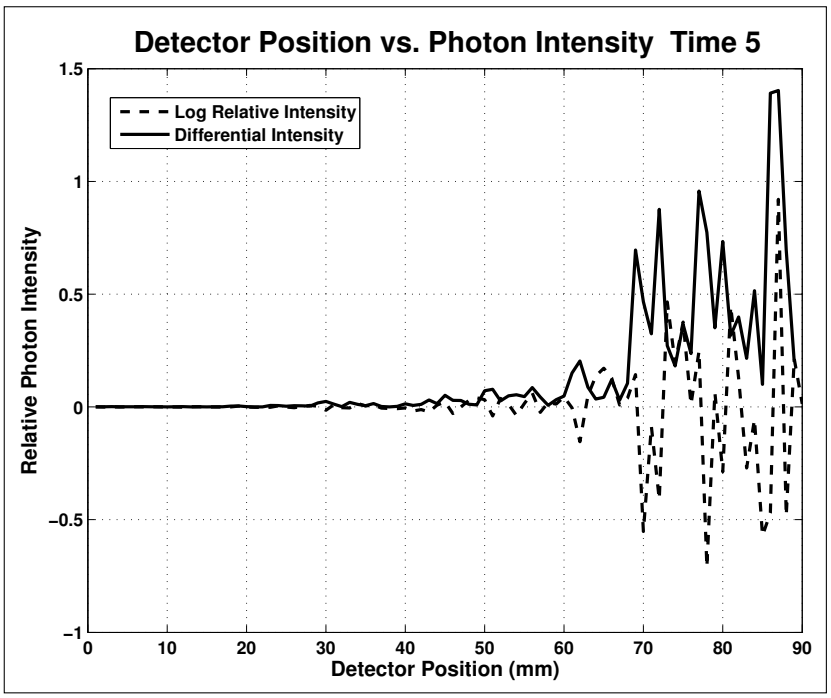

Figure A.49 Intensity Curves for Time 5, 1-100 mm, GM and Scalp Changes.

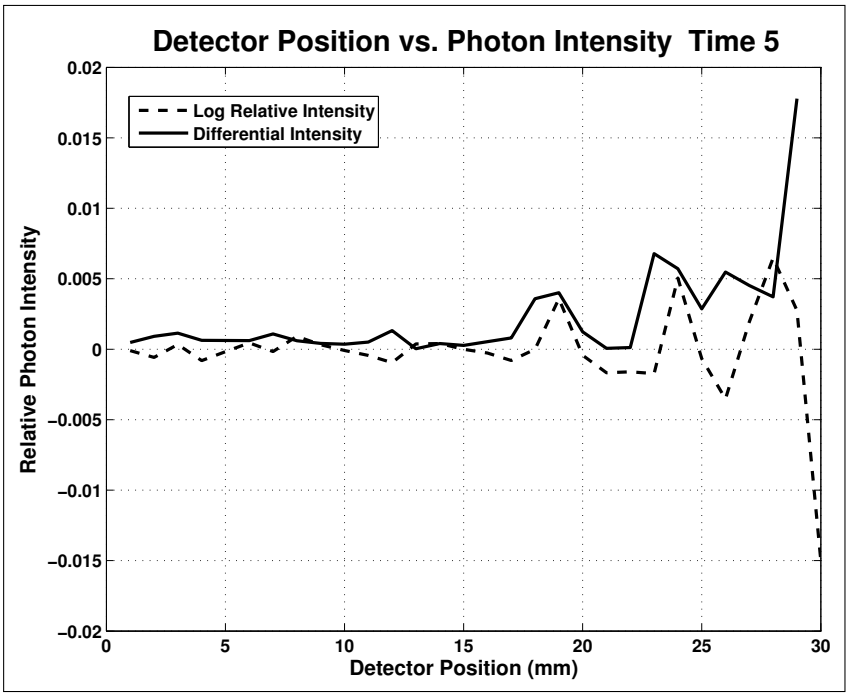

Figure A.50 Intensity Curves for Time 5, 1-30 mm, GM and Scalp Changes.

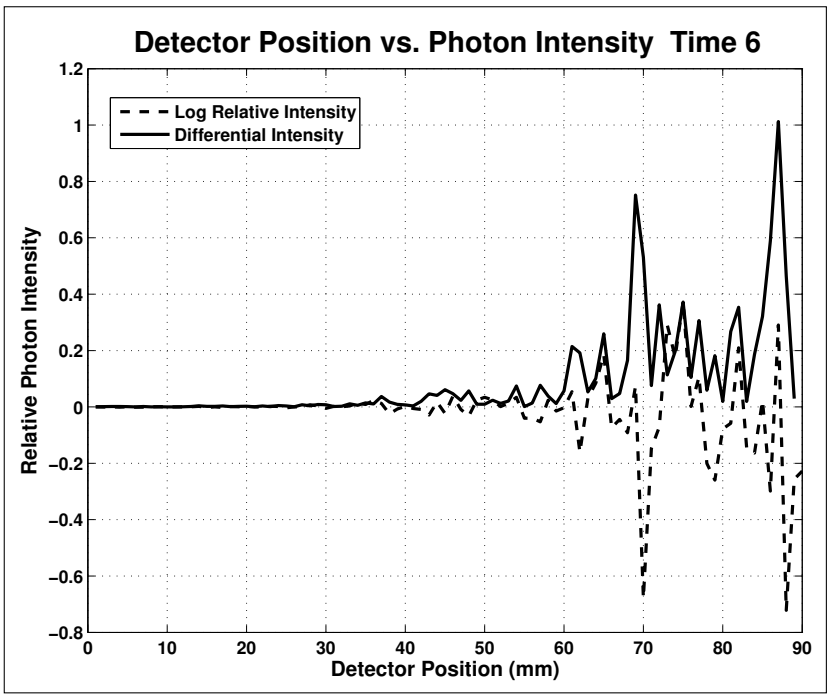

Figure A.51 Intensity Curves for Time 6, 1-100 mm, GM and Scalp Changes.

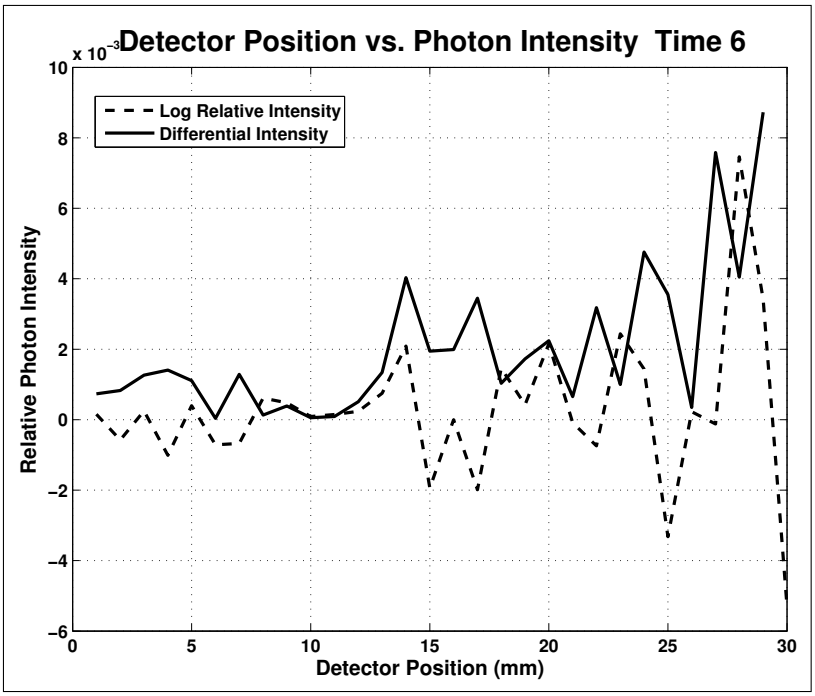

Figure A.52 Intensity Curves for Time 6, 1-30 mm, GM and Scalp Changes.

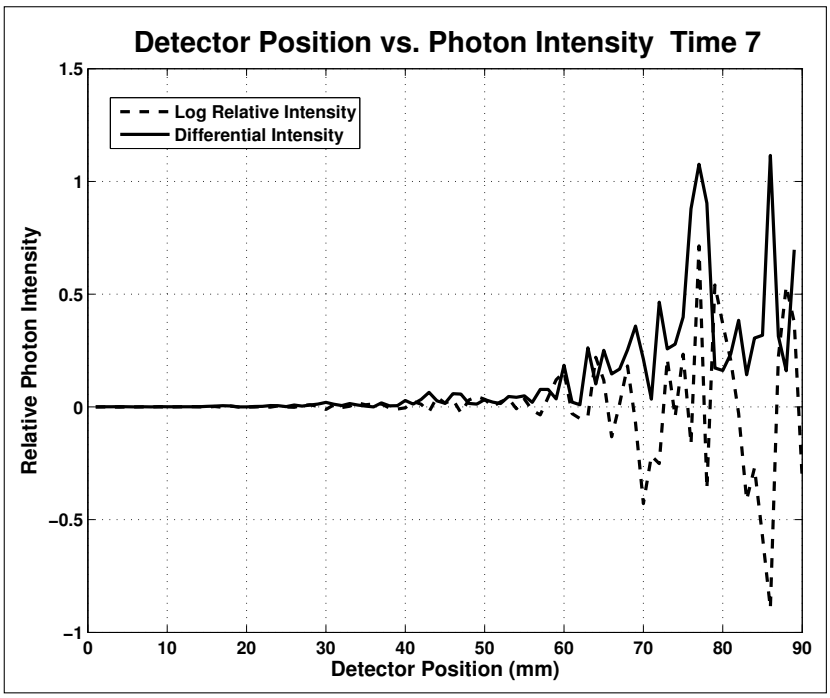

Figure A.53 Intensity Curves for Time 7, 1-100 mm, GM and Scalp Changes.

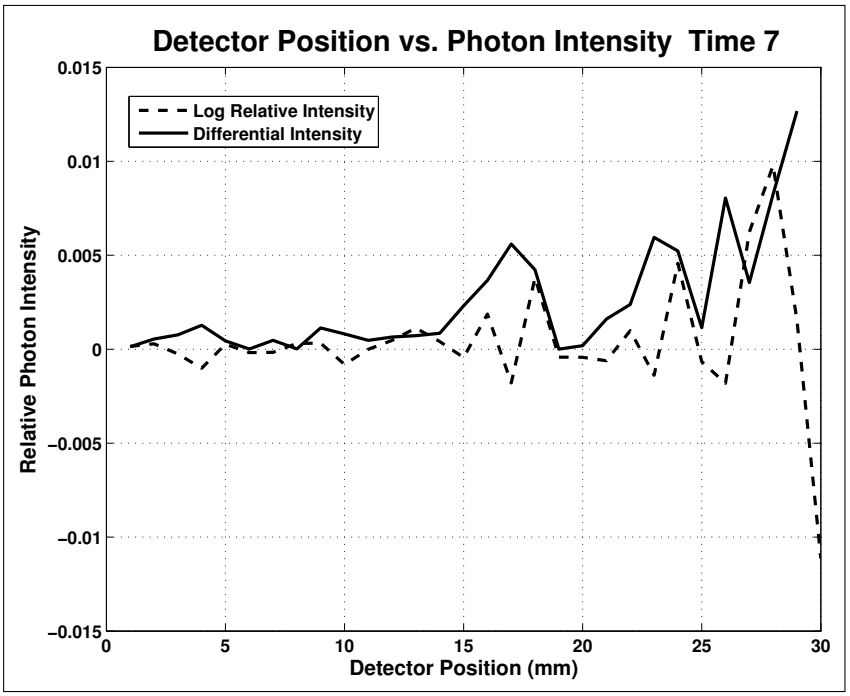

Figure A.54 Intensity Curves for Time 7, 1-30 mm, GM and Scalp Changes.

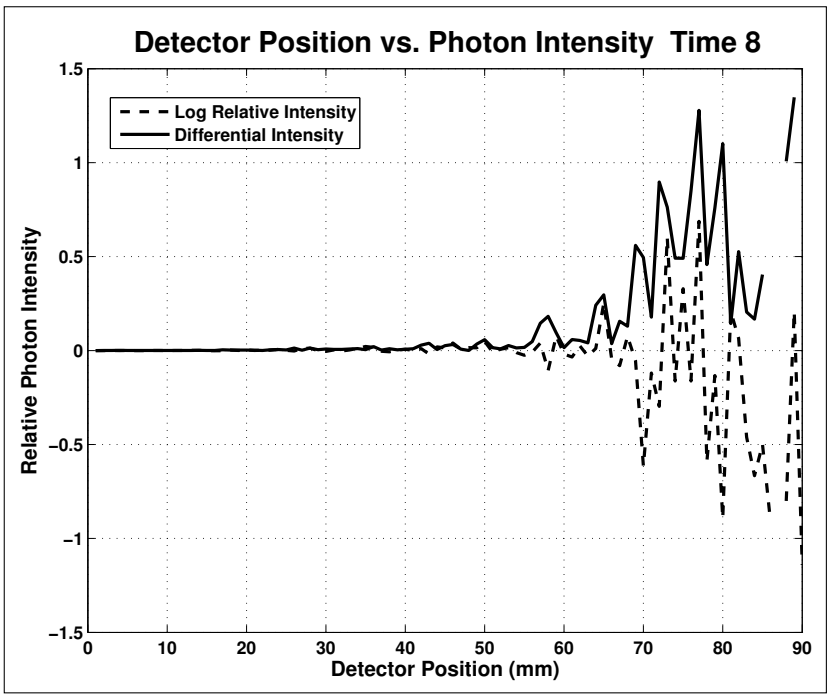

Figure A.55 Intensity Curves for Time 8, 1-100 mm, GM and Scalp Changes.

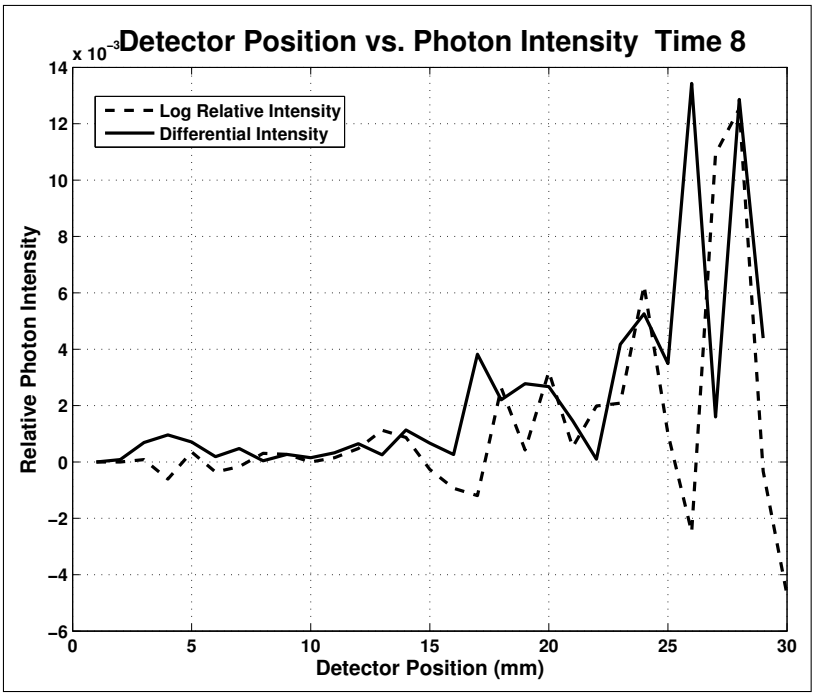

Figure A.56 Intensity Curves for Time 8, 1-30 mm, GM and Scalp Changes.

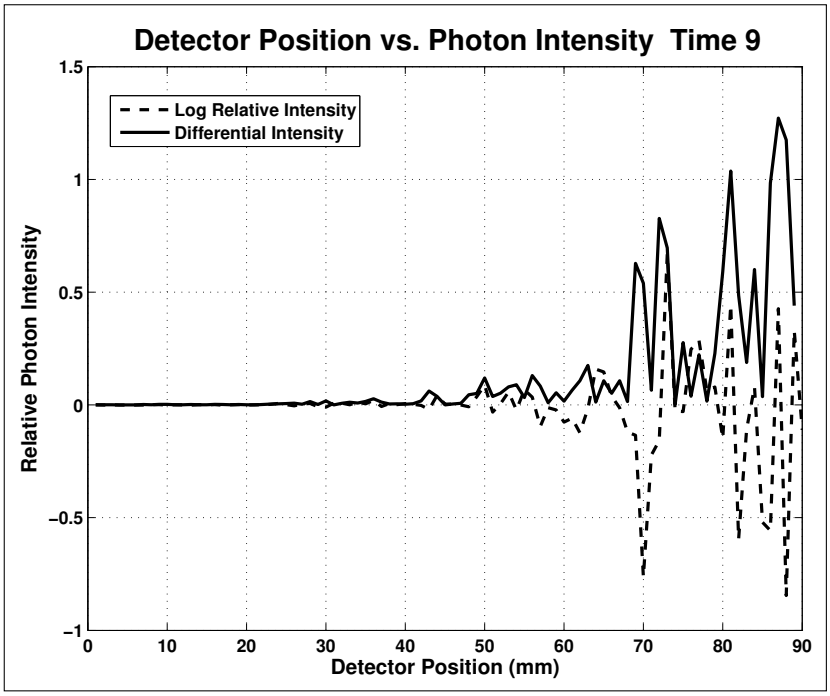

Figure A.57 Intensity Curves for Time 9, 1-100 mm, GM and Scalp Changes.

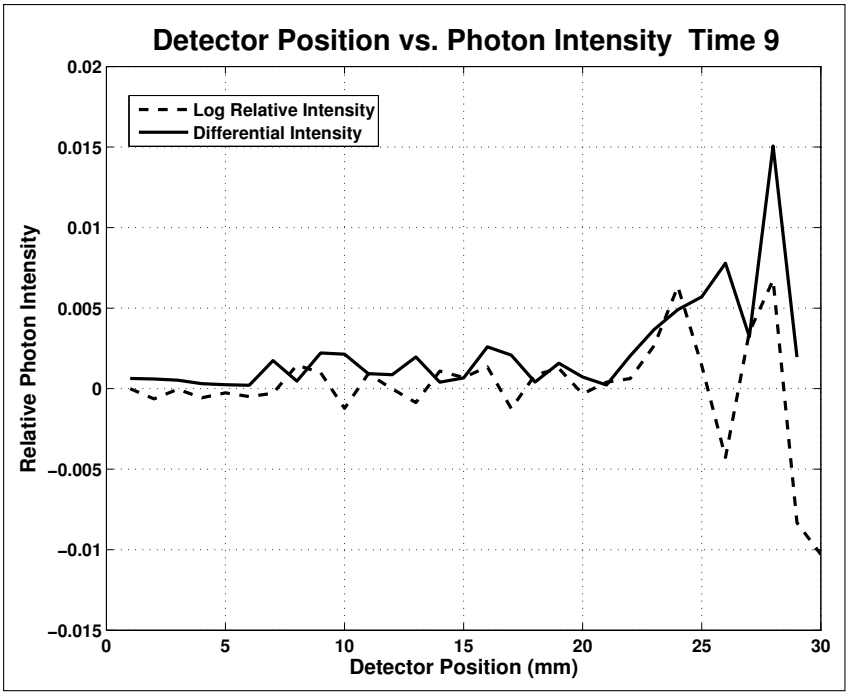

Figure A.58 Intensity Curves for Time 9, 1-30 mm, GM and Scalp Changes.

A.1.4 Absorption Changes in Thin Skull Model: Near Far Detector Analysis Figures

A.1.5 Simulation of the Thin Skull Model Absorption Changes

A.1.5.1 Relative Intensities

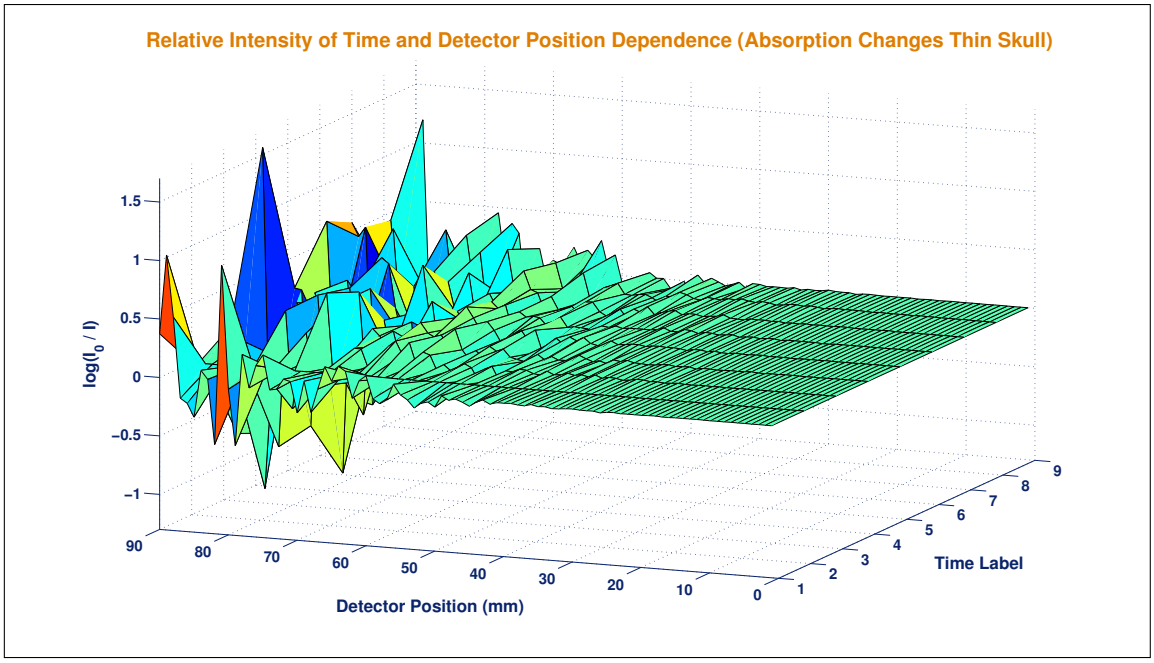

Figure A.59 Relative Photon intensities with a Head Model Mimicking Thin Skull.

A.1.5.2 Differentiation of the Relative Intensities

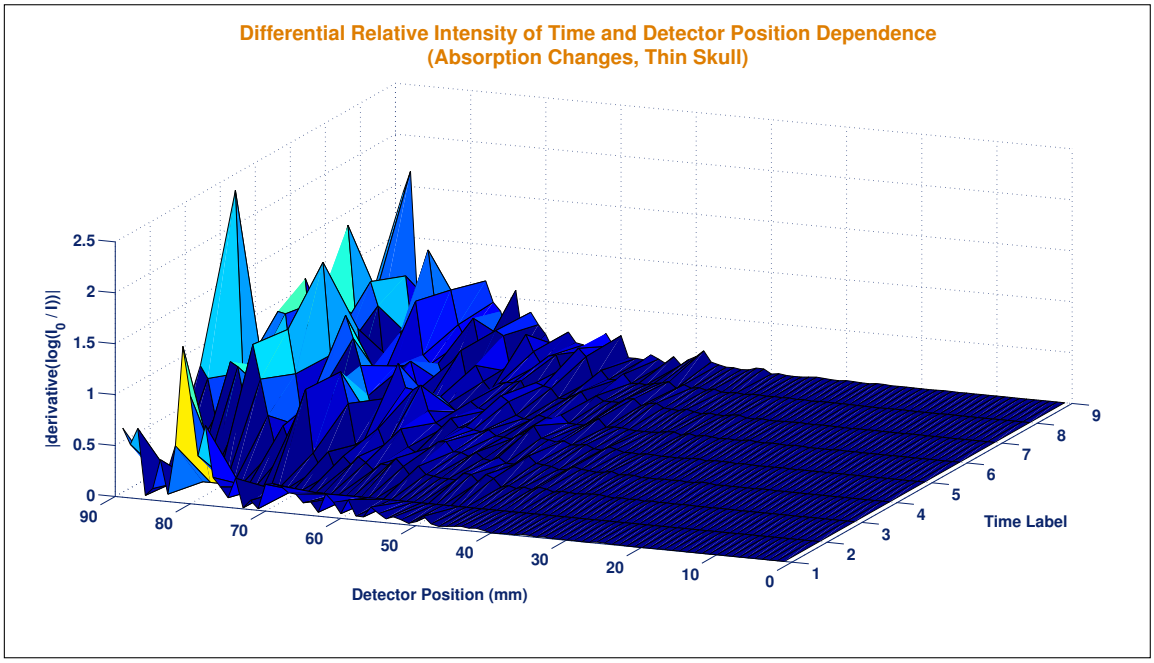

Figure A.60 Differentiation Photon intensities with a Head Model Mimicking Thin Skull.

A.1.5.3 Intensity Curves for each Time Label

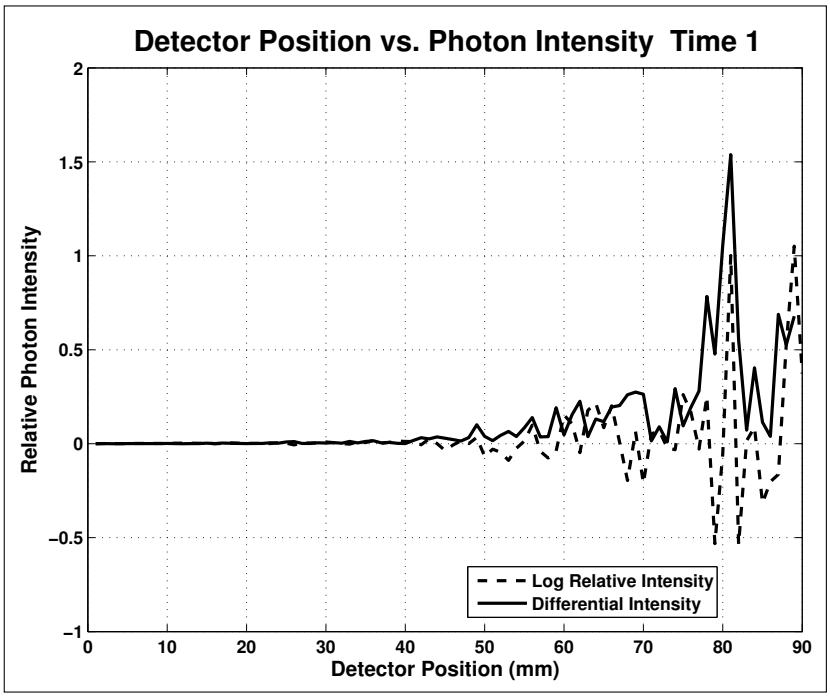

Figure A.61 Intensity Curves for Time 1, 1-100 mm, Thin Skull.

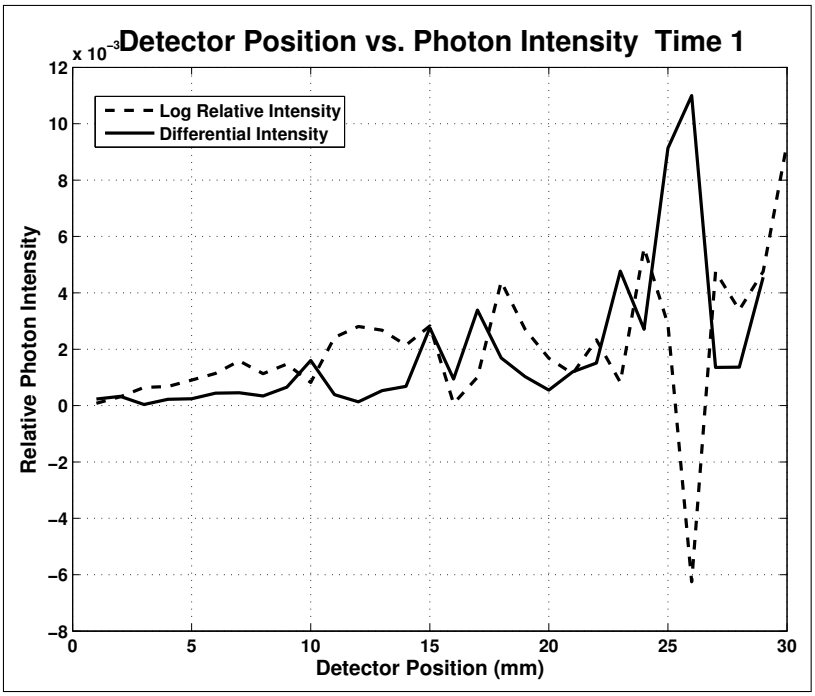

Figure A.62 Intensity Curves for Time 1, 1-30 mm, Thin Skull.

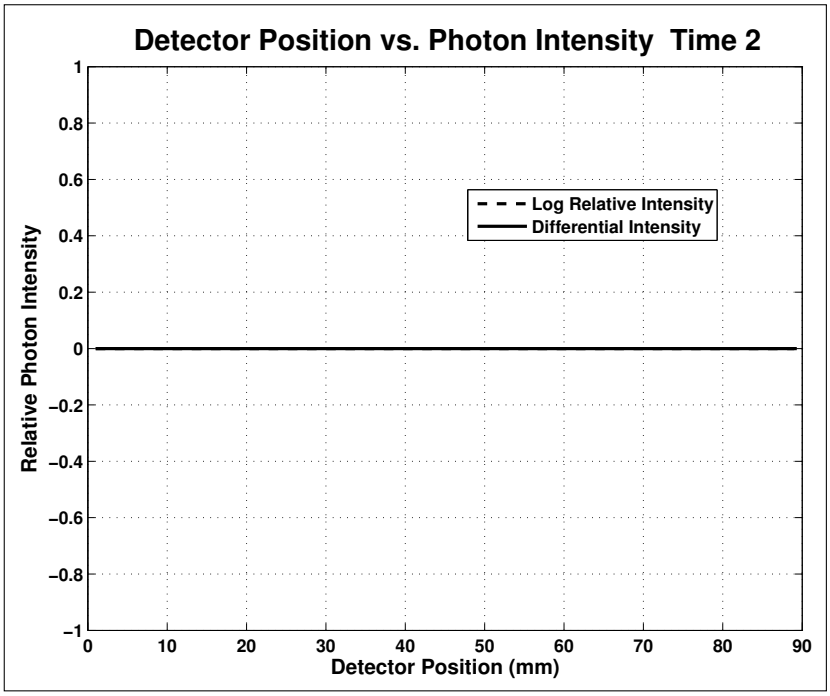

Figure A.63 Intensity Curves for Time 2, 1-100 mm, Thin Skull.

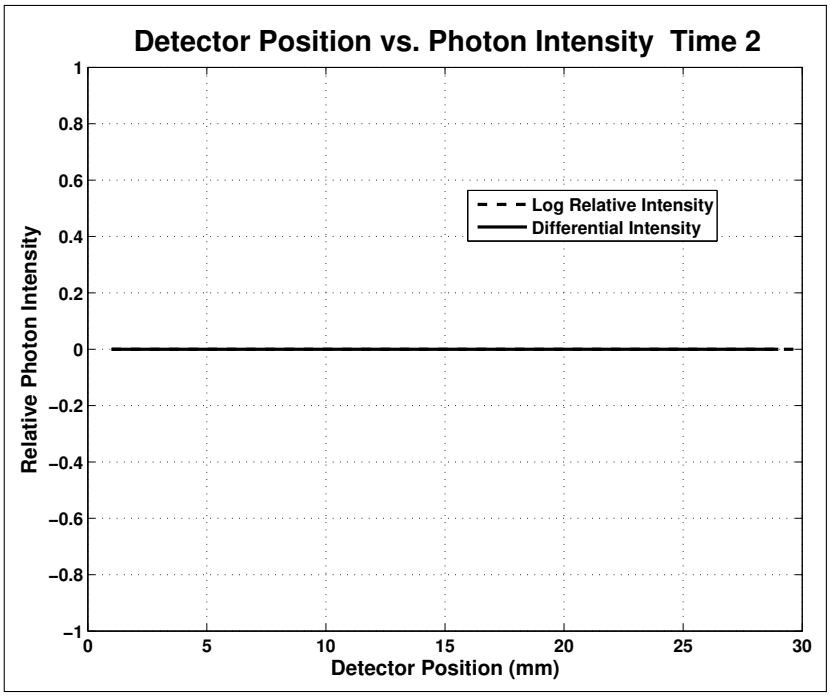

Figure A.64 Intensity Curves for Time 2, 1-30 mm, Thin Skull.

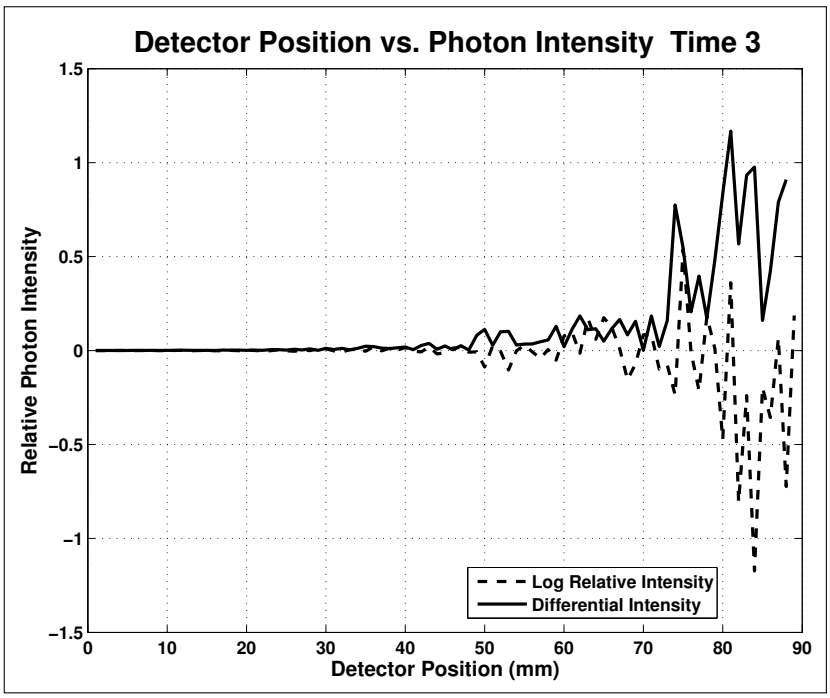

Figure A.65 Intensity Curves for Time 3, 1-100 mm, Thin Skull.

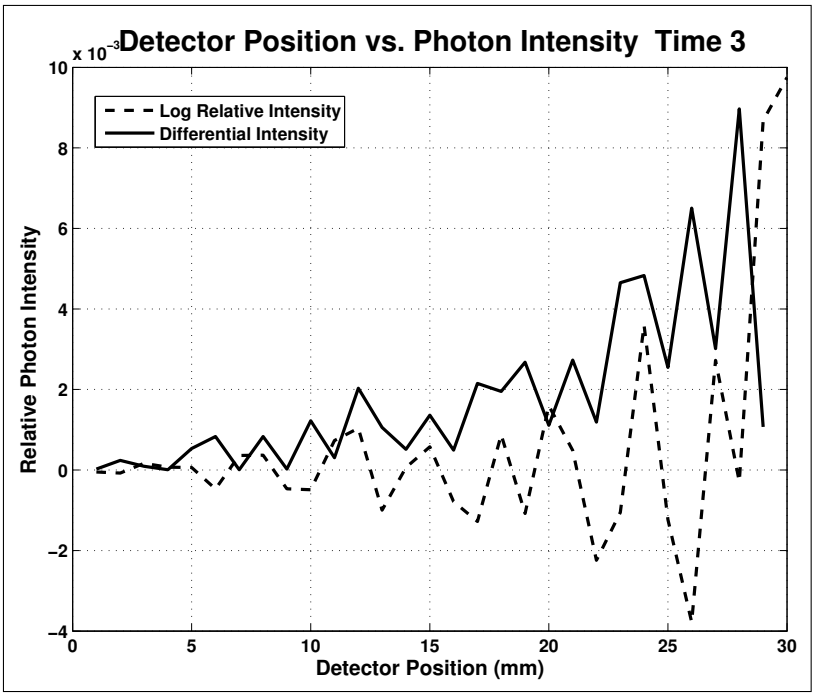

Figure A.66 Intensity Curves for Time 3, 1-30 mm, Thin Skull.

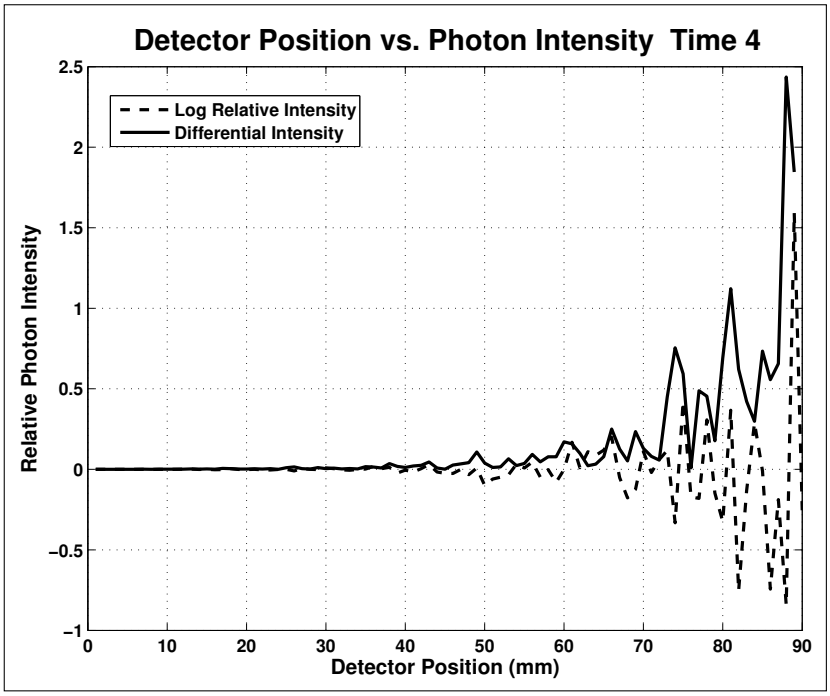

Figure A.67 Intensity Curves for Time 4, 1-100 mm, Thin Skull.

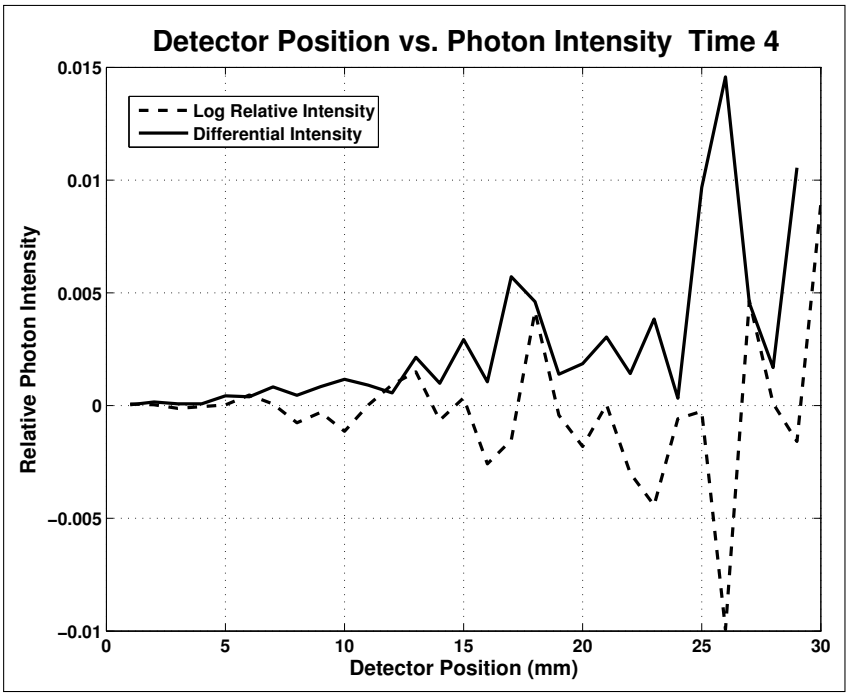

Figure A.68 Intensity Curves for Time 4, 1-30 mm, Thin Skull.

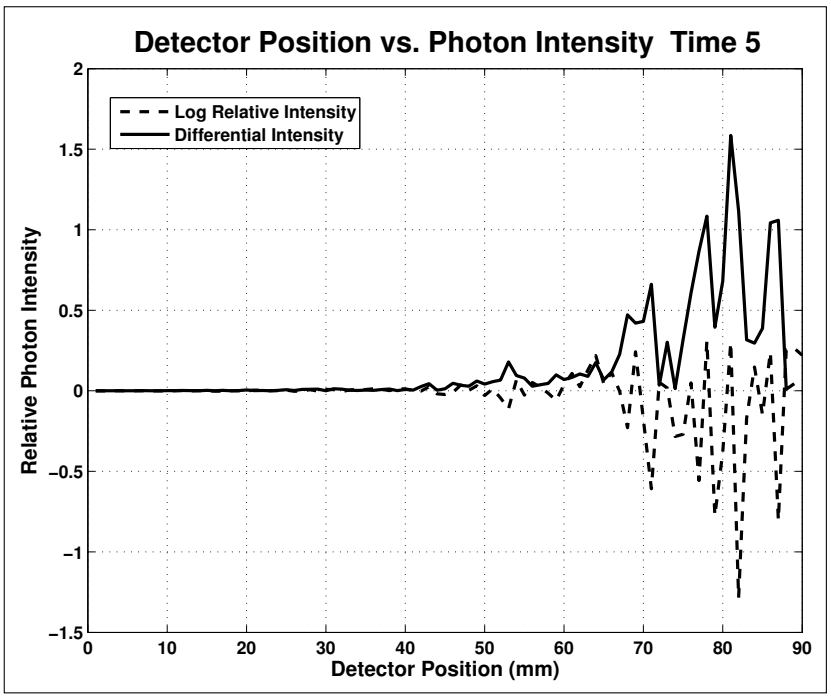

Figure A.69 Intensity Curves for Time 5, 1-100 mm, Thin Skull.

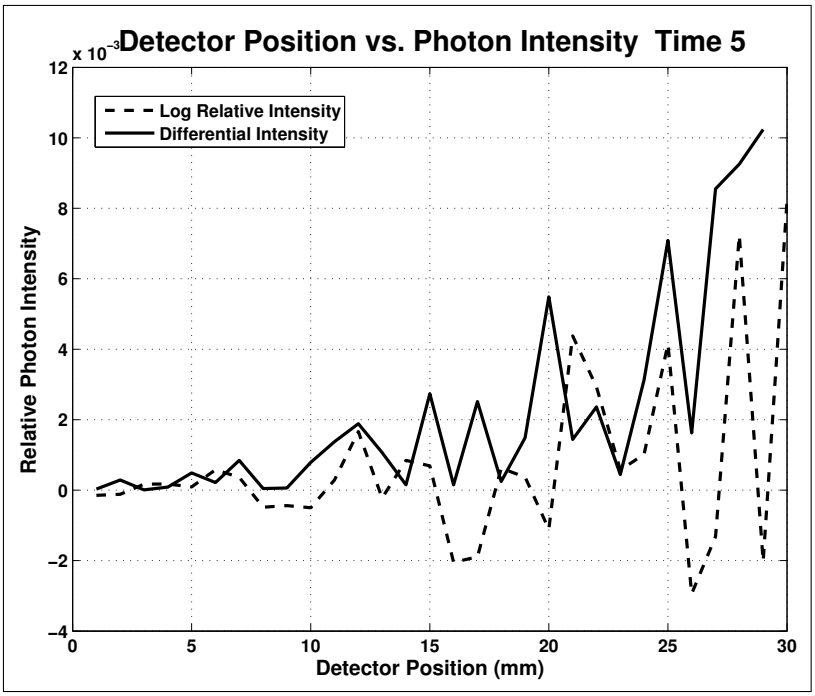

Figure A.70 Time5Skull30 Intensity Curves

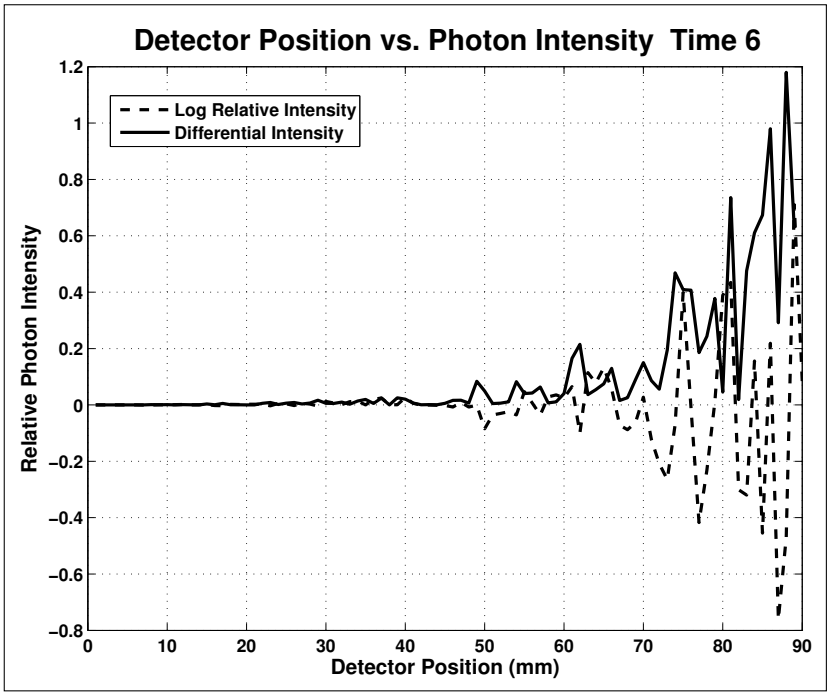

Figure A.71 Intensity Curves for Time 6, 1-100 mm, Thin Skull.

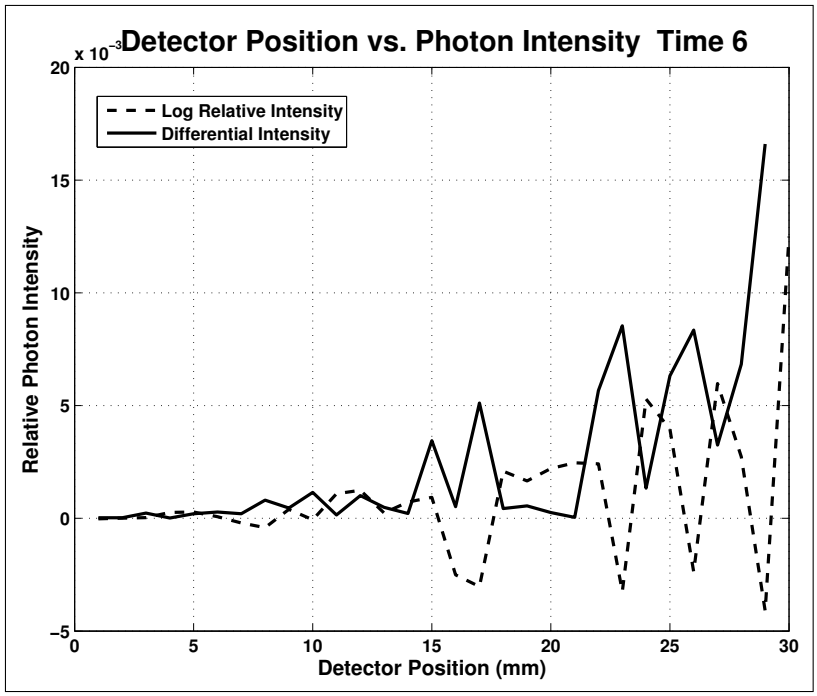

Figure A.72 Intensity Curves for Time 6, 1-30 mm, Thin Skull.

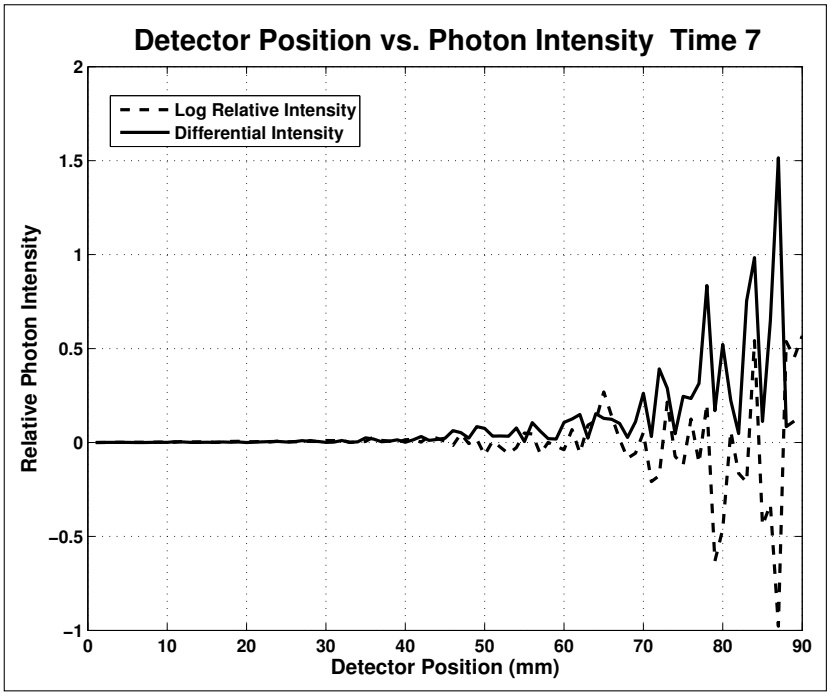

Figure A.73 Intensity Curves for Time 7, 1-100 mm, Thin Skull.

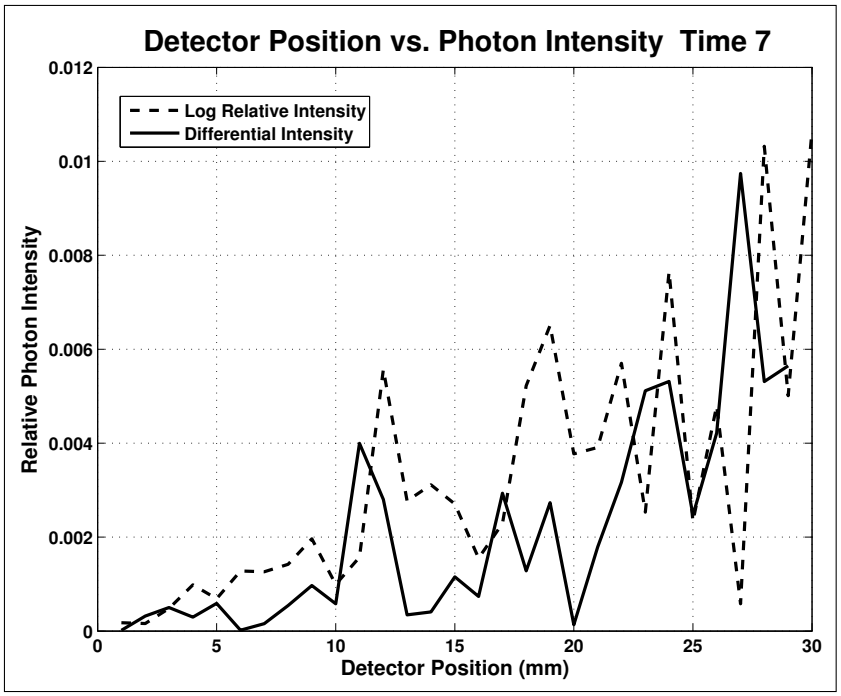

Figure A.74 Intensity Curves for Time 7, 1-30 mm, Thin Skull.

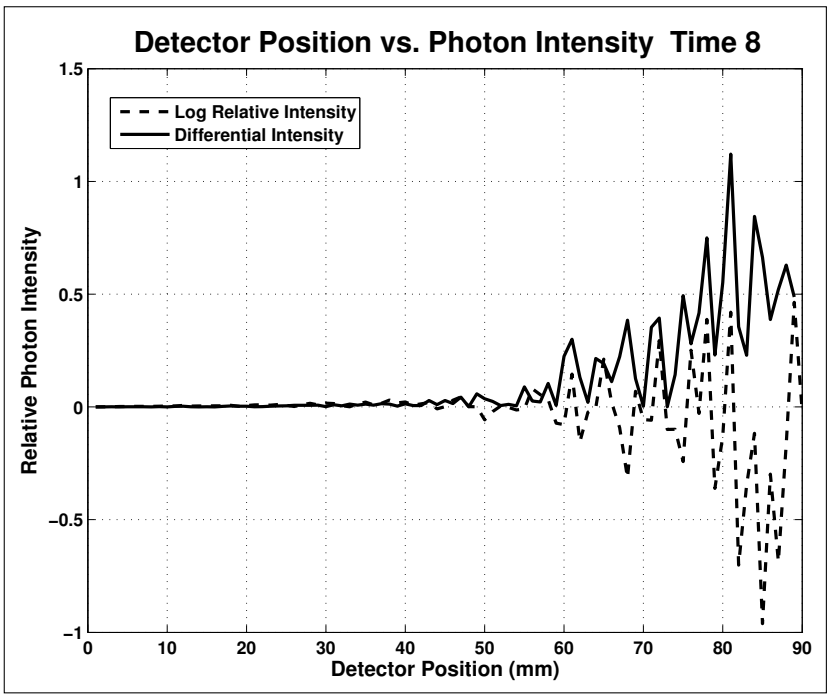

Figure A.75 Intensity Curves for Time 8, 1-100 mm, Thin Skull.

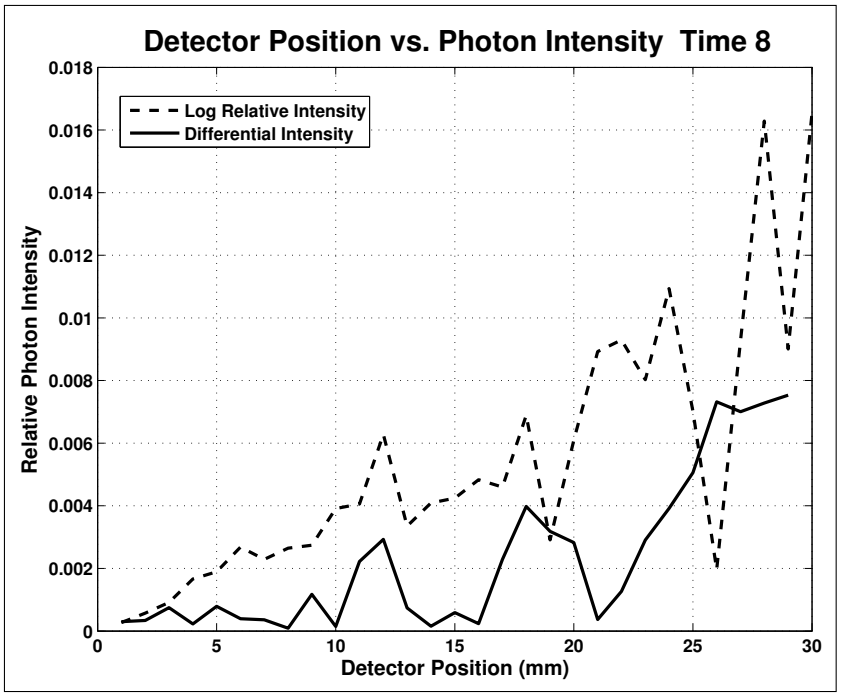

Figure A.76 Intensity Curves for Time 8, 1-30 mm, Thin Skull.

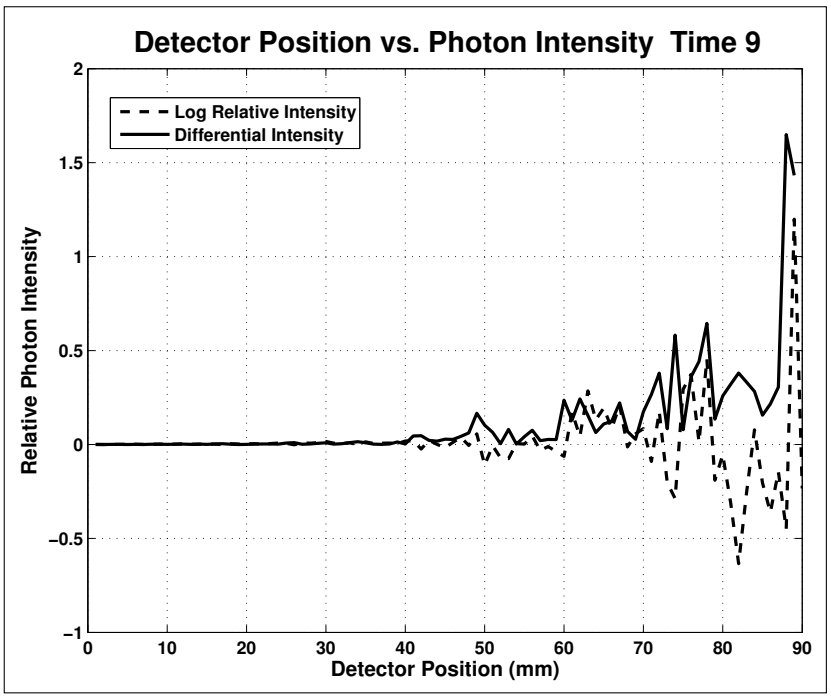

Figure A.77 Intensity Curves for Time 9, 1-100 mm, Thin Skull.

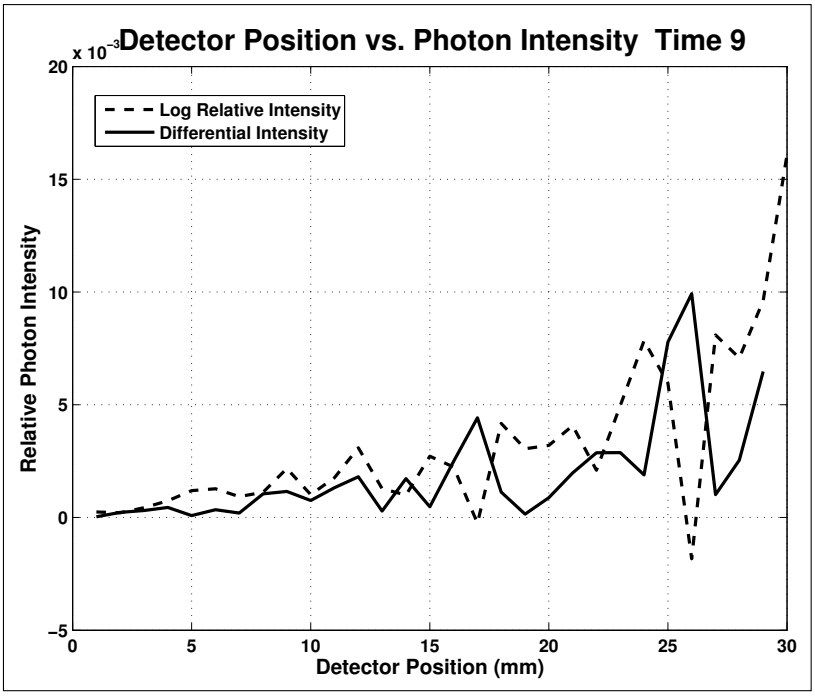

Figure A.78 Intensity Curves for Time 9, 1-30 mm, Thin Skull.

A.2 Slope Comparisons of Clusters Analysis Figures for Different Head Models

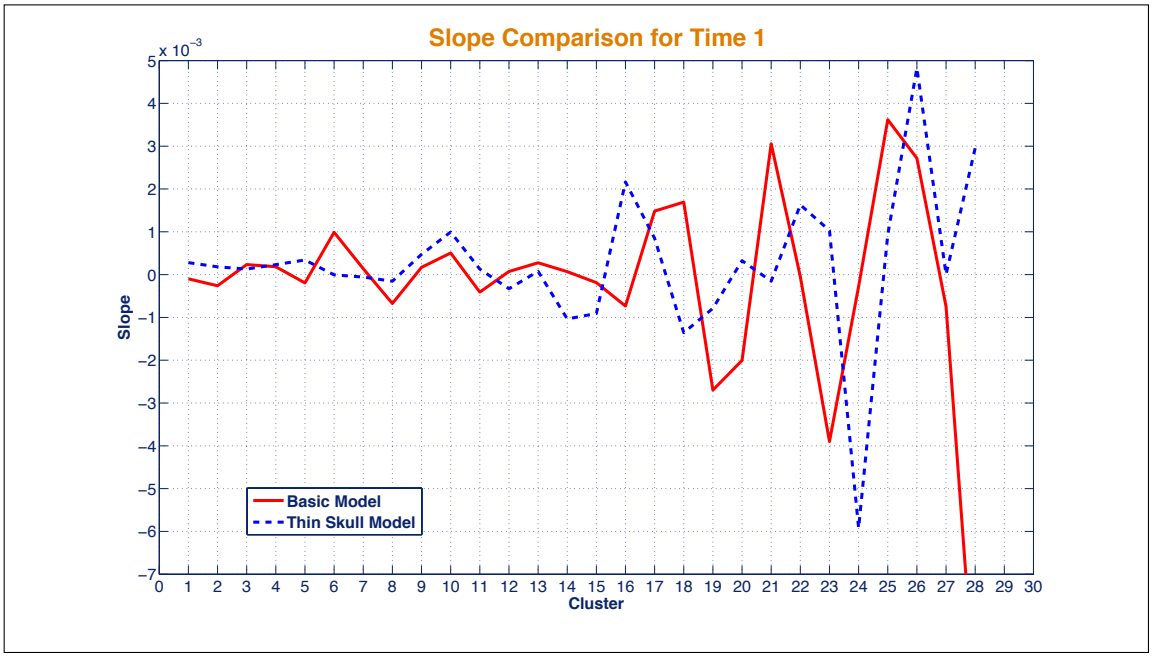

Figure A.79 Slope Comparisons for Time 1.

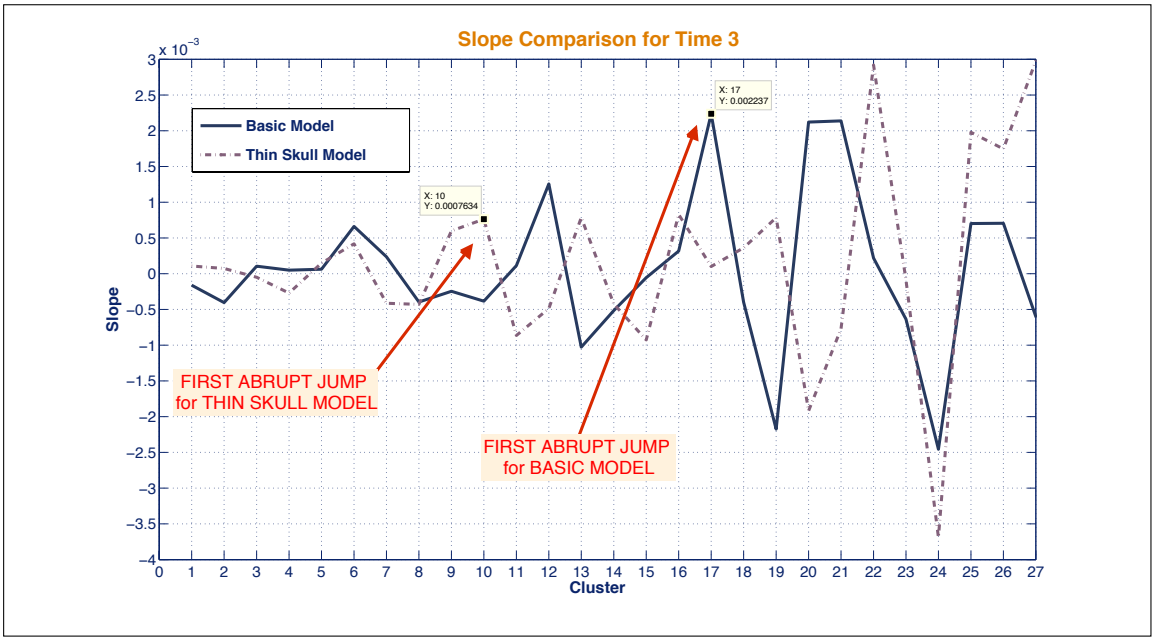

Figure A.80 Slope Comparisons for Time 3.

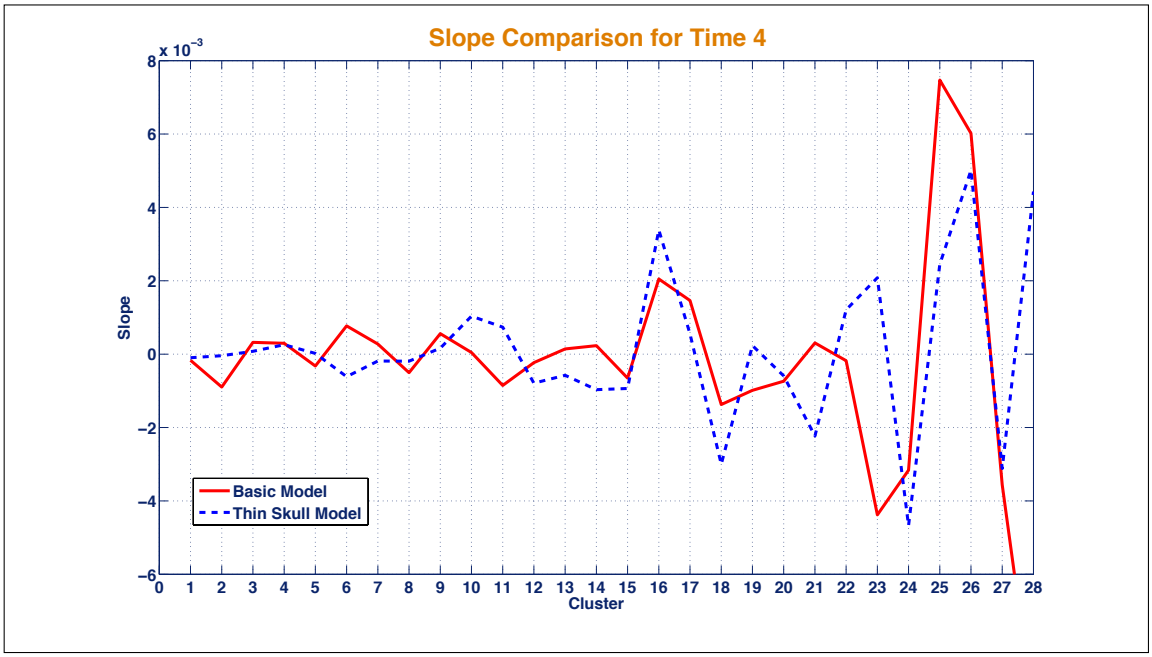

Figure A.81 Slope Comparisons for Time 4.

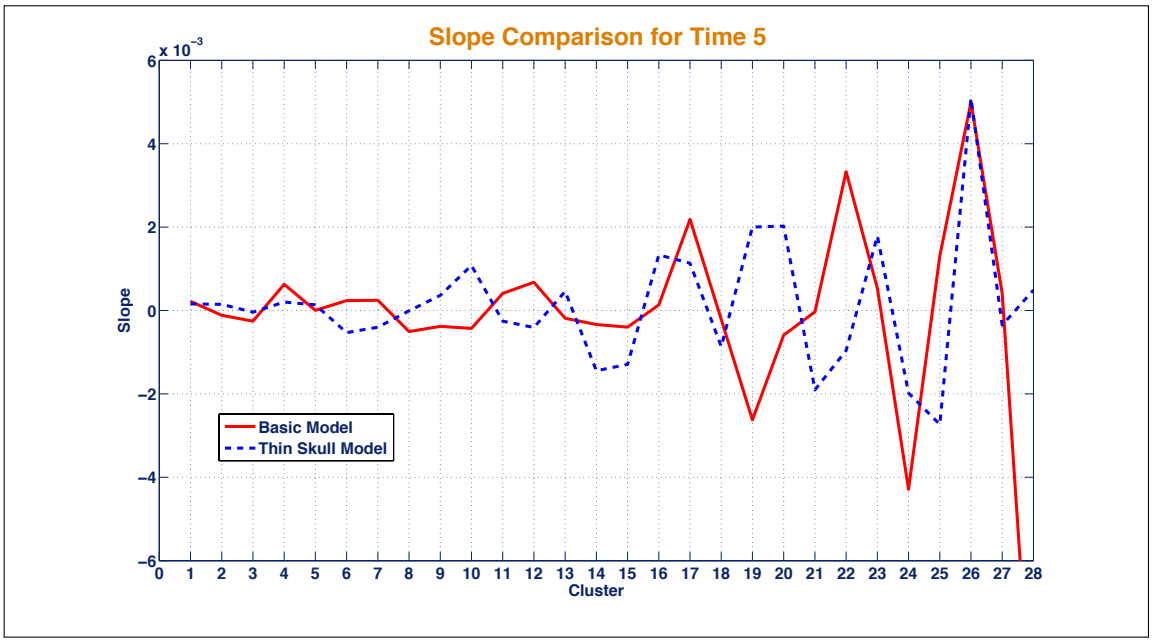

Figure A.82 Slope Comparisons for Time 5.

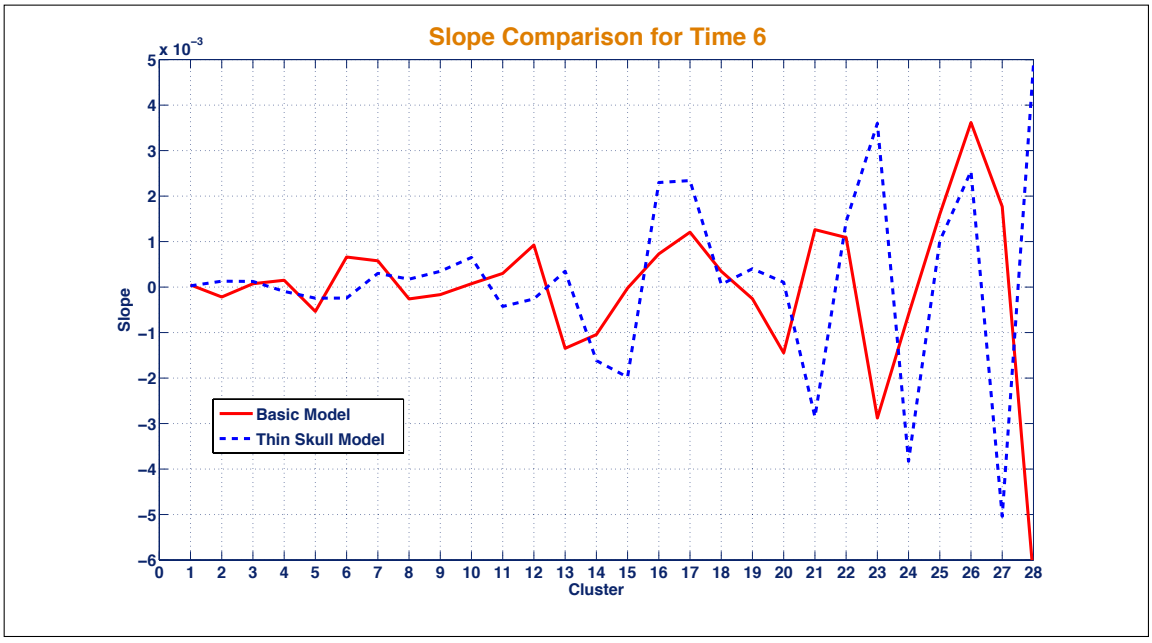

Figure A.83 Slope Comparisons for Time 6.

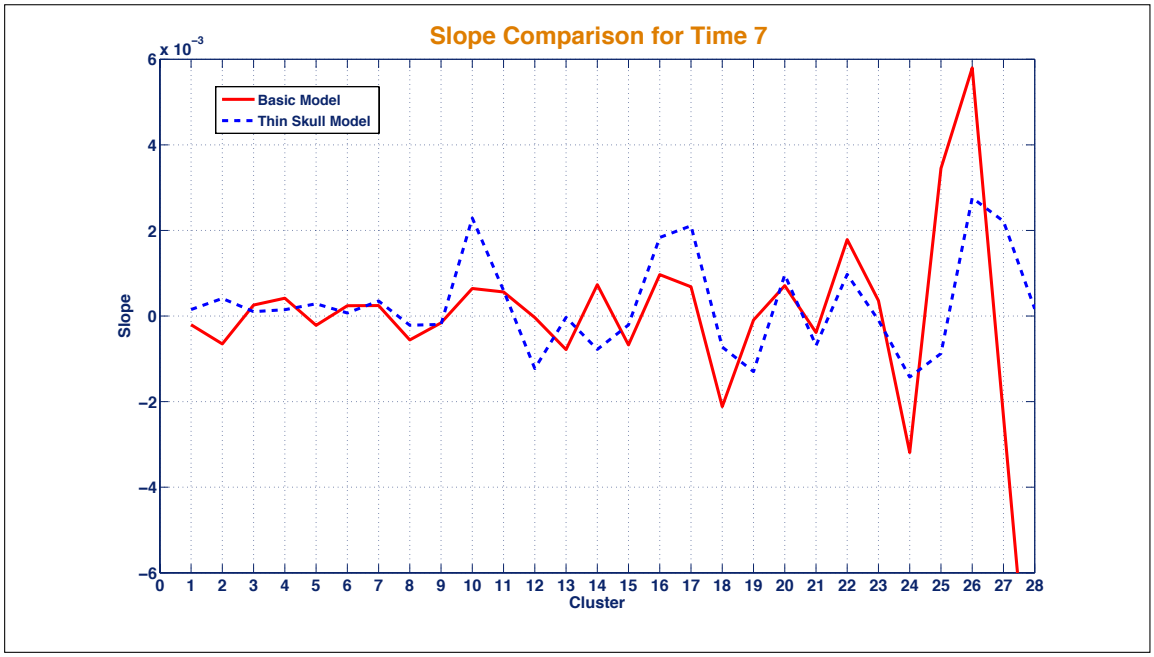

Figure A.84 Slope Comparisons for Time 7.

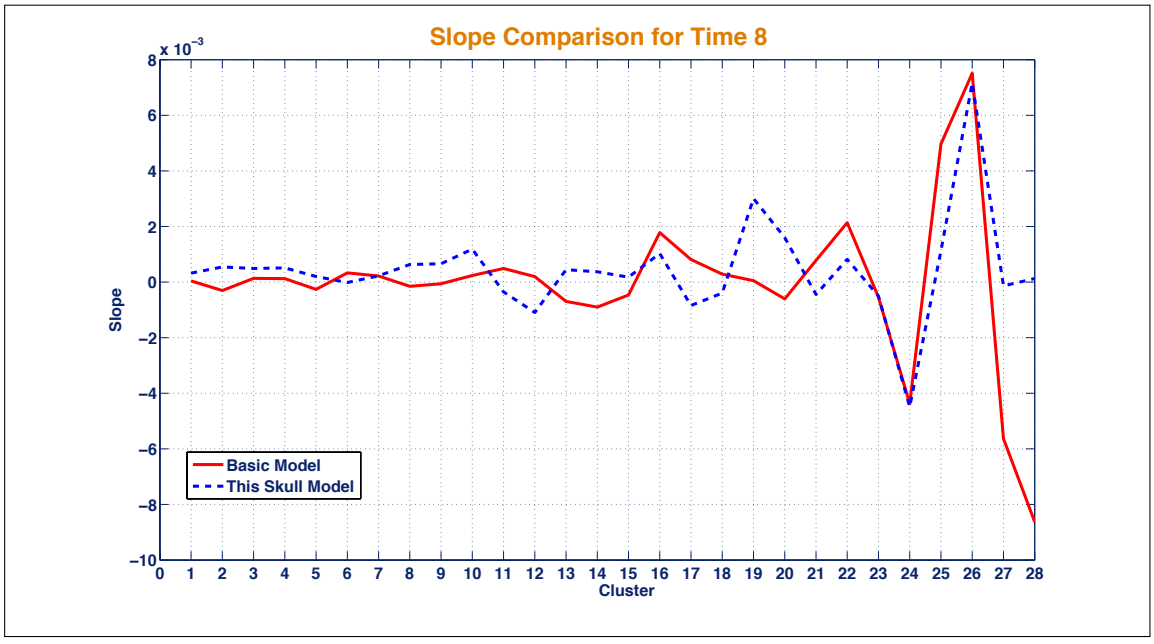

Figure A.85 Slope Comparisons for Time 8.

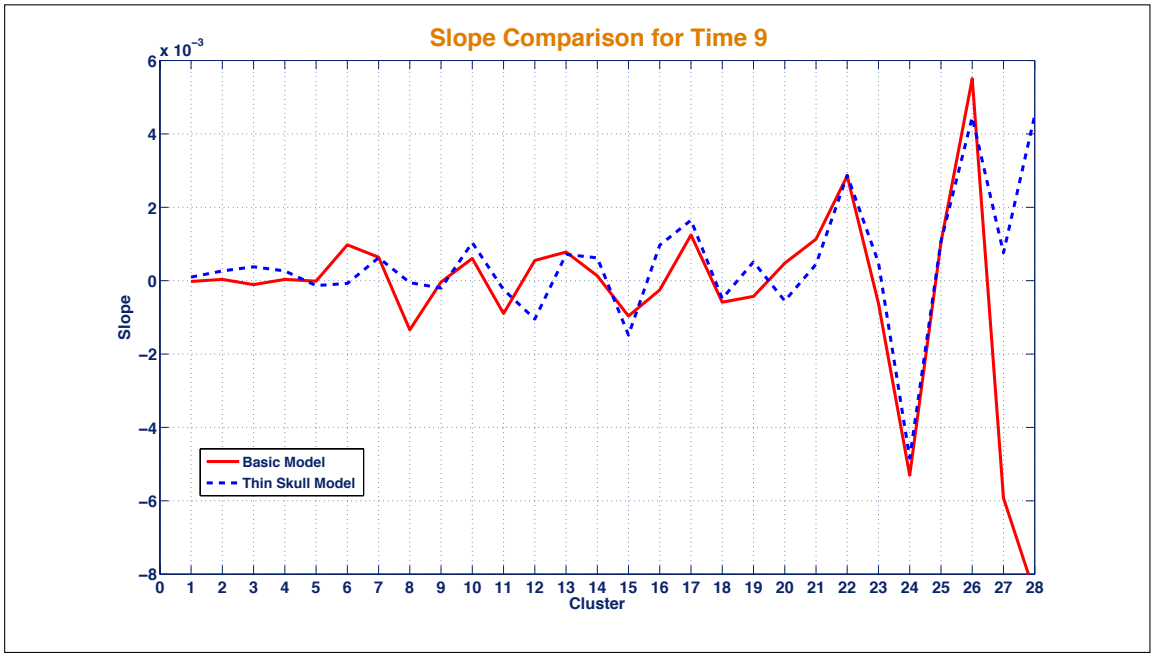

Figure A.86 Slope Comparisons for Time 9.

REFERENCES

1. Scholkmann, F., S. Kleiser, A. J. Metz, R. Zimmermann, J. Mata Pavia, U. Wolf, and M. Wolf, "A review on continuous wave functional near-infrared spectroscopy and imaging instrumentation and methodology.," *Neuroimage*, Vol. 85 Pt 1, pp. 6–27, Jan 2014.

2. Delpy, D. T., and M. Cope, "Quantification in tissue near-infrared spectroscopy," *Phil. Trans. R. Soc. Lond. B*, Vol. 352, pp. 649–659, 1997.

3. Strangman, G., D. A. Boas, and J. P. Sutton, "Non-invasive neuroimaging using near-infrared light.," *Biol Psychiatry*, Vol. 52, pp. 679–693, Oct 2002.

4. Tumer, A., S. B. Erdogan, and A. Akin, "Translating fmri to fnirs," in *The 6th International IEEE EMBS Neural Engineering Conference*, 2013.

5. Okada, E., and D. T. Delpy, "Near-infrared light propagation in an adult head model. ii. effect of superficial tissue thickness on the sensitivity of the near-infrared spectroscopy signal.," *Appl Opt*, Vol. 42, pp. 2915–2922, Jun 2003.

6. Gregg, N. M., B. R. White, B. W. Zeff, A. J. Berger, and J. P. Culver, "Brain specificity of diffuse optical imaging: improvements from superficial signal regression and tomography.," *Front Neuroenergetics*, Vol. 2, 2010.

7. Feng, S., F. A. Zeng, and B. Chance, "Photon migration in the presence of a single defect: a perturbation analysis.," *Appl Opt*, Vol. 34, pp. 3826–3837, Jul 1995.

8. Okui, N., and E. Okada, "Wavelength dependence of crosstalk in dual-wavelength measurement of oxy- and deoxy-hemoglobin.," *J Biomed Opt*, Vol. 10, no. 1, p. 11015, 2005.

9. Lloyd-Fox, S., A. Blasi, and C. E. Elwell, "Illuminating the developing brain: the past, present and future of functional near infrared spectroscopy.," *Neurosci Biobehav Rev*, Vol. 34, pp. 269–284, Mar 2010.

10. Haeussinger, F. B., S. Heinzel, T. Hahn, M. Schecklmann, A.-C. Ehlis, and A. J. Fallgatter, "Simulation of near-infrared light absorption considering individual head and prefrontal cortex anatomy: implications for optical neuroimaging.," *PLoS One*, Vol. 6, no. 10, p. e26377, 2011.

11. Villringer, A., and B. Chance, "Non-invasive optical spectroscopy and imaging of human brain function.," *Trends Neurosci*, Vol. 20, pp. 435–442, Oct 1997.

12. van der Zee, P., S. R. Arridge, M. Cope, and D. T. Delpy, "The effect of optode positioning on optical pathlength in near infrared spectroscopy of brain.," *Adv Exp Med Biol*, Vol. 277, pp. 79–84, 1990.

13. Steinbrink, J., A. Villringer, F. Kempf, D. Haux, S. Boden, and H. Obrig, "Illuminating the bold signal: combined fmri-fnirs studies.," *Magn Reson Imaging*, Vol. 24, pp. 495–505, May 2006.

14. Fox, P. T., and M. E. Raichle, "Focal physiological uncoupling of cerebral blood flow and oxidative metabolism during somatosensory stimulation in human subjects.," *Proc Natl Acad Sci U S A*, Vol. 83, pp. 1140–1144, Feb 1986.

15. Uludag, K., D. J. Dubowitz, E. J. Yoder, K. Restom, T. T. Liu, and R. B. Buxton, "Coupling of cerebral blood flow and oxygen consumption during physiological activation and deactivation measured with fmri.," *Neuroimage*, Vol. 23, pp. 148–155, Sep 2004.

16. Feng, S., F. Zeng, and B. Chance, "Monte carlo simulations of photon migration path distributions in mutiple scattering media," *Proc. SPIE*, Vol. 1888, pp. 78–89, 1993.

17. Ferrari, M., and V. Quaresima, "A brief review on the history of human functional near-infrared spectroscopy (fnirs) development and fields of application.," *Neuroimage*, Vol. 63, pp. 921–935, Nov 2012.

18. Cope, M., D. T. Delpy, E. O. Reynolds, S. Wray, J. Wyatt, and P. van der Zee, "Methods of quantitating cerebral near infrared spectroscopy data.," *Adv Exp Med Biol*, Vol. 222, pp. 183–189, 1988.

19. Yip, M. H., and M. J. Carvalho, "A monte-carlo maplet for the study of the optical properties of biological tissues," *Computer Physics Communications*, Vol. 177, pp. 965–975, 2007.

20. Wang, L., S. L. Jacques, and L. Zheng, "Mcml–monte carlo modeling of light transport in multi-layered tissues.," *Comput Methods Programs Biomed*, Vol. 47, pp. 131–146, Jul 1995.

21. Prahl, S. A., *Light Transport In Tissue*. PhD thesis, The University of Texas at Austen, 1988.

22. Wang, L., and S. L. Jacques, *Monte Carlo Modeling of Light Transport in Multi-layered Tissues in Standard C*. Laser Biology Research Laboratory University of Texas M. D. Anderson Cancer Center, 1992.

23. Binzoni, T., T. S. Leung, A. H. Gandjbakhche, D. Rfenacht, and D. T. Delpy, "The use of the henyey-greenstein phase function in monte carlo simulations in biomedical optics.," *Phys Med Biol*, Vol. 51, pp. N313–N322, Sep 2006.

24. Henyey, L. G., and J. L. Greenstein, "Diffuse radiation in the galaxy," *Astrophysical Journal*, Vol. 93, pp. 70–83, 1941.

25. Wang, L., and S. Jacques, "(mcml) monte carlo for multi-layered media." http://omlc.ogi.edu/software/mc/, 2007.

26. Okada, E., M. Firbank, M. Schweiger, S. R. Arridge, M. Cope, and D. T. Delpy, "Theoretical and experimental investigation of near-infrared light propagation in a model of the adult head.," *Appl Opt*, Vol. 36, pp. 21–31, Jan 1997.

27. Strangman, G., M. A. Franceschini, and D. A. Boas, "Factors affecting the accuracy of near-infrared spectroscopy concentration calculations for focal changes in oxygenation parameters.," *Neuroimage*, Vol. 18, pp. 865–879, Apr 2003.

28. Kawaguchi, H., T. Hayashi, T. Kato, and E. Okada, "Theoretical evaluation of accuracy in position and size of brain activity obtained by near-infrared topography.," *Phys Med Biol*, Vol. 49, pp. 2753–2765, Jun 2004.

29. Firbank, M., S. R. Arridge, M. Schweiger, and D. T. Delpy, "An investigation of light transport through scattering bodies with non-scattering regions.," *Phys Med Biol*, Vol. 41, pp. 767–783, Apr 1996.

30. Simpson, C., M. Kohl, M. Essenpreis, and M. Cope, "Near-infrared optical properties of ex vivo human skin and subcutaneous tissues measured using the monte carlo inversion technique," *Phys. Med. Biol.*, Vol. 43, pp. 2465–2478, 1998.

31. Firbank, M., M. Hiraoka, M. Essenpreis, and D. T. Delpy, "Measurement of the optical properties of the skull in the wavelength range 650-950 nm.," *Phys Med Biol*, Vol. 38, pp. 503–510, Apr 1993.

32. van der Zee, P., M. Essenpreis, and D. T. Delpy, "Optical properties of brain tissue," *Proc. SPIE*, Vol. 1888, pp. 454–465, 1993.